



Western Michigan University  
ScholarWorks at WMU

---

Master's Theses

Graduate College

---

4-2006

## Analytical Modeling and Simulation of an AUV with Five Control Surfaces

John Tomasi

Follow this and additional works at: [https://scholarworks.wmich.edu/masters\\_theses](https://scholarworks.wmich.edu/masters_theses)



Part of the Mechanical Engineering Commons

---

### Recommended Citation

Tomasi, John, "Analytical Modeling and Simulation of an AUV with Five Control Surfaces" (2006). *Master's Theses*. 4739.

[https://scholarworks.wmich.edu/masters\\_theses/4739](https://scholarworks.wmich.edu/masters_theses/4739)

This Masters Thesis-Open Access is brought to you for free and open access by the Graduate College at ScholarWorks at WMU. It has been accepted for inclusion in Master's Theses by an authorized administrator of ScholarWorks at WMU. For more information, please contact [wmu-scholarworks@wmich.edu](mailto:wmu-scholarworks@wmich.edu).



ANALYTICAL MODELING AND SIMULATION OF AN AUV  
WITH FIVE CONTROL SURFACES

by

John Tomasi

A Thesis  
Submitted to the  
Faculty of the The Graduate College  
in partial fulfillment of the  
requirements for the  
Degree of Master of Science in Engineering (Mechanical)  
Department of Mechanical and Aeronautical Engineering

Western Michigan University  
Kalamazoo, Michigan  
April 2006

Copyright by  
John Tomasi  
2006

## ACKNOWLEDGEMENTS

First and foremost I would like to thank my wonderful wife Kimberly, for without her constant love, patience, and support completion of this project would not have been accomplished. I would like to express my gratitude to Kim for always standing behind me during this past venture. I would also like to express my gratitude towards my parents for doing their best in providing me with all of the best experiences and foundation necessary to embark on this latest life venture.

I extend my thanks to my thesis advisor, Dr. Kapseong Ro, Professor of Mechanical and Aeronautical Engineering, for all of his time, help, and guidance. This project would not have even existed without his vision and encouragement.

I would also like to acknowledge and express my sincere appreciation to my thesis committee, Dr. J. Kamman and Dr. I. Sahin, for their assistance in completing this project; the employees of Western Michigan University's Inter Library Loan office, for their hard work and ability to locate the often obscure and difficult to locate materials I requested throughout the course of this project; Mr. Charlie Long, for donating his valuable time and skills to help in the creation of the beautiful scaled model used to experimentally verify my results; and Anne Saad and Jonathan Strombeck for electing to perform the experimental verification of my analytical results.

John Tomasi

# ANALYTICAL MODELING AND SIMULATION OF AN AUV WITH FIVE CONTROL SURFACES

John Tomasi, M.S.E.

Western Michigan University, 2006

This research describes the dynamic modeling and numerical simulation of an autonomous underwater vehicle (AUV) with five hydrodynamic control surfaces, necessary for the development of an autopilot algorithm, based solely upon analytical methodologies. The purpose of this research was to demonstrate the ability to develop a low order approximation of the dynamics and control characteristics of an underwater vehicle that is complete enough to validate a specific design before physical construction begins; therefore, allowing for a more cost effective virtual design, test, and evaluation process. The AUV model developed in this study takes into consideration inertia, hydrostatic forces, hydrodynamic forces, propulsion forces, control fin forces, added mass, and damping. The model assumes that the vehicle is sufficiently far enough away from the ocean bottom and surface so that their effects can be ignored. The necessary stability and control derivatives were determined through the use of engineering formulae. The mathematical model represents a general, nonlinear, six degrees of freedom model, and it is similar to those used to carry out atmospheric flight simulations. The non-linear model was linearized about the design (equilibrium) condition to obtain a linear state-space vehicle model.

## TABLE OF CONTENTS

ACKNOWLEDGEMENTS .....	ii
LIST OF TABLES .....	v
LIST OF FIGURES .....	vi
LIST OF EQUATIONS .....	viii
CHAPTER 1: INTRODUCTION .....	1
CHAPTER 2: VEHICLE DESIGN AND MODELING .....	5
2.1. Hull Design .....	6
2.2. Control Fin Design .....	16
2.3. Propulsion System Design .....	20
2.4. Vehicle Mathematical Model .....	29
CHAPTER 3: VEHICLE EQUATIONS OF MOTION AND SIMULATIONS .....	53
3.1. Equations of Motion .....	53
3.2. Simulation .....	66
3.3 Linearization .....	94
CHAPTER 4: CONCLUSIONS AND FUTURE WORK .....	99
4.1. Conclusions .....	99
4.2. Future Work .....	99
REFERENCES .....	101
GLOSSARY .....	107

## Table of Contents – Continued

APPENDICES .....	111
A. Table of Offsets for the <i>Deep 6</i> Hull .....	111
B. Tabular Comparison Between <i>Deep 6</i> and Other AUVs .....	112
C. Explanation of a Screw Propeller’s Inherent Inefficiency .....	113
D. Propeller Optimization Program Input and Output.....	115
E. Sample CFD Analysis Output.....	116
F. Additional CFD Verification .....	120
G. Verification of Analytical Solutions Through Physical Testing.....	123

## LIST OF TABLES

1.1. <i>Deep 6</i> Principle Particulars.....	4
2.3.1. Optimal Propeller Characteristics .....	28
2.4.1. <i>Deep 6</i> Mathematical Modeling Parameters.....	47



## LIST OF FIGURES

2.1.1. Example of Typical Torpedo Hull Form .....	8
2.1.2a. Pictorial Definition of Myring Hull Profile Terms .....	10
2.1.2b. General Effect of Nose Shape Coefficient, $n$ .....	10
2.1.2c. General Effect of Tail Shape Coefficient, $\theta$ .....	11
2.1.3. Pictorial Definition of Jackson Hull Profile Terms .....	11
2.1.4. AUV Length-to-Diameter Ratios.....	14
2.1.5. Profile Plot of the <i>Deep 6</i> 's Hull.....	15
2.2.1. Common Aft Fin Configurations .....	18
2.2.2. NACA 0025 Profile Curve.....	20
2.3.1. Operating Principle of the Contra-Rotating Propeller .....	23
2.3.2. Contra-Rotating Propeller Drive Mechanism .....	23
2.3.3. Optimal Propeller Characteristic Curves .....	28
2.3.4. Diagram of Optimal Propeller .....	29
2.4.1. Definition of Vehicle Fixed Reference Frame .....	31
2.4.2. Regression Fit of Fresh Water Kinematic Viscosity Data .....	33
2.4.3. 3D Renderings of the <i>Deep 6</i> .....	37
2.4.4. Regression Plot of Control Fin Lift vs. Angle of Attack .....	45
2.4.5. Regression Plot of Control Fin Drag vs. Angle of Attack Squared .....	46

## List of Figures – Continued

3.1.1. Aft Fin Configuration for Rudder Deflection .....	65
3.2.1. Simulation Program Flowchart.....	68
3.2.2. Simulation Results – Case 1, Steady State Condition.....	72
3.2.3. Simulation Results – Case 2, No Initial Velocity .....	75
3.2.4. Simulation Results – Case 3, Positive Bow Plane Deflection .....	78
3.2.5. Simulation Results – Case 4, Constant Positive Pitch Angle .....	81
3.2.6. Simulation Results – Case 5, Negative Rudder Deflection .....	84
3.2.7. Simulation Results – Case 6, Level Oblique Rise .....	87
3.3.1. Linearized $[A_2]$ Coefficient Matrix.....	96
3.3.2. Linearized $[B_2]$ Coefficient Matrix.....	97
3.3.3. Non-Linear vs. Linear EOM Comparison Plot.....	98

## LIST OF EQUATIONS

2.1.1a. Myring Hull Profile, Nose.....	8
2.1.1b. Myring Hull Profile, Tail .....	8
2.1.1c. Myring Hull Profile, Profile Description Code.....	9
2.1.2a. Jackson Profile, Entrance .....	9
2.1.2b. Jackson Profile, Run .....	9
2.1.3a. Series 58 Profile .....	9
2.1.3b. Series 58 Profile, Profile Description Code.....	9
2.2.1a. 4-Digit NACA Foil Profile Equation, General Form.....	20
2.2.1b. 4-Digit NACA Foil Profile Leading Edge Radius.....	20
2.3.1. Required Thrust .....	27
2.4.1. Mass Moment of Inertia About the Longitudinal Axis.....	35
2.4.2. Mass Moment of Inertia About the Transverse Axis.....	35
2.4.3. Mass Moment of Inertia About the Vertical Axis .....	35
2.4.4. Product of Inertia for X-Y Plane Symmetry .....	35
2.4.5. Product of Inertia for X-Z Plane Symmetry .....	36
2.4.6. Product of Inertia Y-Z Plane Symmetry .....	36
2.4.7. Empirical Hull Surface Area Formula .....	36
2.4.8. Drag Coefficient Definition .....	39
2.4.9. Longitudinal Drag Coefficient Equations.....	39
2.4.10. Definition of the Reynolds Number.....	40
3.1.1a. General Form of 6 Degree of Freedom Equations of Motion.....	56

## List of Equations - Continued

3.1.1b. Rearranged Form of 6 Degree of Freedom Equations of Motion.....	56
3.1.2. Surge Equation of Motion.....	56
3.1.3. Sway Equation of Motion.....	57
3.1.4. Heave Equation of Motion.....	57
3.1.5. Roll Equation of Motion .....	58
3.1.6. Pitch Equation of Motion.....	58
3.1.7. Yaw Equation of Motion .....	59
3.1.8. Body to Inertial Frame Velocity Transformation .....	63
3.1.9. Definition of $\dot{X}$ Vector.....	64
3.1.10. Definition of $X$ Vector .....	64
3.3.1. Taylor Series Expansion, General Form.....	95
3.3.2. Linearized Equations of Motions.....	95

# **CHAPTER ONE**

## **INTRODUCTION**

It has been stated numerous times that over three quarters of the Earth's surface is covered by water. The volume of water present on Earth has been estimated at 320 cubic miles [16]. Within this aquatic realm lie many vast, unexplored frontiers. For centuries, man has had an unexplainable draw to the sea. For terrestrial beings, though, glimpses into this alien world result only from the use of technology. One such technology that is showing great promise for aquatic exploration is the autonomous underwater vehicle, or AUV.

AUV technology has been evolving for the past 30 years. The majority of these vehicles were built for academic investigation, but a few vehicles have been able to successfully carry out important commercial missions. Some of the missions that AUVs are commonly assigned include undersea mapping, ocean sampling, surveillance, mine detection, and installation and inspection of cables and pipelines; however, the list of possible tasks is almost limitless. One of the driving forces behind AUV development is the vehicle's ability to operate independently of a support crew and surface ship for large portions of the mission. This feature renders the AUV economically superior to other underwater vehicles (such as towfish, remotely operated vehicles, and submersibles) for projects that encompass large areas and/or long time spans [30].

The adage “Do not put anything into the water that you cannot afford to lose” is especially true for AUVs. Since AUVs operate independently of surface support, there is no physical connection between them and their operators. AUV control is of great importance for vehicle retrieval and correlation of collected data to a specific location. Therefore, the ability to create a controller for a specific vehicle is of great interest to a segment of the marine industry.

The purpose of this study was to complete the preliminary work necessary for the development of an AUV autopilot control system. The scope of this project includes the preliminary design of a new AUV, the *Deep 6*, the construction of a mathematical model of this vehicle, and the simulation of this model. The design of a new AUV was required since a complete set of the necessary parameters for the construction of the mathematical model was not available for any one existing AUV. A design constraint for the *Deep 6* was that it be comparable to most other AUVs. This constraint allowed for a comparison between the generated results and those published for similar vehicles. The principle particulars for the *Deep 6* have been provided in Table 1.1.

The creation of the mathematical model of the *Deep 6* utilized analytical methods. This model represents a first order approximation of the real world environment. The methods used during the modeling included a combination of empirical formulae, design tables, and 3D CAD (computer aided design/drafting). The simulation of the *Deep 6* combined the mathematical model with a set of coupled, non-linear, 6 degree of freedom equations of motion to predict the vehicle’s response to various control parameter inputs (such as

control fin deflections). The simulation was performed using a program that was created specifically for this project. The simulation results were then used to create a linearized state-space vehicle model. The linearization of the non-linear vehicle model was necessary so that conventional control design methodologies would be applicable.

The design of an AUV is not revolutionary, neither is any one element of the procedure performed during this project. The novel work of this thesis project was the assimilation of various sources to create and document a complete approach for the design an AUV based upon analytical techniques. The documented approach provides a reliable, approximate solution for the final design prior to the construction and testing of a working model. The report that follows discusses, in detail, the design, modeling, and simulation of the *Deep 6*.

---

**Table 1.1: *Deep 6* Principle Particulars**

Description	Unit	Value
Length, LOA	in	60.0
Diameter, D	in	7.5
Slenderness Ratio, L/D	n.d.	8.0
Block Coefficient, $C_B$	n.d.	0.654
Prismatic Coefficient, $C_p$	n.d.	0.833
Displaced Volume, $\nabla$	in <sup>3</sup>	2,226.5
Fin Semi-Span, SS <sub>pn</sub>	in	5.625
Fin Chord, c	in	3.0
Fin Thickness to Chord Ratio, t/c	n.d.	0.25
Wetted Surface Area, S	in <sup>2</sup>	1,348.6
Displacement, $\Delta$	lbf	80.4
Max Operating Depth, $Z_{\max}$	in	18,000
Design Speed, $U_o$	kts	4.0
Propeller Diameter, $D_p$	in	3.0
Propeller Blade Number, z	#	4

Note: For definitions of any unfamiliar terminology, refer the Glossary.

---



## CHAPTER TWO

### VEHICLE DESIGN AND MODELING

The modeling portion of this project began with the preliminary design of a new AUV, the *Deep 6*. A new vehicle was conceptually created as a result of the great difficulty in obtaining sufficient published data on any one specific vehicle. If assumptions were used to fill in these information “gaps” any comparison between the calculated performance results and the published ones would have been tainted. Therefore, a new vehicle was required so that unrestricted access to all of the necessary inputs for the intended analysis would be available. A design constraint imposed for the new AUV was that it should be comparable to most other AUVs currently available so that results generated would contain the same general trends as those published for other similar vehicles. This use of experimental data provided a reality check later-on for the theoretical calculations performed during this study.

The design of marine vehicles is more often evolutionary than it is revolutionary. The designs of marine vehicles are generally only used to produce a small fleet, at best. Therefore, it is acceptable naval architecture practice to gather as much data for a new vehicle as possible from those previously built. The comparisons between vehicles may include any combination of trend data, non-dimensional regression curves, and visual inspections [33]. The preliminary design of the *Deep 6* follows standard naval architecture guidelines. The goal of this work was not to create an optimized hull form; therefore, it was assumed that the *Deep 6* was comparatively efficient since the design is

comparable to other successful AUVs. A qualitative comparison between the *Deep 6* and other AUVs has been provided in Appendix B.

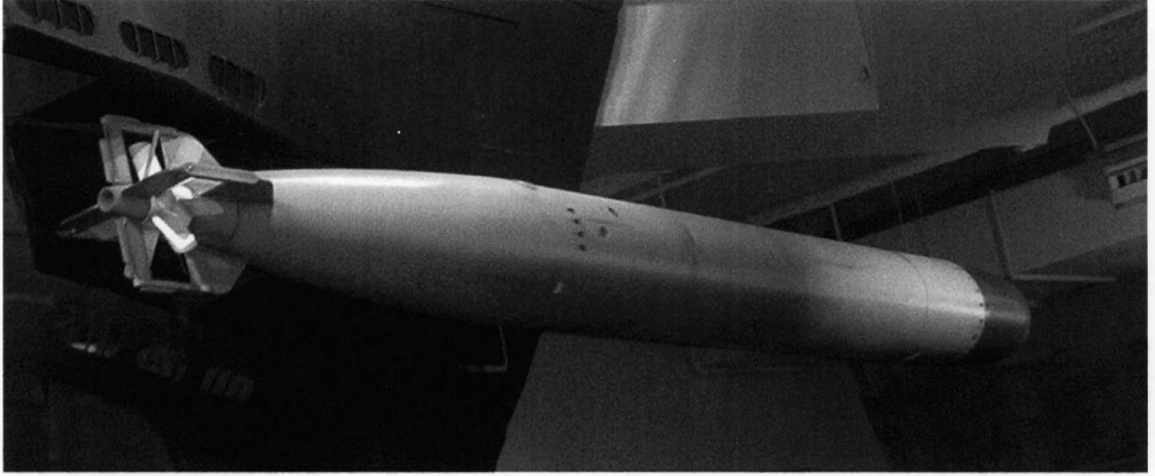
## **2.1 Hull Design**

The design of the *Deep 6* AUV began with the selection of a suitable hull form. As with all vehicles, it is desirable to create a hull that generates only a small amount of drag so that the vehicle can have sufficient power and endurance to be useful. For a submerged body, the two greatest contributors to the total drag are the skin friction drag and the form drag (a.k.a. pressure drag) [13]. It follows from general fluid mechanics that the skin friction drag is dependent upon the exposed surface area and the relative velocity between the surface and the fluid [20], [33]. The skin friction is typically estimated using formulas that were developed from studies of flat plates (such as the ITTC 1957 line equation). Once the exposed surface area, fluid, and relative velocity are known, it is fairly easy to determine this quantity. The skin friction can be minimized by reducing the amount of exposed surface area [20], [28], [33]. The form drag also depends upon the relative velocity between the fluid and the body. In addition to the relative velocity, form drag is also dependent upon the shape of the body. Determining an estimate for the form drag for a radically new shape is no simple task, requiring model testing and/or complex fluid calculations. Determining an estimate for the form drag for a shape that has been previously studied is also difficult, but can be accomplished through the use of similarity rules and regression analysis [33]. The form drag can be minimized by providing a longer, more slender shape with gradual transitions [28]. These two sources of drag, are generally divergent; the skin friction drag is of greater importance at lower speeds and the

form drag is of greater importance at higher speeds. Therefore, the process of optimizing a hull for total drag requires a balance between these two components [13], [20], [33]. Finding the minimum drag is a time consuming process – requiring consideration of both speed and shape. The Carmichael hull form, developed by Dr. Bruce Carmichael, is one example of a hull form that has been optimized for total drag reduction [28]. Hulls that have been optimized for drag reduction, such as the Carmichael hull, also have complex geometries, which result in an increased amount of wasted internal volume [28]. An alternative to the complex shape of a low drag hull form is the more classical torpedo shape shown in Figure 2.1.1. This form is characterized by a longer maximum diameter midsection. The drag of this form may be slightly higher than that of a comparable low drag hull, but it also provides a greater amount of usable volume for the payload [28], [29]. For this reason, the majority of underwater vehicle have hull forms that resemble the torpedo. Therefore, the hull form for the *Deep 6* was designed to also resemble the torpedo shape.

---

**Figure 2.1.1: Example of a Typical Torpedo Hull Form**



The above image depicts a typical World War II era torpedo. The cylindrical center section provides a greater amount of usable internal payload volume than a low drag hull form. The form does, however, produce more drag.

---

Three general hull forms commonly used as a basis for AUV hull profiles are the Myring profile, the profile presented by Capt. Harry A. Jackson, and the Series 58 hull form used by Gertler. The profiles are based upon various combinations of ellipses, parabolas, and polynomials of revolution [22], [29], [36]. The equations for each profile are provided below. It is worth noting that while the equations for the various profiles differ, each is capable of representing the same profile with only minor variances.

---

**Equation 2.1.1a: Myring Hull Profile, Nose (modified elliptical distribution)**

$$r = \frac{1}{2} d \left\{ 1 - \left( \frac{x-a}{a} \right)^2 \right\}^{\frac{1}{n}}$$

**Equation 2.1.1b: Myring Hull Profile, Tail (cubic distribution)**

$$r = \frac{1}{2} d - \left\{ \frac{3d}{2(100-a-b)^2} - \frac{\tan(\theta)}{(100-a-b)} \right\} \{x-a-b\}^2 + \left\{ \frac{d}{(100-a-b)^3} - \frac{\tan(\theta)}{(100-a-b)^2} \right\} \{x-a-b\}^3$$

### Equation 2.1.1c: Myring Hull Profile, Profile Description Code

$$a/b/n/\theta/\frac{1}{2}d$$

Where  $r$  is the hull radius at a specific longitudinal position,  $x$ ,  $d$  is the maximum hull diameter,  $a$  is the length of the nose section,  $b$  is the length of the center section,  $n$  is a nose shape coefficient, and  $2\theta$  is the included angle of the tail section (in radians). The terms of the equations are defined pictorially in Figures 2.1.3 a, b, and c.

Note: The Myring hull form is based upon a length of 100 units. The calculation of the hull radii for lengths other than 100 units can be performed by multiplying all longitudinal positions,  $x$ , by the coefficient (100/LOA), where LOA is the overall length of the hull. The maximum hull diameter is also based upon a hull of length 100. To obtain the maximum diameter,  $d$ , for the above equations for lengths other than 100 units the coefficient (LOA/100) needs to be used on the full scale vehicle diameter.

### Equation 2.1.2a: Jackson Profile, Entrance (parabolic distribution)

$$y_f = \frac{D}{2} \left[ 1 - \left( \frac{x_f}{L_f} \right)^{n_f} \right]^{1/n_f}$$

### Equation 2.1.2b: Jackson Profile, Run (elliptical distribution)

$$y_a = \frac{D}{2} \left[ 1 - \left( \frac{x_a}{L_a} \right)^{n_a} \right]$$

Where  $y_f$  and  $y_a$  are the hull radii at longitudinal positions  $x_f$  and  $x_a$ , respectively,  $L_f$  and  $L_a$  are the lengths of the hull entrance and run, respectively, and  $n_f$  and  $n_a$  are entrance and run shape coefficients, respectively. The terms in the above equations are defined pictorially in Figure 2.1.4.

### Equation 2.1.3a: Series 58 Profile (6<sup>th</sup> degree polynomial distribution)

$$y^2 = a_1x + a_2x^2 + a_3x^3 + a_4x^4 + a_5x^5 + a_6x^6$$

Where  $y$  is the non-dimensional ordinate at the non-dimensional abscissa  $x$ , the ordinate,  $y$ , is non-dimensionalized by the maximum hull diameter, the abscissa,  $x$ , is non-dimensionalized by the hull overall length,  $a_n$  are arbitrary constants selected to provide the desired form.

### Equation 2.1.3b: Series 58 Profile, Profile Description Code

$$mr_o r_1 C_p - \frac{L}{D}$$

Where  $m$  is the longitudinal position of the maximum (largest) section (in percentage),  $r_o$  is the non-dimensional nose radius,  $r_1$  is the non-dimensional tail radius,  $C_p$  is the hull prismatic coefficient (in percentage), and  $L/D$  is 10 times the hull length-to-diameter ratio – all numbers rounded to the nearest integer. The nose and tail radii are non-dimensionalized using the following formula:  $r = RL/D^2$ .

**Figure 2.1.2a: Pictorial Definition of Myring Hull Profile Terms**

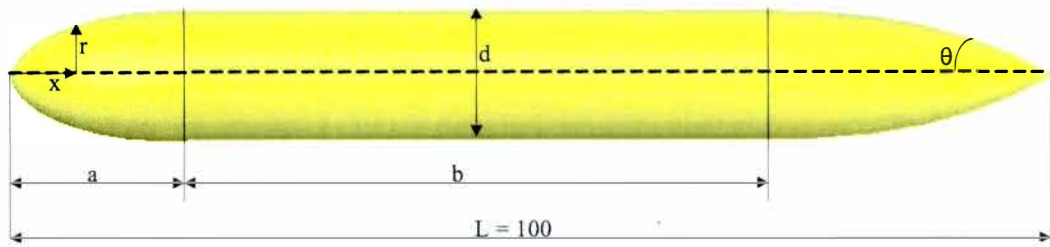


**Figure 2.1.2b: General Effect of Nose Shape Coefficient,  $n$**

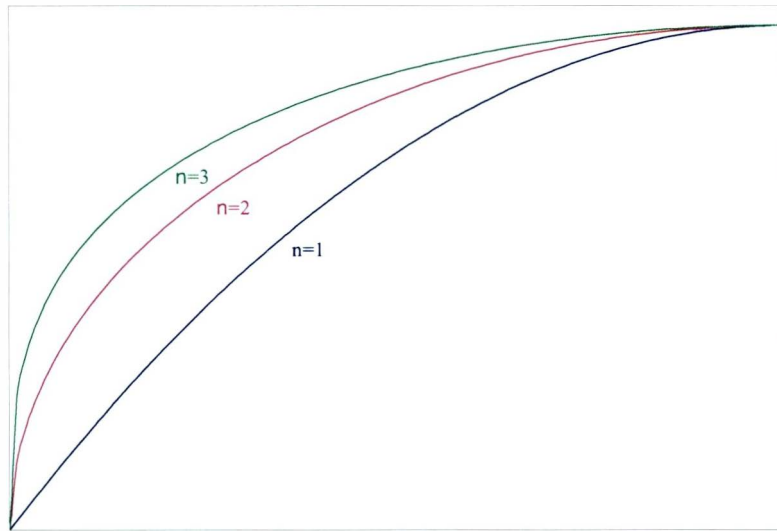


**Figure 2.1.2c: General Effect of Tail Shape Coefficient,  $\theta$**

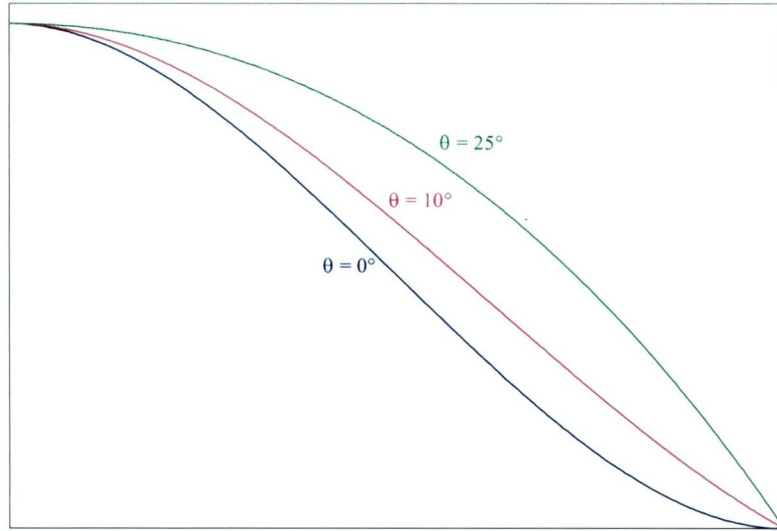
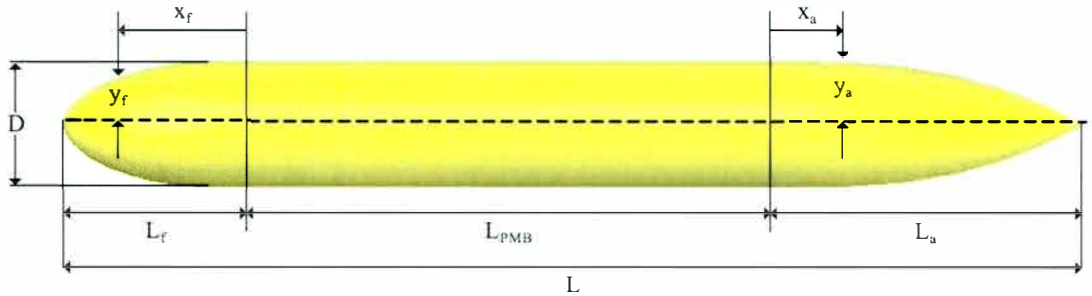


**Figure 2.1.3: Pictorial Definition of Jackson Hull Profile Terms**



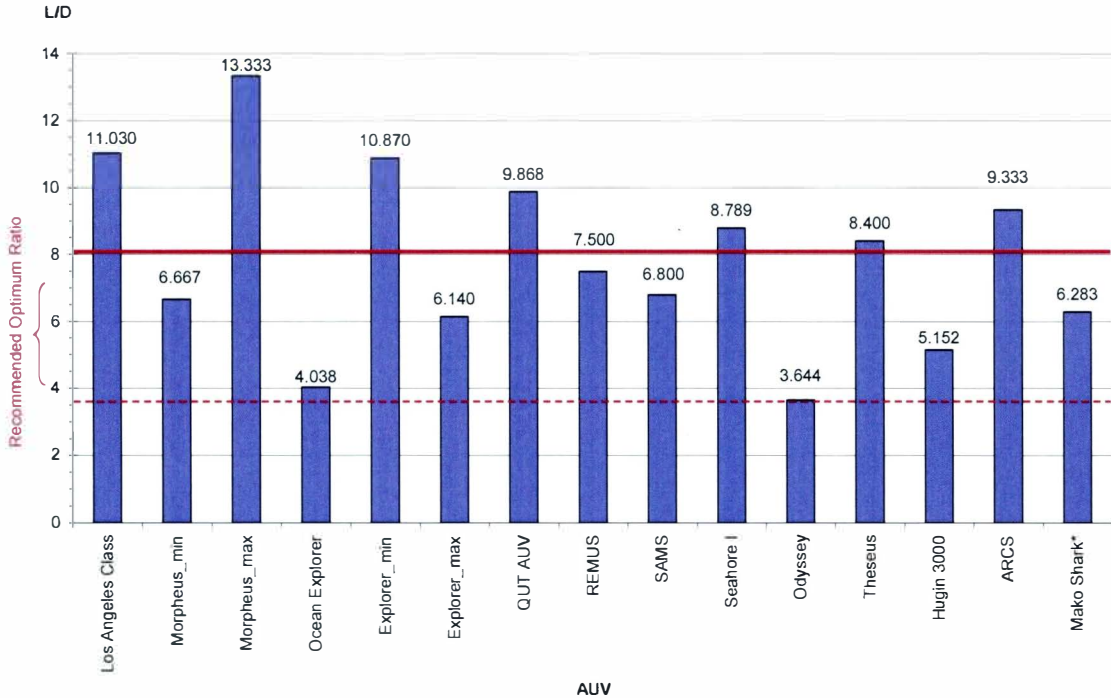
The *Deep 6*'s hull profile was developed using the Myring profile as the primary influence. The main reason for basing the hull on this form was the accessibility of the information published by Myring [36]. The initial values for the Myring profile code that were used when developing the *Deep 6* hull profile were those presented by Myring as hull "B", and by Prestero for the Wood's Hole Oceanographic Institute (WHOI) / Massachusetts Institute of Technology (MIT) joint AUV, REMUS [36], [39]. From this start, the values were modified based on published information for various vehicles and

the intentions of the current study. It was decided to utilize a parallel midsection to increase the volume of the vehicle. The final hull form has 33 in. of parallel middle body (PMB), which represents 55% of the total hull length. The comparatively large amount of PMB was used to increase the amount of the precious “maximum diameter area” available within the hull for payload. As mentioned previously, the reason that this area is of such great value is that its large, constant size eases the trouble of designing internal components and leads to less “dead” space. The entrance for the *Deep 6*’s hull was made blunt to reduce the amount of exposed surface area. Since most other underwater vehicles can be considered slow movers, reducing the skin friction was of greater importance than reducing the form drag. This conclusion follows from the previous discussion regarding hull drag. The bow of the *Deep 6* is comparable in bluntness to the bows of many other AUVs. The final bow section is 9 in. in length, or 15% of the total hull. The stern section of the *Deep 6* was allowed to taper smoothly over a long distance. This was done to produce a smooth transition from the maximum diameter down to the aft tip of the hull, thus preventing flow separation. Prevention of flow separation is important because separation increases the size of the vehicle’s wake and the amount of drag. The final stern section is 18 in. in length, or 30% of the total hull, and has an included angle of approximately  $30^\circ$ . The Myring hull profile code for the final *Deep 6* is 15/55/1.81/0.5236/6.25. The profile that was developed can also be accurately described by the Jackson profile using 1.9 and 2.75 for the shape coefficients,  $n_f$  and  $n_a$ , respectively, and 1.2 and 2.4 for the respective entrance and run length-to-diameter ratios. The Series 58 profile code for the final *Deep 6* hull profile is 33050163-36. A table of offsets for the developed hull is provided in Appendix A.



The investigation into the characteristics of an efficient hull revealed a strong connection between the length-to-diameter ratio (a.k.a. slenderness ratio) and the hull's drag. Small length-to-diameter ratios result in a hull that is very wide. Such a hull form would have plenty of internal volume, but would also generate large amounts of form drag (rendering the vehicle unsuitable for high speed travel). Large length-to-diameter ratios produce long, slender hulls (i.e. an arrow or a speed boat) that are ideal for high speed travel, but have a limited internal volume. Most studies agree that an optimal hull form for underwater vehicles will have a length-to-diameter ratio of 6, with some sources suggesting ratios as low as 4 and as high as 7 [3], [13], [20], [29]. Available sources also show that modern military submarines typically have length-to-diameter ratios in the range of 9 to 10 [13]. An investigation of what ratios are actually being used for AUVs was performed. A plot of the slenderness ratios is provided in Figure 2.1.4. The average of the length-to-diameter ratios calculated for the vehicles used in Figure 2.1.4 was 7.733. In order to simplify the calculations for the *Deep 6* and to increase the payload capacity, this average was rounded to 8. Although the selected value for the slenderness ratio is outside the suggested range, it was chosen because it was comparable to other AUVs. Again, it should be emphasized that the main focus of the current study was not to optimize the hull form.

**Figure 2.1.4: AUV Length-to-Diameter Ratios**



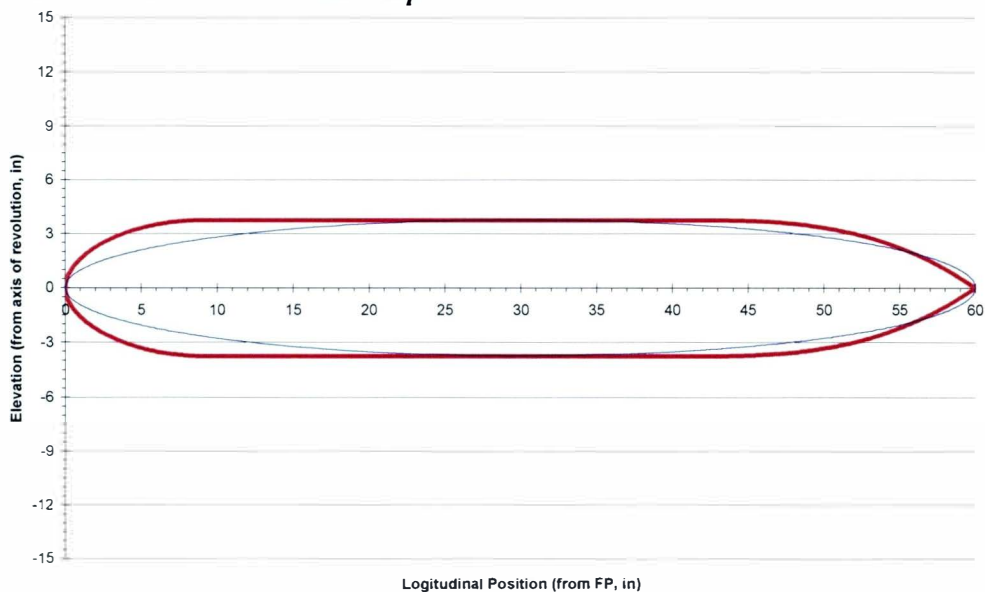
The above figure displays the available length-to-diameter ratios of the AUVs used for comparison during this project. The solid red line in the figure represents the length-to-diameter ratio that was used for the *Deep 6*. The red dashed line represents the *Deep 6*'s slenderness ratio if the PMB is neglected. Also provided for comparison in the above figure is the length-to-diameter ratio of a Los Angeles Class Submarine and of a mako shark (without its tail). The shark, arguably one of the most efficient shapes in the ocean, represents an optimized "hull" form with no parallel mid body. It is worth noting, out of academic interest, the close proximity of the shark's L/D ratio to the theoretically determined ideal of 6. The Los Angeles Class submarine and the Mako shark were not included in the calculation of the average L/D ratio.

The final element necessary to complete the preliminary design of the *Deep 6*'s hull was the overall length. The final length was chosen to be 60 in. (5 ft.). This dimension was selected due to the close proximity of Western Michigan University to Lake Michigan. To provide local significance to this project, *Deep 6* was designed for operation within the Great Lakes. The length of 5 ft. was chosen because this would create a vehicle of sufficient size to provide ample payload capacity while remaining manageable by two or three people on a small boat (20 to 50 ft. in length). The boat size and crew number were

factored into the vehicle length decision because they are an essential components to the vehicle's launch and retrieval process. With the hull length determined, it was then possible to generate a plot of the *Deep 6*'s profile. Figure 2.1.5 shows (in red) the profile plot that was created. The blue curve in Figure 2.1.5 is an ellipse of equal length and diameter to the *Deep 6*. This has been included in the plot of the *Deep 6* hull profile to provide a visual comparison between the two. A comparison between the *Deep 6* profile and the ellipse is of importance because many of the formulas used to estimate the *Deep 6*'s hydrodynamic characteristics (such as added mass and hydrodynamic damping) are based upon an ellipsoid of revolution [19], [38]. Therefore, it is important for the two curves to resemble each other, as it directly affects the quality of the estimates.

---

**Figure 2.1.5: Profile Plot of the *Deep 6*'s Hull**



The red curve represents the *Deep 6* hull profile. The blue curve represents the profile of an ellipsoid of revolution of equal length and diameter.

---

## 2.2 Control Fin Design

There are two distinct categories for controlling an underwater vehicle. The first category utilizes multiple thrusters, which are typically fixed and arranged at various angles to one another. Directional control is achieved through the management of which thrusters are activated. An alternate application of this method allows the thrusters to rotate about a fixed axis, thus reducing the total number of thrusters required. This control method does permit excellent “close quarters” maneuvering but at the expense of generating considerable drag (from the external thruster housings and/or from the defects in the streamlined hull shape caused by the thruster duct openings) [5], [33]. As a result, this configuration is typically limited to and best suited for tethered vehicles and other slow moving vehicles (note: the word “slow” is used in a relative sense – most objects move slowly underwater compared to terrestrial standards) [28]. The second method utilizes fins to generate the forces necessary for directional control. This method does require flow over the control fins to generate a force. As a result, this method is ineffective for hovering and low speed maneuvers [1], [5], [20], [28]. The large distance required for maneuvering (on the order of several body lengths for turns) is another drawback of this method [5]. The benefits of the control fin method are that the fins produce only a marginal increase in the drag when the fins are aligned with the hull and the fins tend to act as rotational stabilizers [1], [41]. For vehicles that typically cover great distances moving along a straight path at a constant speed, this method of control is ideal. For this reason, fins are the most common method of control for AUVs. This precedent was followed when designing the control system for the *Deep 6*. The similarity that exists between an AUV using control fins and an airplane also influenced

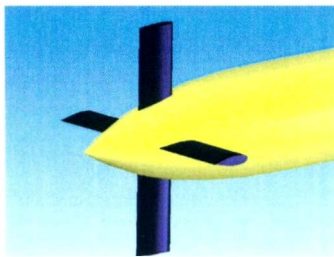
this decision. This resemblance served as justification for the use of airplane formulae and methodologies during subsequent portions of this investigation. The decision of which method of control would be used was significant as it influenced the structure of the vehicle equations of motion.

After it was decided that fins would be used to control the *Deep 6*, it was necessary to determine the arrangement of the fins. There exists an infinite number of possible arrangements, but some common documented aft fin arrangements include the conventional vertical rudder and horizontal stern plane (“T”) arrangement, the “X” arrangement, the inverted “Y” arrangement, and the underbody arrangement common to World War II era submarines (and similar to surface ships). Figures 2.2.1 displays the aforementioned aft fin configurations. In addition to the aft fins, a vehicle may or may not have fins located towards the bow. By far the most common arrangement used for AUV control is the “T” arrangement without bow fins. Despite the popularity of the “T” arrangement, an inverted “Y” arrangement, with the fins equally spaced around the hull, and with two horizontal bow fins was selected for the *Deep 6*. This decision was influenced by the maneuverability capabilities claimed by International Submarine Engineering, Ltd. of their Explorer AUV which also uses this arrangement. To summarize, this configuration allows the vehicle to move obliquely in the vertical (X-Z) plane while maintaining a horizontal attitude, in addition to the typical yaw and pitch maneuverability. The benefit of this additional capability is that transmissions emitting from the vehicle (such as SONAR pulses) will remain normal to a flat bottom while the vehicle changes altitude (such as to avoid a potential obstacle) [28]. For these reasons an

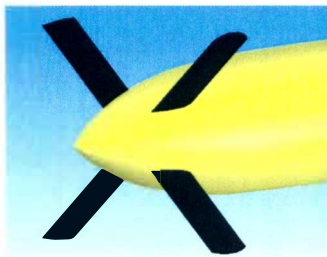
inverted “Y” arrangement with bow fins was adopted for the *Deep 6*. This decision proved to be beneficial because some of the modeling software used later in the design process required that canard wing arrangements (two sets of wings/fins longitudinally spaced along the same vertical plane) be avoided [2].

---

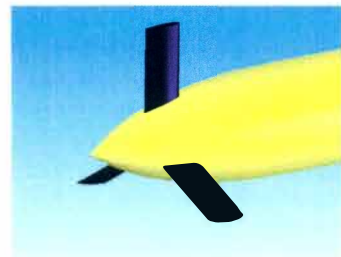
**Figures 2.2.1: Common Aft Fin Configurations**



(a) “T” Arrangement



(b) “X” Arrangement



(c) Inverted “Y” Arrangement



(d) WWII Era Arrangement

---

The final decisions to be made to complete the control fin design were the shape and dimensions. For simplicity, all of the fins have the same general shape. The controllability section of the *Principles of Naval Architecture*, vol. III, recommend the

use of NACA foils 0018 – 0025 for use as control fins on marine vehicles. The stated advantages of these sections are the increased stall angles and lift coefficients, the relatively stationary center of pressure, and ability to install adequately sized drive shafts [34]. The availability of published research on the recommended foil sections led the selection of the NACA 0025 section for the *Deep 6*'s control fins. Figure 2.2.2 shows the profile of the selected foil shape. Equations 2.2.1 provide the general equations used to describe a 4-digit NACA foil section [1], [34]. The decision for the foil chord length and the fin span was made to minimize the amount of fin surface area present (thus reducing the additional drag imposed by the fins) while still providing sufficient force generating capability to allow the vehicle to maneuver within a reasonable area. An estimate for a suitable chord length of 3.00 in. and for a “wing” span of 11.25 in. was made. To allow these low aspect ratio fins to be effective controllers they required large moment arms. Therefore, the fins needed to be placed as far away from the vehicle center of mass as possible. The aft fins were placed so that their quarter chord point is 52.75 in. from the bow (24.40 in. aft of the mass center). This location was selected as the furthest distance aft possible that still allowed sufficient space for the propulsor. The bow fins were placed so that their quarter chord point was 14.00 in. aft of the bow (14.35 in. forward of the mass center). This location was chosen so that the bow fins were far enough behind the hull entrance as to not disturb the flow over the bow, yet far enough forward to produce sufficient pitching moment. The quality of these estimates was evaluated during the simulation portion of this project.

---

**Figure 2.2.2: NACA 0025 Profile Curve**

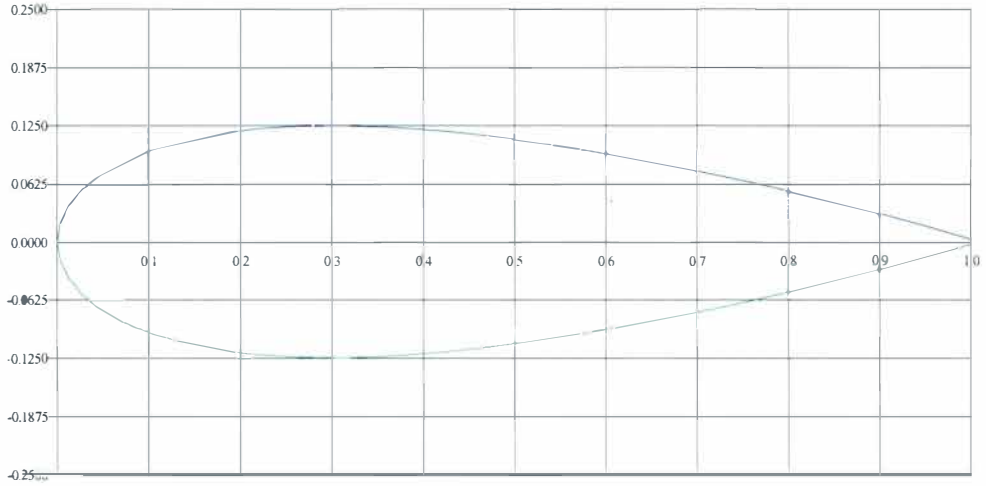


Image generated by Digital Wind Tunnel 2-D section analysis

**Equation 2.2.1a: 4-Digit NACA Foil Profile Equation, General Form**

$$\pm y = \frac{t}{0.20} \left( 0.29690\sqrt{x} - 0.12600x - 0.35160x^2 + 0.28430x^3 - 0.10150x^4 \right)$$

Where  $y$  is the vertical distance away from the chord line at a specific longitudinal position,  $x$ , and  $t$  is the maximum section thickness (expressed as a fraction of the chord length).

Note: The above equation describes a foil with a chord length of 1 unit. To the coefficients in the equation must be scaled to produce results for differing chord lengths.

**Equation 2.2.1b: 4-Digit NACA Foil Profile Leading Edge Radius**

$$r = 1.1019t^2$$

Where  $r$  is the leading edge radius of the foil profile and  $t$  is the maximum section thickness (expressed as a fraction of the chord length).

---

## 2.3 Propulsion System Design

To satisfy the requirements of the planned vehicle simulation, the only necessary propulsion system parameters are the vehicle design speed and propulsor rate of revolution. These values, as with most of the other design values discussed thus far, were selected so that they would be comparable to other AUVs. For completeness of the



preliminary design of the *Deep 6*, the groundwork for a propulsion system design was laid. The discussion that follows describes the preliminary design of the *Deep 6*'s propulsion system.

By far the most common method of propulsion for marine vehicles is the screw propeller. While the screw propeller possesses the fundamental flaw that its use increases the vehicle's drag (thus requiring an even larger force necessary for motion)<sup>1</sup>, its simplicity over other forms of propulsion has allowed it to maintain its dominance [3], [32], [33]. For almost all marine vehicles the propeller is symmetrically located at the stern. The long and slender submarine forms are also prone to another of the screw propeller's characteristic problems, the unbalanced torque. This problem is also experienced by single propeller airplanes and helicopters without a tail rotor. For this problem, however, there exist a number of solutions. The best known method of balancing the propeller torque is through the use of two propellers rotating in opposite directions. This solution can be implemented by either transversely offsetting the propellers to form a counter-rotating pair (such as those found on twin screw surface ships and some Russian Naval Submarines) or to longitudinally offset the pair to form a (coaxial) contra-rotating pair. The counter-rotating propeller solution, simply put, is an application of two individual conventional propellers and works by using the second propeller to produce an equal but opposite torque. Similar to the single propeller, the flow behind each propeller in the counter-rotating solution contains a wasted rotational component. The contra-rotating

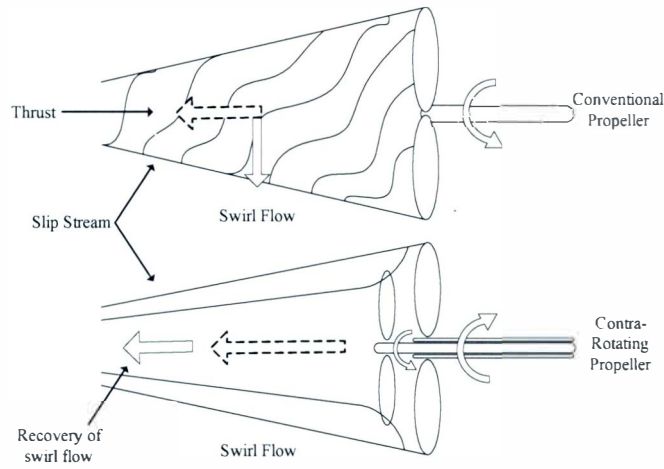
---

<sup>1</sup> A more in-depth explanation of the fundamental inefficiency of the screw propeller has been provided in Appendix C

propeller solution works by using the second propeller to produce an equal but opposite torque (as with the counter-rotating propellers), but also to remove the rotational momentum of the fluid imparted by the first propeller. This second effect produces a more efficient propeller thrust that is almost completely aligned with the body longitudinal axis/direction of travel [3], [13], [33], [48]. A diagram explaining the concept of the contra-rotating propeller is provided in Figure 2.3.1. Contra-rotating propellers provided additional gains in efficiency by allowing smaller blade areas and lessened blade loading compared with an equivalent single screw [3]. Either of the fore mentioned solutions presents a challenging set of design requirements. The narrow hulls of most underwater vehicles make the counter-rotating method difficult to install, especially in smaller vehicles. The contra-rotating propeller solution requires a complicated drive system, shown in Figure 2.3.2 [3], [13]. Experiments on surface ships with contra-rotating propellers show an energy savings with this propulsion scheme ranging from a few percent to as much as 16% [10], [14], [27], [48]. Unfortunately, designers typically feel that the additional complexity and weight required for contra-rotating propeller installation negate the small efficiency gains [10].

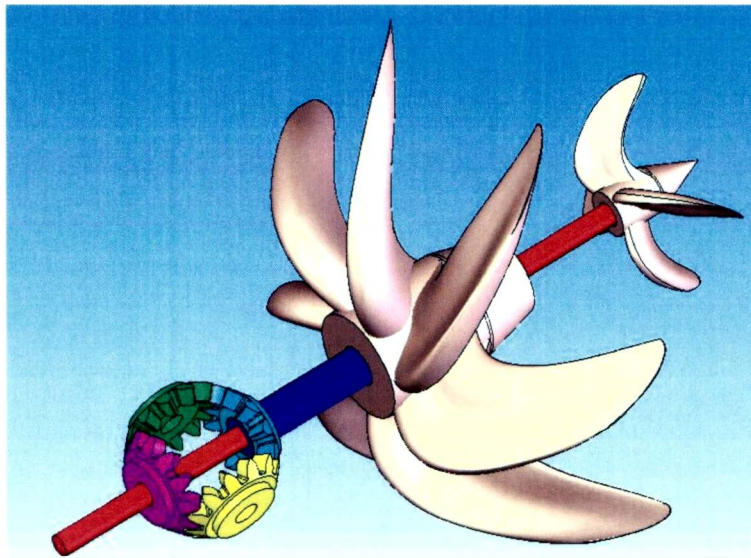
---

**Figure 2.3.1: Operating Principle of the Contra-Rotating Propeller**



The above diagram displays the operating principle of the contra-rotating propeller. The top diagram shows the two thrust components generated by a conventional single screw propeller, the axial and the rotational. The bottom diagram shows that the second propeller in a contra-rotating propeller pair removes the rotational component imparted by the first propeller, thus creating, in theory, an all axial thrust component. The contra-rotating pair therefore has a higher efficiency because it generates less wasted energy.

**Figure 2.3.2: Contra-Rotating Propeller Drive Mechanism**



The above figure is a SolidWorks rendering of a simplified contra-rotating propeller drive system. The red “inner” shaft rotates the same direction as the magenta gear and the 4-bladed propeller. The yellow and green gears drive the blue gear (thus the blue “outer” shaft and the 7-bladed propeller) in the opposite direction of the magenta gear. Power to the system is usually input through the inner shaft, forward of the magenta gear, or through the yellow and green gears.

---

Another approach for countering the propeller torque is through the use of a Grim wheel. The Grim wheel is similar in appearance to the contra-rotating propeller design, but engine power is not provided to the after set of blades. The “free spinning” stator blades serve to remove the rotation of the flow emerging from the propeller. The Grim wheel may also be designed to produce additional thrust. Installation of the Grim wheel is difficult in practice [13]. A simpler approach than the Grim wheel is to use stationary stators mounted before the propeller. When operating at the design speed, these stationary stator blades produce a counter “pre-swirl” that cancels out the propeller torque [13]. The final solution for overcoming the unbalanced propeller torque problem is to design the vehicle such that the center of gravity (CG) is vertically much lower than the center of buoyancy (CB) (usually requiring heavy ballasting). The vertical offset of the CG and the CB will produce a righting moment when the vehicle rolls due to the unbalanced torque. When the righting moment becomes large enough, the propeller torque will become balanced and the vehicle will cease to roll. While the vehicle CG can theoretically be positioned such that a static righting moment is created that perfectly offsets the propeller torque (through the use of a transverse offset), typically some amount of roll during operation must be accepted with this option.

A contra-rotating propeller arrangement was selected to counteract the unbalanced torque effects of a single propeller. This decision was made despite the fact that all of the vehicles taken into consideration for comparison utilized a single propeller configuration with no Grim wheel or stationary stator blades. The contra-rotating propeller arrangement was chosen because of its ability to produce no net propulsion torque. This

had the added benefit of simplifying the equations of motion. Although the contra-rotating propeller drive system is complex, it has been successfully used on torpedoes to increase their directional stability since the invention of the Whitehead torpedo in 1864 [10]. Since there is no clear agreement on the potential efficiency gains offered by the use of contra-rotating propellers, this effect has been ignored [10], [27], [48]. This procedure provided an additional margin of safety for the design calculations.

For the purposes of preliminary design, the two propellers of the *Deep 6* are of equal size and blade number, each producing one half of the required thrust. Although having two propellers of equal size and blade number may appear to vary from accepted naval architecture theory for contra-rotating propeller installation, a visual inspection of several photos of the propellers for torpedoes revealed a similar approach [46]. By using a matched pair of propellers (identical except in rotational orientation) the design process was simplified since only the design of a single propeller was required.

Selection of an optimal propeller was performed with the assistance of the Propeller Optimization Program (POP) internet Java applet developed by Dr. Michael Parsons and Dr. Jun Li at the University of Michigan. POP performs a Nelder and Mead Simplex search with external penalty function to select the most efficient Wageningen B series propeller for the given input constraints [33], [35]. Before POP can be run, the following inputs must be determined: blade number, required thrust, vehicle speed, wake fraction, depth of propeller shaft center line, water properties, and the maximum and minimum diameters acceptable. Knowledge of the depth of the propeller shaft centerline is

necessary for cavitation prevention calculations. For this application, the propeller should be sufficiently deep to prevent cavitation during normal operation, but to ensure a safety factor the depth was set at 5.625 in. This dimension represents the depth of the propeller shaft centerline on the *Deep 6* when the highest point on the vehicle (the upper aft fin) begins to break the surface. This depth represents the operating condition at which cavitation is most likely to occur. The vehicle speed was set at 4 knots as it was believed that this value was comparable to other AUV service speeds (see the comparison table provided in Appendix B). A blade number of 4 was selected because it reduced the potential for problematic vibrations from occurring as the propeller blades aligned and misaligned with the aft fins [25]. The blade number selected is also similar to that used for the Mark 14 torpedo [46]. In light of the previous discussion on the effects of a stern mounted screw propeller on a vessel's resistance, the required thrust must be increased beyond the measured "bare hull" resistance. The increase factor is known in the naval architecture community as thrust deduction,  $t$ . The calculation of the required thrust follows from Equation 2.3.1 [3], [25], [33]. The thrust deduction and its counterpart, the wake fraction, were determined with the assistance of the design charts provided in Allmendinger and in Burcher [3], [13]. To utilize the design charts, the ratio of the propeller diameter to the maximum hull diameter had to be known. Scaled measurements taken from pictures of AUVs with similar body form to the *Deep 6* revealed a common ratio of about 0.4. Using a propeller to hull diameter ratio of 0.4, the wake fraction read from both of the charts was approximately 0.40 [3], [13]. The thrust deduction value used for the design was taken from the Burcher chart, which yielded a value of +0.11 [13]. This value was used because it produced the larger and more conservative required

thrust. Only model tests can provide the actual values of thrust deduction and wake fraction, but the wake fraction value determined from the design charts corresponded closely with the value estimated from the Cosmos FloWorks computational fluid dynamics (CFD) simulation that was performed. The calculated required thrust for one of the *Deep 6*'s propellers was 1.28 lbf. The water properties that were used for the POP analysis were the default fresh water values. The final input quantities to be determined were the maximum and minimum acceptable propeller diameters. Actuator disk theory predicts that a larger, slower turning propeller will be more efficient than a smaller, faster turning one [33]. Therefore, the target propeller diameter of 3.00 in. (40% of the maximum hull diameter) was input into POP for the maximum allowable diameter. The minimum value was unimportant in this application and was selected to be 2 in. to reduce the amount of searching POP had to perform. The characteristics of the optimal propeller that POP selected for the *Deep 6* are presented in Table 2.3.1. Figure 2.3.3 displays the thrust coefficient, torque coefficient, and open water efficiency curves for the selected propeller. Figure 2.3.4 displays a picture of what the optimized propeller looks like.

---

**Equation 2.3.1: Required Thrust**

$$T = \frac{R_T}{(1-t)}$$

Where  $T$  is the required thrust,  $R_T$  is the “bare hull” total resistance, and  $t$  is the thrust deduction factor.

**Table 2.3.1: Optimal Propeller Characteristics**

Parameter	Abbreviation	Unit	Value
Diameter	$D_p$	inch	3.00
Pitch	P	inch	2.33
Pitch-Diameter Ratio	$P/D_p$	n.d.	0.778
Expanded Area Ratio	$A_e/A_o$	n.d.	0.471
Rate of Revolution	$N_{prop}$	rpm	1,912.2
Open Water Efficiency	$\eta_o$	%	58.8
Thrust	T	lbf	1.22

**Figure 2.3.3: Optimal Propeller Characteristic Curves**

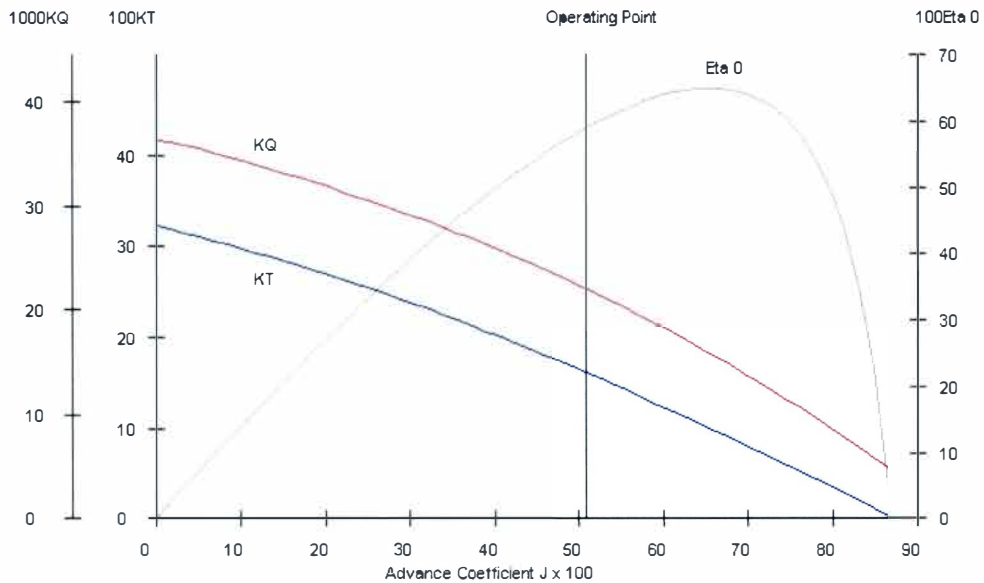


[Image generated using POP]



**Figure 2.3.4: Diagram of Optimal Propeller**

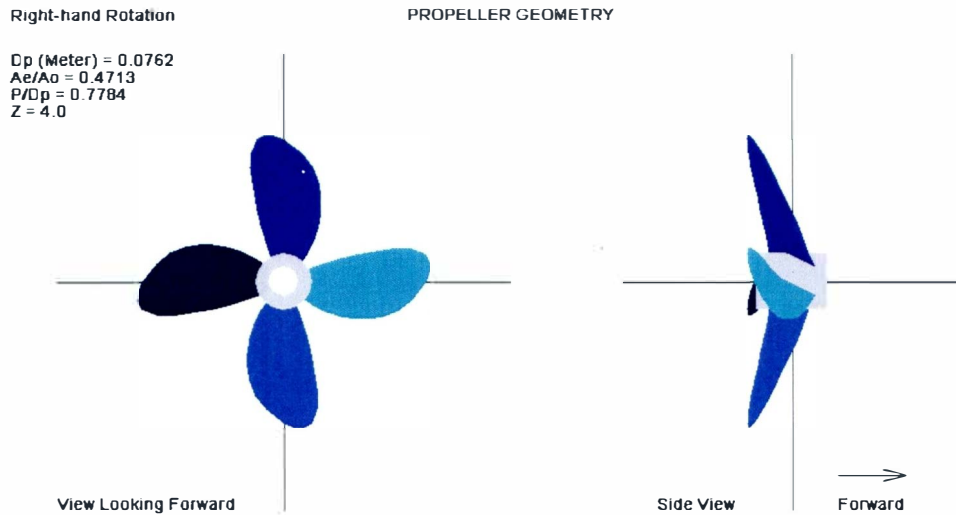


[Image generated using PropView]

Determining the specifications of the propeller drive motor was not within the scope of this research project. The standard naval architecture formulas used for engine sizing can be found in Allmendinger and in Lewis [3], [33]. For completeness of the preliminary design, epicyclical reduction gears would be used to mate the motor to the propeller shaft. This type of gear was selected for its compactness, allotting more room for payload.

## 2.4 Vehicle Mathematical Model

The previous three sections defined the overall vehicle design information for the *Deep 6*. After a suitable vehicle had been designed, it was possible to use the vehicle's dimensions to create a mathematical model of the vehicle. The parameters of the mathematical model were determined using analytical techniques. The subsequent model represents a first order approximation of the real world. Whenever possible, the

analytical estimates were compared against results generated using more advanced calculation techniques.

The mathematical model of the *Deep 6* accounts for the interactions between the vehicle and its aquatic environment from the perspective of a body fixed reference frame. The reason for this is that the interactions between the two depend upon the vehicle's orientation, shape, relative velocity, and relative acceleration. Figure 2.4.1 defines the body fixed coordinate system that is used throughout the remainder of this study. Figure 2.4.1 also provides the definition for positive forces, moments, and displacements that will be used for the subsequent simulation. Exceptions to the interaction forces and moments previously mentioned include gravity, water currents, and wave forcing. For the purpose of simplifying the mathematical model, the vehicle will operate at a depth sufficiently deep to allow the influence of surface disturbances to be ignored. The effects of surface disturbances decay exponentially with depth and therefore diminish to a negligible value within a short distance [15]. Other simplifying assumptions included are that the vehicle will operate far enough above the lake bottom that ground effects can be ignored, and that the fluid in which the vehicle operates is stationary [11]. These simplifying assumptions follow standard naval architecture practices for first order approximations [3], [34].

**Figure 2.4.1: Definition of the Vehicle Fixed Reference Frame**

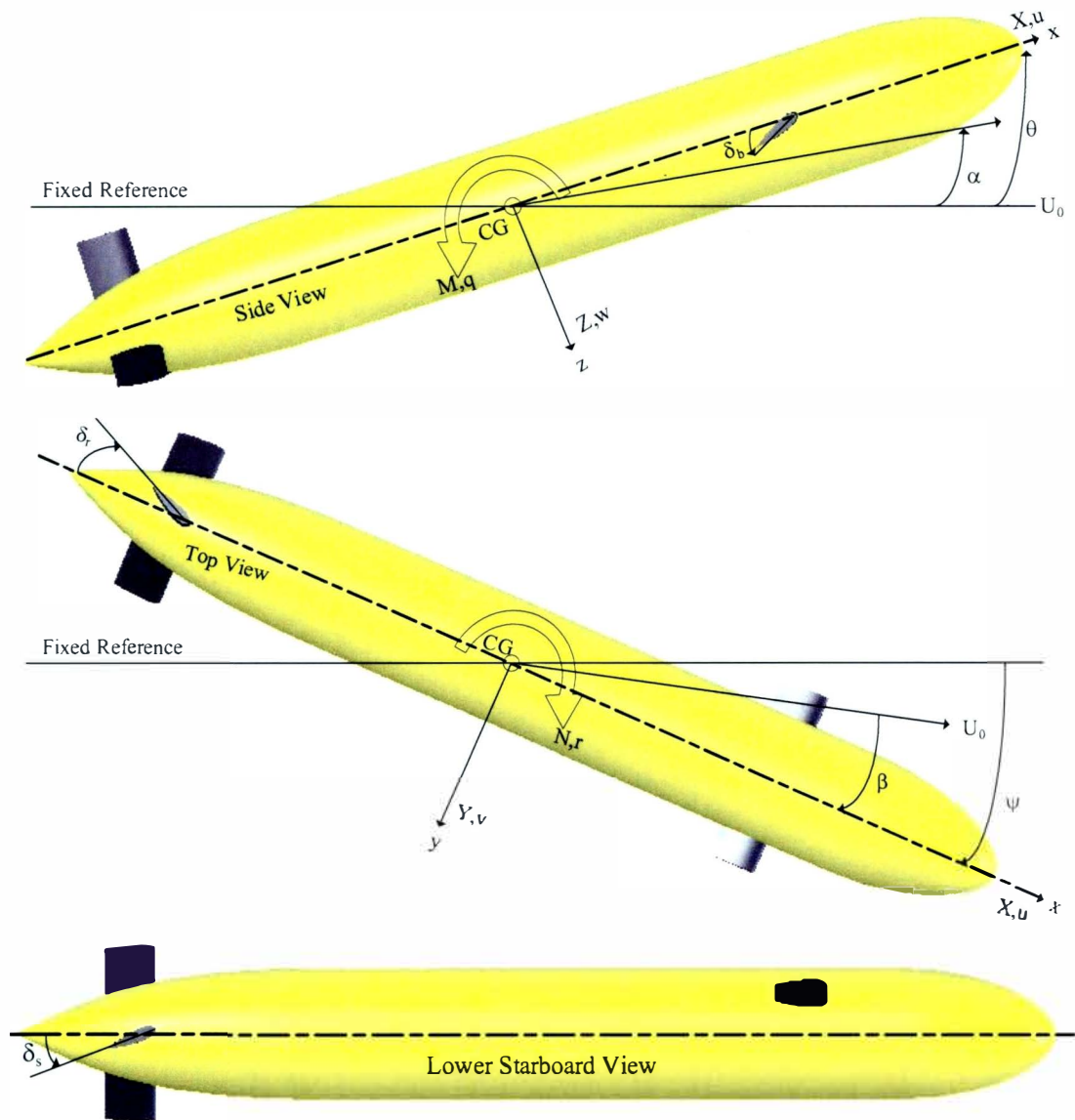
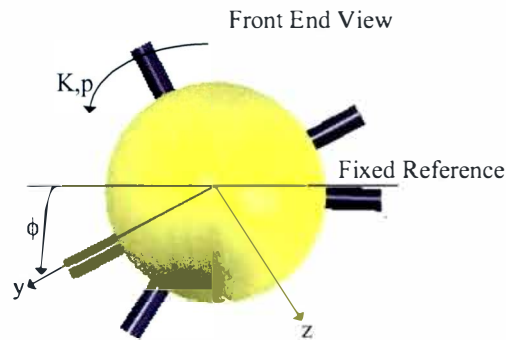


Figure 2.4.1 - Continued



The above diagram displays the orientation and placement of the vehicle fixed coordinate system used throughout this project. Also shown in the above figure are the definitions for positive control fin deflections, forces, and moments.

Note: To simplify the above figures only the top aft fin was deflected for the rudder deflection. In reality a positive rudder deflection would also require a positive deflection of the starboard aft fin and a negative deflection of the port aft fin. To produce no net rolling moment, all fins should have the same deflection magnitude.

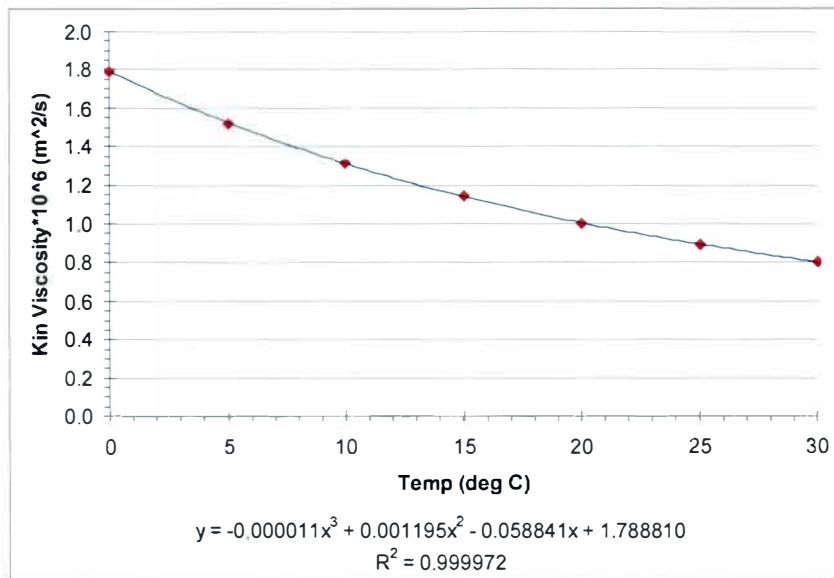
---

The next step towards the completion of the mathematical model was to determine the properties of the fluid in which the vehicle was to operate. The decision to design the *Deep 6* for operation within the Great Lakes mandated that the submerging fluid be fresh water. To provide the largest safety margin possible in the calculations, the water properties were selected for when water is at its densest. Fresh water's unique properties produce a maximum density at approximately 4°C [24], [31]. The high latitude of the Great Lakes renders the concept of the *Deep 6* operating in water at its densest completely plausible. The data for water at various temperatures was gathered from Newman [38]. To provide the most accurate values for the density and the kinematic viscosity for water at 4°C, the data presented by Newman was plotted and fit with regression curves [38]. The density data was reasonably fit with a line. The slope of the

presented for 5°C. The kinematic viscosity data was then fit with a 3<sup>rd</sup> order polynomial equation. Figure 2.4.2 displays the plot of the published data and the regression curve fit to it. The kinematic viscosity at 4°C estimated from the regression curve equation was  $1.58 \times 10^{-6} \text{ m}^2/\text{s}$ . This value differs enough from the published value for 5°C ( $1.52 \times 10^{-6} \text{ m}^2/\text{s}$ ) that the regression work was clearly justified. This information is necessary for the calculation of the vehicle's Reynolds Number (which is necessary for drag calculations) and displacement.

---

**Figure 2.4.2: Regression Fit of Fresh Water Kinematic Viscosity Data**



---

The first model parameters to be determined were those that could be calculated through integration of the hull profile. Since the profile could be described using a piecewise continuous equation, all of the integrations were able to be determined exactly [45]. Had this not been the case, the integrations could have been approximated by using Simpon's

Rule or other finite summation processes [50]. The most obvious of the profile integration quantities was the displaced volume. The total displaced volume was calculated as the sum of the hull volume and the five control fin volumes. The displacement and its associated buoyant force were calculated as the product of the vehicle displacement and the water density [24], [50]. The CB is the location in space through which the resultant buoyant force vector can be assumed to act. The location of the center of buoyancy coincides with the centroid of the displaced volume [50]. The vehicle was made to be neutrally buoyant (vehicle weight is equal in magnitude with the buoyant force). This assumption is standard practice for the preliminary design of underwater vehicles since the actual vehicle weight will not be known until completion of the component level design [3], [13]. Neutral buoyancy simplified the EOM and allowed the vehicle to move laterally without deflecting the bow and/or stern planes. After an estimate for the vehicle's weight had been determined, the associated mass could be determined by dividing by the acceleration due to gravity. The CG is the location in space through which the resultant weight vector can be assumed to act [24], [50]. To maintain the intended static vehicle posture, the CG and the CB must lie along the same vertical line. To obtain dynamic stability, the CG must also be located below the CB on that vertical line. The further the CG is located below the CB the larger the righting moment produced when the vehicle rolls [50]. During this study, the rolling motions were not desired; therefore, the center of gravity was located 1.25 in. (approximately 33% of the maximum hull radius) below the CB. The inertia matrix for the *Deep 6* was determined once the mass and profile curve were known. Equations 2.4.1 – 2.4.6 show the equations used to calculate the elements of the inertia matrix [9]. Since the

component level design has not been completed, the mass distribution within the *Deep 6* is unknown. For the purposes of preliminary design, the mass distribution has been estimated to be uniformly distributed based upon volume. The *Deep 6*'s wetted surface area was analytically determined as the sum of the exposed surface area of its individual components. The surface area of the *Deep 6*'s hull was approximated both by integration of the profile curve and empirical formula presented by Jackson [29], [45]. The equation presented by Jackson that was used to estimate the hull wetted surface area has been provided in Equation 2.4.7 [29]. Both of these values were in reasonable agreement with each other, however, the value determine through integration was determined specifically for the *Deep 6*. For this reason, the integration area value was selected to be used for the mathematical model.

---

**Equation 2.4.1: Mass Moment of Inertia About the Longitudinal Axis**

$$I_{xx}^G = \int_B (y^2 + z^2) dm$$

**Equation 2.4.2: Mass Moment of Inertia About the Transverse Axis**

$$I_{yy}^G = \int_B (x^2 + z^2) dm$$

**Equations 2.4.3: Mass Moment of Inertia About the Vertical Axis**

$$I_{zz}^G = \int_B (x^2 + y^2) dm$$

**Equation 2.4.4: Product of Inertia for X-Y Plane Symmetry**

$$I_{xy}^G = \int_B (xy) dm$$

**Equation 2.4.5: Product of Inertia for X-Z Plane Symmetry**

$$I_{xz}^G = \int_B (xz) dm$$

**Equation 2.4.6: Product of Inertia for Y-Z Plane Symmetry**

$$I_{yz}^G = \int_B (yz) dm$$

Where  $I_{*#}^G$  is the mass moment of inertia or product of inertia with respect to the body's center of gravity, x, y, and z are measured from the particular axis under consideration, and the inertia matrix is:

$$[I_G] = \begin{bmatrix} I_{xx}^G & -I_{xy}^G & -I_{xz}^G \\ -I_{xy}^G & I_{yy}^G & -I_{yz}^G \\ -I_{xz}^G & -I_{yz}^G & I_{zz}^G \end{bmatrix}$$

**Equation 2.4.7: Empirical Hull Surface Area Formula**

$$S = \pi D^2 \left[ \frac{L}{D} - K2 \right]$$

Where  $S$  is the hull wetted surface area,  $D$  is the hull maximum diameter,  $\frac{L}{D}$  is the hull's slenderness ratio, and  $K2$  is a parameter that can either be read off of the design chart presented by Jackson or calculated by

$$K2 = 6 - n_f C_{ws_f} - n_a C_{ws_a}$$

should estimates for the forward and after wetted surface area coefficients,  $C_{ws}$ , be known.  $n_f$  and  $n_a$  are the nose and tail shape coefficients, respectively, used to describe a hull Jackson hull profile [29].

---

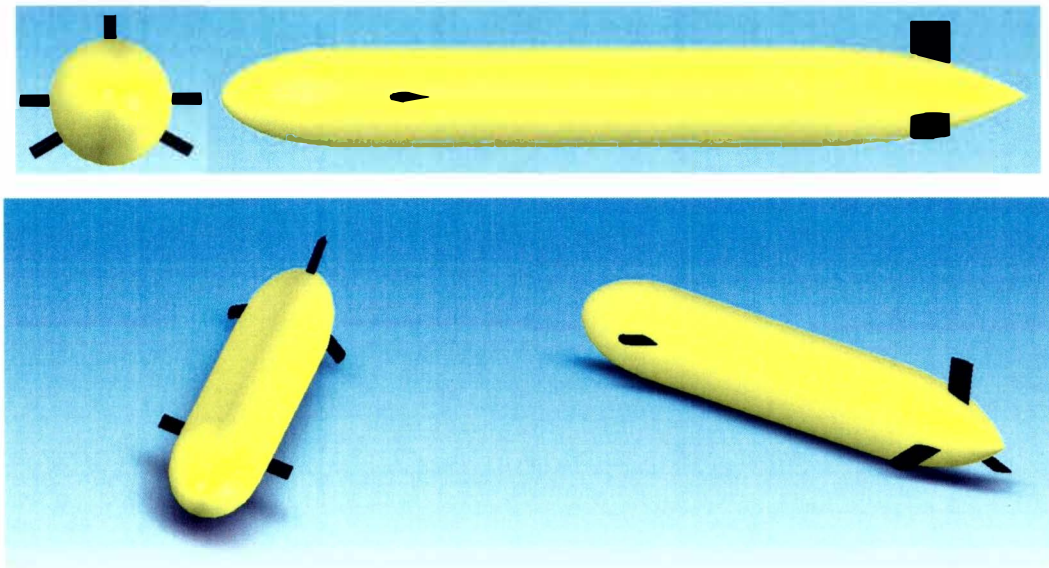
To validate the aforementioned analytically determined parameters, measurements were taken using a 3D model of the *Deep 6* that was created using SolidWorks. The hull of the *Deep 6* was made by revolving the profile curve around a stationary axis. The profile curve was discretized in Microsoft Excel into a series of "X-Y" points with a longitudinal spacing of 0.15 in. and then imported into SolidWorks (which automatically fit the points with a spline). A similar procedure was performed for the NACA 0025 profile curve that was used for the control fins. Figure 2.4.3 provides some renderings of the 3D model that was created. It was possible to quickly determine the vehicle's displaced volume,



centroid of volume, exposed (“wetted”) surface area, total mass, and inertia matrix using the measure mass properties command. The values provided by SolidWorks were in good agreement with the analytical values previously calculated. However, the values determined by SolidWorks were determined much quicker and to a much higher level of precision.

---

**Figure 2.4.3: 3D Renderings of the *Deep 6***



---

The implementation of the 3D modeling software package allowed for clear visualization of the vehicle geometry. By constraining the control fins to their drive shafts with an angular dimension, it was possible to quickly and easily view the fins at various orientations. This capability allowed for the determination of the proper spacing and taper angle for the rear fins. The proper spacing was determined to be between 0.06 in. and 0.09 in. with a taper angle of  $15^\circ$ . These dimensions would allow the rear fins to rotate about their quarter chord point from  $+90^\circ$  to  $-90^\circ$  without intersecting the hull.

The mathematical model of the *Deep 6* also included information regarding the hull drag. To provide a complete description of the drag, estimates for the longitudinal, transverse, and vertical drag coefficients were required. Drag coefficients are commonly non-dimensionalized by using the equation shown in Equation 2.4.8 [20]. To avoid the possibility of comparing drag coefficients that were non-dimensionalized using differing characteristic dimensions, all drag calculations were carried out using dimensionalized quantities until the final results were obtained. The longitudinal drag was calculated first, and was performed using the standard naval architecture equations shown in Equations 2.4.9 and the design chart presented by Burcher and Rydill [13], [25], [33]. The drag calculation required that the Reynolds Number (using the hull LOA as the characteristic length) be determined. The formula used to calculate the Reynolds Number is shown in Equation 2.4.10. Equations 2.4.9 in conjunction with the design chart predicted an axial drag for the *Deep 6* hull of approximately 2.11 lbf., 1.68 lbf. of that being due to frictional resistance. The results from the hull drag calculation provided support for the assumption that most marine vehicles and all underwater vehicle's drag is dominated by frictional drag [3], [13], [33]. The predicted drag for the control fins was added to the hull drag to produce a total axial drag of 2.12 lbf. The data used for the control fin drag prediction was gathered from the experimental test results for the NACA 0025 foil section published by Abbot and VonDoenhoff, Bullivant, and Lewis [1], [13], [33]. The primary source for data for the control fins, though, was that presented by Lewis because it presented data for straight, low aspect ratio sections that were attached to a flat body on one end (as apposed the to "infinitely" long section data presented elsewhere) [33]. The data published by Lewis was most representative of the situation present on the *Deep 6*.

---

**Equation 2.4.8: Drag Coefficient Definition**

$$C_D = \frac{D}{\frac{1}{2}\rho A v^2}$$

Where  $C_D$  is the non-dimensionalized drag coefficient,  $D$  is the dimensional drag,  $\rho$  is the mass density of the fluid,  $A$  is the characteristic area, and  $v$  is the relative velocity between the fluid and the body.

Note: Typically, in naval architecture the characteristic area is the wetted surface area. However, this may not always be the case, especially if when using design tables generated by different industry sectors. The characteristic area may also be the body volume raised to the two thirds power, the square of the body length, the projected area normal to the flow, or any other combination of parameters that results in an area.

Care must be taken to always dimensionalize and non-dimensionalize drag values as defined by the reference in use to provide a just comparison [1], [20], [33].

**Equations 2.4.9: Longitudinal Drag Coefficient Equations**

Equation 2.4.9a:

$$C_{T_S} = C_{F_S} + C_R + C_A$$

Where  $C_{T_S}$  is the total resistance of the full scale vehicle,  $C_{F_S}$  is the frictional resistance of the full scale vehicle,  $C_R$  is the residuary resistance, and  $C_A$  is the correlation allowance between residuary measurements taken at the model scale and their full scale counterparts.

Note: Since there is little to no wave making resistance for the *Deep 6* under normal operating conditions, the residuary resistance is comprised primarily of the form/viscous pressure drag. The correlation allowance has been included in the calculations to correct for any discrepancies accumulated through the use of model scale residuary resistance measurements.

Equation 2.4.9b:

$$C_F = \frac{0.075}{(\log_{10} Re - 2)^2}$$

Where  $C_F$  is the frictional resistance (either model or full scale) and  $Re$  is the Reynolds Number associated with the vehicle.

Note: Equation 2.4.1b represents the equation for the ITTC 1957 flat plate friction line.

#### Equation 2.4.10: Definition of the Reynolds Number

$$Re = \frac{vL}{\nu}$$

Where  $Re$  is the Reynolds Number,  $v$  is the relative velocity between the fluid and the body,  $L$  is the characteristic length, and  $\nu$  is the kinematic viscosity of the fluid.

Note: The characteristic length in naval architecture is typically the LOA. However, this may not always be the case, especially when using design charts generated by different industry sectors. The characteristic length may also be defined as the cube root of the body volume, the square root of the wetted surface area, or the width of the body. Care must be taken to calculate the Reynolds Number as it is defined by the provided data [20], [33].

---

The transverse and vertical drag could have been estimated in a similar fashion to the longitudinal drag, but a source of data for the residuary resistance that applied to these two conditions could not be located. However, published data for the total drag coefficient around a circular profile and against a flat plate (representative of the control fins) was available from Fox and McDonald [20]. As with the longitudinal case, the total drag in the transverse and the vertical directions was calculated as the sum of the hull drag and the control fin drag. The design charts presented by Fox and McDonald non-dimensionalized the drag by the projected area normal to the flow [20]. The projected area for the hull was determined both by integration of the hull profile and by the measures section properties command in SolidWorks. The drag coefficients presented by Fox and McDonald are for laminar flows only, requiring that the values be adjusted to accommodate the existence of a turbulent transition somewhere along the hull. Fox and McDonald stated that drag measurements over a circular cylinder with turbulent boundary layer flow could be as much as 4 times smaller than their laminar counterpart (due to a lower separation point) [20]. A reduction factor of 2.5 was used to account for turbulent boundary layer flow over only a portion of the hull. The reduction factor was

determined using the ratio of areas estimated to experience laminar and turbulent flows. The transition between laminar and turbulent flow was assumed to occur completely once a local Reynolds Number of 500,000 (characteristic length being the flow path, or hull circumference) was achieved [21]. The final drag measurements for the transverse and vertical directions were 67.9 lbf. and 72.0 lbf., respectively. It should be noted that for the transverse direction calculations, the second of the two lower control fins was not counted as a complete fin. The second fin's close proximity to the first led to the use of a scaling factor of 0.5 to account for the fact that the second fin should be almost completely contained within the first fin's wake, thus not exposed to the full brunt of the flow [33].

To validate the analytical drag calculations two preliminary and independent computational fluid dynamics (CFD) analyses were performed. The first CFD analysis that was performed utilized the SolidWorks CFD add-in, Cosmos FloWorks. The total longitudinal drag predicted by FloWorks was 2.29 lbf., 1.80 lbf. resulting from skin friction. The vertical drag predicted by FloWorks was 72.1 lbf. The second CFD analysis that was performed utilized FLUENT. The longitudinal drag that was predicted using FLUENT was 1.91 lbf. The purpose of this investigation was not to obtain a perfect hydrodynamics model of the flow around the *Deep 6*, but rather to validate the analytical drag predictions that were calculated. No claims of correctness are made for the drag value determined by any one of the three methods. However, the good agreement between the values determined by the three methods implies that the actual drag values are most likely close to those predicted. Appendix E contains some sample

results generated from the preliminary CFD analyses. The slight discrepancy between the drag results was acceptable for the purposes of the first order mathematic model and the preliminary design since the differences will be adequately absorbed into the design margin for the powering calculation [33].

The next set of parameters to be determined for the mathematical model of the *Deep 6* was added mass and hydrodynamic damping. “Added mass” is an engineering construct used to describe the effects of the entrained fluid moving around a body. Added mass is typically adopted so that the complex hydrodynamics associated with the body accelerating can be removed from the system. To include the additional force required to accelerate the entrained fluid when the body accelerates, the mass of the body is arbitrarily increased by the quotient of the extra force and the acceleration (which results in a mass term). The “heavier” body therefore requires a larger force for it to accelerate – the force being the sum of the force to accelerate the body’s mass and the force required to accelerate the entrained fluid [34]. The added mass and hydrodynamic damping terms are heavily based upon the geometry of the vehicle [19], [38]. These terms are probably the most difficult of all of the required model parameters to approximate. The difficulty associated with achieving analytical computation of these parameters is commonly overcome by performing physical testing to determine either all or most of the parameters. Recall that for this project it was desired to fully determine reasonable approximations for a complete vehicle model through analytical methods. The research presented by Humphrey and Watkinson provided empirical formulas for the added mass of a submarine that were determined from trend lines fit to experimental data collected

during systematic testing of submarine models [26]. The formulas presented by Humphrey and Watkinson were especially useful because they considered the additional effects of hull appendages and asymmetrical hull shapes, which were not considered in the analytical methods presented by Fossen and Newman [19], [38]. Another benefit of the data presented by Humphrey and Watkinson were the discussions of how well the formulas predicted reality. The high density of water renders the inclusion of the added mass and hydrodynamic damping parameters essential for the construction of an accurate underwater vehicle model. This requirement constitutes the key difference between an aircraft and an underwater vehicle mathematical model [41]. The added mass and damping parameters describe the resistive forces that will be exerted upon the vehicle as it attempts to perform various maneuvers (such as turning, pitching, and control fin deflections). These parameters are partially responsible for the coupling that may exist between vehicle motions [26], [41]. Verification of the added mass and damping parameters was sought. HYCOEF is the only program known that is able to determine these quantities. This program was developed by the United States Navy and is not available to the public [37]. Therefore, no independent verification of the added mass and damping parameters was obtained.

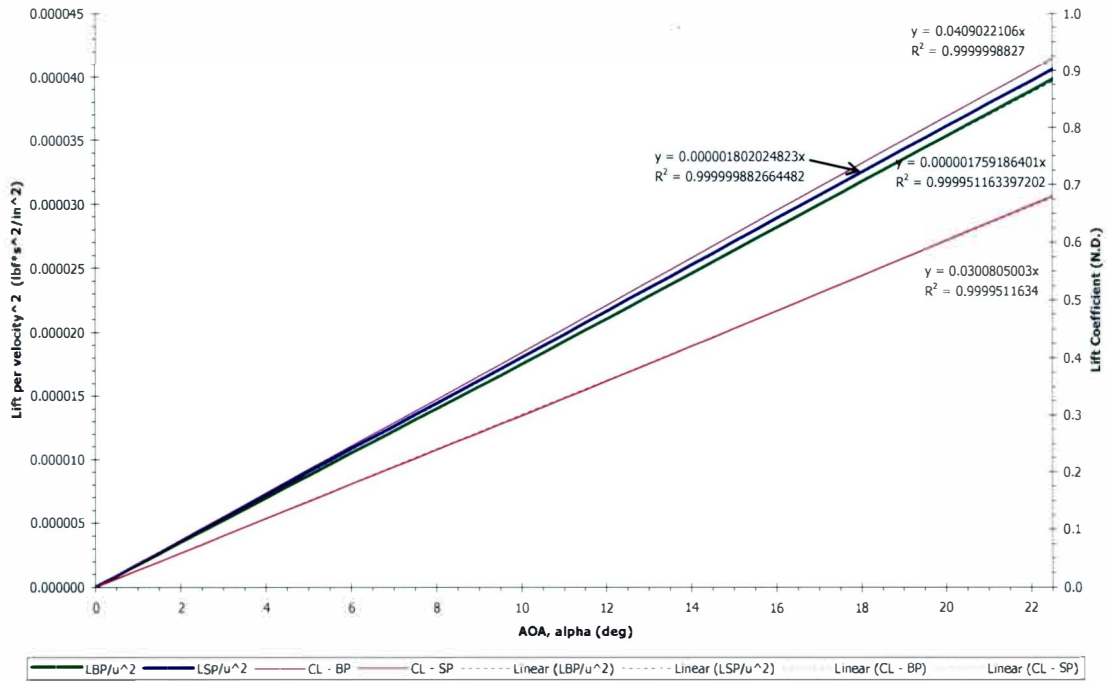
The final parameters required to complete the mathematical model of the *Deep 6* were the influence effects of the control parameters. The only parameters available for control on the *Deep 6* are the deflection angles of the control fins and the rate of revolution for the propellers. The five fins on the *Deep 6* exert control over the vehicle by deflecting, which produces an angle of attack (AOA) relative to the inflow to the vehicle, which

results in the generation of a lift force and additional drag [1], [3], [34]. The forces generated by the fins create moments about the vehicle CG, which result in the appropriate vehicle rotations. The rate of revolution of the propellers exerts control over the vehicle's speed by altering the amount of thrust generated. Nothing special had to be determined for the modeling of the propeller rpm control parameter due the manner in which it was handled within the equations of motion (this will be discussed further within Section 3.1 of this report). The controlling effects of the fin deflections were determined through the use of regression plots for the measured drag and lift for the NACA 0025 section at various angles of attack [1], [12], [34]. The regression plots that were created for the lift and drag of the control fins are shown in Figures 2.4.4 and 2.4.5. Again, the data presented by Lewis served as the primary source of information for the plots because it best represented the configuration present on the *Deep 6* [34]. To achieve a linear drag relationship for use within the vehicle equations of motion, the drag data was plotted against the square of the attack angle (the usual relationship between drag and angle of attack is parabolic). The slope of the regression lines fitted to the plotted data served as the input value for the control effect of each fin per degree of deflection. It was assumed that the lift and drag measurements would exhibit the behavior of an odd function. This behavior should occur since the chord line for the fin profile is also a line of symmetry. Once the additional lift and drag forces per degree of deflection were determined, the additional moments per deflection were calculated by multiplying the distance between a particular control fin and the vehicle CG by the appropriate force generated. The foil data presented by Lewis predicts a stall angle of  $45^\circ$  for a low aspect fin using a NACA



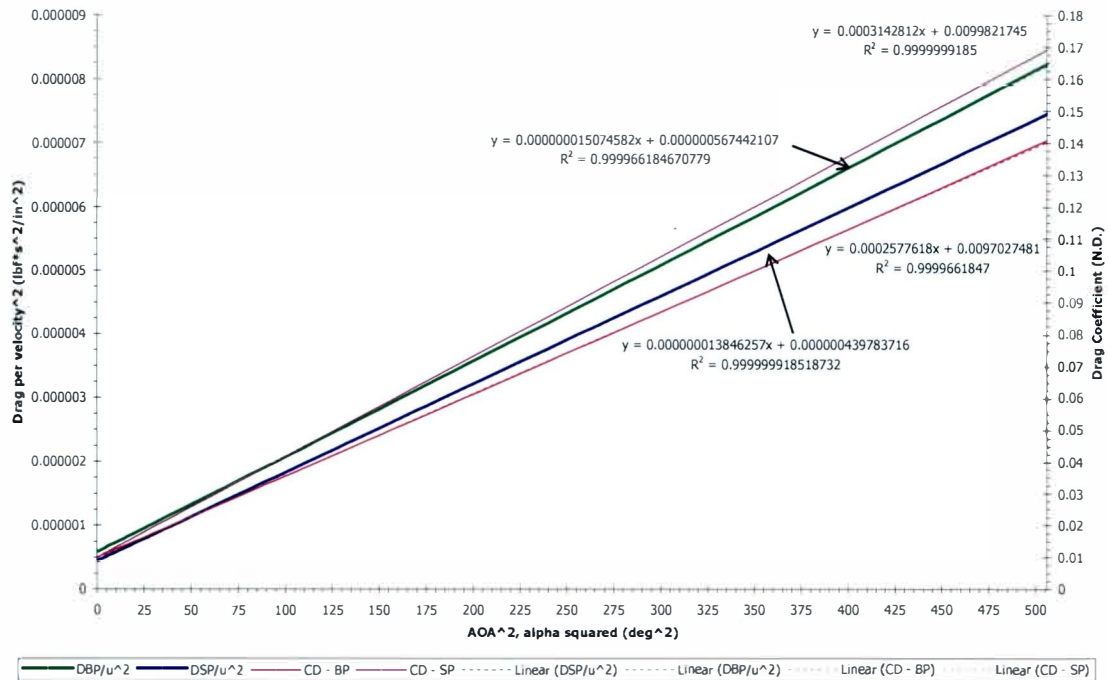
0025 profile [34]. To retain conservatism in the calculations, the maximum fin deflection for all of the control fins was set to  $\pm 22.5^\circ$ .

**Figure 2.4.4: Regression Plot of Control Fin Lift vs. Angle of Attack**



Note: The crossing the regression lines at the origin reveal the already known fact that at zero angle of attack the fins produce no lift. The zero crossing is one indication that the lines have proper form.

**Figure 2.4.5: Regression Plot of Control Fin Drag vs. Angle of Attack Squared**



Note: The “y-intercept” at zero angle of attack that exists for the drag regression lines reveal that the fins do, in fact, have parasite drag. The existence of the parasite drag confirms the already known fact that the control fins produce a drag force at all angles of attack. The magnitude of the parasite drag predicted by the regression lines closely matches the experimentally measured values.

At this point, the preliminary design and mathematical modeling of the *Deep 6* was completed. Table 2.4.1 presents a summary of the parameters that were determined for the vehicle in the previous sections.

**Table 2.4.1: Deep 6 Mathematical Modeling Parameters**

Variable	Description	Units*	Value
$\rho_m$	mass density of fluid medium (fresh water)	$\text{lb}_f \cdot \text{s}^2 / \text{in}^4$	9.357E-05
$g$	acceleration due to gravity	$\text{in} / \text{s}^2$	3.861E+02
$l$	(hull/characteristic) length	in	6.000E+01
$D$	hull maximum diameter	in	7.500E+00
$L/D$	slenderness ratio	n.d.	8.000E+00
$S$	wetted surface area	$\text{in}^2$	1.349E+03
$C_b$	block coefficient	n.d.	6.540E-01
$\nabla$	displaced volume	$\text{in}^3$	2.226E+03
$B$	buoyant force	$\text{lb}_f$	8.044E+01
$W$ or $\Delta$	weight/displacement	$\text{lb}_f$	8.044E+01
$m$	mass	$\text{lb}_f \cdot \text{s}^2 / \text{in}$	2.083E-01
$x_G$	longitudinal position of CG	in	2.835E+01
$y_G$	transverse position of CG	in	0.000E+00
$z_G$	vertical position of CG	in	1.250E+00
$x_B$	longitudinal position of CB	in	2.835E+01
$y_B$	transverse position of CB	in	0.000E+00
$z_B$	vertical position of CB	in	8.300E-04
$I_{xx}$	mass moment of inertia about lon. axis	$\text{in} \cdot \text{lb}_f \cdot \text{s}^2$	5.376E+02
$I_{yy}$	mass moment of inertia about trans. axis	$\text{in} \cdot \text{lb}_f \cdot \text{s}^2$	1.786E+04
$I_{zz}$	mass moment of inertia about vert. axis	$\text{in} \cdot \text{lb}_f \cdot \text{s}^2$	1.786E+04
$I_{xy}$	cross product of inertia	$\text{in} \cdot \text{lb}_f \cdot \text{s}^2$	-3.440E-03
$I_{xz}$	cross product of inertia	$\text{in} \cdot \text{lb}_f \cdot \text{s}^2$	1.072E+00
$I_{yz}$	cross product of inertia	$\text{in} \cdot \text{lb}_f \cdot \text{s}^2$	-5.300E-04
$Re$	Reynolds Number (using LOA)	n.d.	1.988E+06
$X_{u\dot{d}ot}$	added mass	$\frac{1}{2}\rho l^3$	-8.304E-04
$X_{v\dot{d}ot}$	added mass	$\frac{1}{2}\rho l^3$	0.000E+00
$X_{w\dot{d}ot}$	added mass	$\frac{1}{2}\rho l^3$	0.000E+00
$X_{p\dot{d}ot}$	added mass	$\frac{1}{2}\rho l^4$	0.000E+00
$X_{q\dot{d}ot}$	added mass	$\frac{1}{2}\rho l^4$	0.000E+00
$X_{r\dot{d}ot}$	added mass	$\frac{1}{2}\rho l^4$	0.000E+00
$X_{uu}$	coupled added mass cross term	$\frac{1}{2}\rho l^3$	0.000E+00
$X_{uv}$	coupled added mass cross term	$\frac{1}{2}\rho l^3$	0.000E+00
$X_{uw}$	coupled added mass cross term	$\frac{1}{2}\rho l^3$	0.000E+00
$X_{up}$	coupled added mass cross term	$\frac{1}{2}\rho l^3$	0.000E+00
$X_{uq}$	coupled added mass cross term	$\frac{1}{2}\rho l^3$	0.000E+00
$X_{ur}$	coupled added mass cross term	$\frac{1}{2}\rho l^3$	0.000E+00
$X_{vv}$	coupled added mass cross term	$\frac{1}{2}\rho l^3$	0.000E+00
$X_{vw}$	coupled added mass cross term	$\frac{1}{2}\rho l^3$	0.000E+00

Table 2.4.1 - Continued

$X_{vp}$	coupled added mass cross term	$\frac{1}{2}\rho l^3$	0.000E+00
$X_{vq}$	coupled added mass cross term	$\frac{1}{2}\rho l^3$	0.000E+00
$X_{vr}$	coupled added mass cross term	$\frac{1}{2}\rho l^3$	1.960E-02
$X_{ww}$	coupled added mass cross term	$\frac{1}{2}\rho l^3$	0.000E+00
$X_{wp}$	coupled added mass cross term	$\frac{1}{2}\rho l^3$	0.000E+00
$X_{wq}$	coupled added mass cross term	$\frac{1}{2}\rho l^3$	-2.009E-02
$X_{wr}$	coupled added mass cross term	$\frac{1}{2}\rho l^3$	0.000E+00
$X_{pp}$	coupled added mass cross term	$\frac{1}{2}\rho l^4$	0.000E+00
$X_{pq}$	coupled added mass cross term	$\frac{1}{2}\rho l^3$	0.000E+00
$X_{pr}$	coupled added mass cross term	$\frac{1}{2}\rho l^4$	4.145E-04
$X_{qq}$	coupled added mass cross term	$\frac{1}{2}\rho l^4$	-3.932E-03
$X_{qr}$	coupled added mass cross term	$\frac{1}{2}\rho l^4$	0.000E+00
$X_{rr}$	coupled added mass cross term	$\frac{1}{2}\rho l^4$	-7.939E-05
$X_{uq\delta b}$	coupled added mass due to fin movement	$\frac{1}{2}\rho l^3 * \delta$	0.000E+00
$X_{uq\delta s}$	coupled added mass due to fin movement	$\frac{1}{2}\rho l^3 * \delta$	0.000E+00
$X_{ur\delta r}$	coupled added mass due to fin movement	$\frac{1}{2}\rho l^3 * \delta$	0.000E+00
$X_{uv\delta r}$	coupled added mass due to fin movement	$\frac{1}{2}\rho l^3 * \delta$	0.000E+00
$X_{uw\delta b}$	coupled added mass due to fin movement	$\frac{1}{2}\rho l^3 * \delta$	0.000E+00
$X_{uw\delta s}$	coupled added mass due to fin movement	$\frac{1}{2}\rho l^3 * \delta$	0.000E+00
$X_{u u \delta b\delta b}$	additional Xdrag due to BP deflection	$u^2 * \delta^2$	1.507E-08
$X_{u u \delta s\delta s}$	additional Xdrag due to SP deflection	$u^2 * \delta^2$	2.769E-08
$X_{u u \delta r\delta r}$	additional Xdrag due to rudder deflection	$u^2 * \delta^2$	4.154E-08
$C_{dx}$	lon. drag coefficient	$u^2$	3.482E-04
$Y_{u\dot{u}}$	added mass	$\frac{1}{2}\rho l^3$	0.000E+00
$Y_{v\dot{v}}$	added mass	$\frac{1}{2}\rho l^3$	-1.960E-02
$Y_{w\dot{w}}$	added mass	$\frac{1}{2}\rho l^3$	0.000E+00
$Y_{p\dot{p}}$	added mass	$\frac{1}{2}\rho l^4$	-4.145E-04
$Y_{q\dot{q}}$	added mass	$\frac{1}{2}\rho l^4$	0.000E+00
$Y_{r\dot{r}}$	added mass	$\frac{1}{2}\rho l^4$	7.939E-05
$Y_{uu}$	coupled added mass cross term	$\frac{1}{2}\rho l^3$	0.000E+00
$Y_{uv}$	coupled added mass cross term	$\frac{1}{2}\rho l^3$	0.000E+00
$Y_{uw}$	coupled added mass cross term	$\frac{1}{2}\rho l^3$	0.000E+00
$Y_{up}$	coupled added mass cross term	$\frac{1}{2}\rho l^3$	0.000E+00
$Y_{uq}$	coupled added mass cross term	$\frac{1}{2}\rho l^3$	0.000E+00
$Y_{ur}$	coupled added mass cross term	$\frac{1}{2}\rho l^3$	-8.304E-04
$Y_{vv}$	coupled added mass cross term	$\frac{1}{2}\rho l^3$	0.000E+00
$Y_{vw}$	coupled added mass cross term	$\frac{1}{2}\rho l^3$	0.000E+00
$Y_{vp}$	coupled added mass cross term	$\frac{1}{2}\rho l^3$	0.000E+00

Table 2.4.1 - Continued

$Y_{vq}$	coupled added mass cross term	$\frac{1}{2}\rho l^3$	0.000E+00
$Y_{vr}$	coupled added mass cross term	$\frac{1}{2}\rho l^3$	0.000E+00
$Y_{ww}$	coupled added mass cross term	$\frac{1}{2}\rho l^3$	0.000E+00
$Y_{wp}$	coupled added mass cross term	$\frac{1}{2}\rho l^3$	2.009E-02
$Y_{wq}$	coupled added mass cross term	$\frac{1}{2}\rho l^3$	0.000E+00
$Y_{wr}$	coupled added mass cross term	$\frac{1}{2}\rho l^3$	0.000E+00
$Y_{pp}$	coupled added mass cross term	$\frac{1}{2}\rho l^4$	0.000E+00
$Y_{pq}$	coupled added mass cross term	$\frac{1}{2}\rho l^3$	3.932E-03
$Y_{pr}$	coupled added mass cross term	$\frac{1}{2}\rho l^4$	0.000E+00
$Y_{qq}$	coupled added mass cross term	$\frac{1}{2}\rho l^4$	0.000E+00
$Y_{qr}$	coupled added mass cross term	$\frac{1}{2}\rho l^4$	0.000E+00
$Y_{rr}$	coupled added mass cross term	$\frac{1}{2}\rho l^4$	0.000E+00
$Y_{u u \dot{\delta}r}$	Y fin lift force due to bow rudder	$u^2 \cdot \dot{\delta}$	0.000E+00
$Y_{u u \dot{\delta}s}$	Y fin lift force due to stern planes	$u^2 \cdot \dot{\delta}$	0.000E+00
$Y_{u u \dot{\delta}rs}$	Y fin lift force due to (stern) rudder	$u^2 \cdot \dot{\delta}$	3.604E-06
$C_{dy}$	trans. drag coefficient	$u^2$	1.035E-02
$Z_{u\dot{u}}$	added mass	$\frac{1}{2}\rho l^3$	0.000E+00
$Z_{v\dot{v}}$	added mass	$\frac{1}{2}\rho l^3$	0.000E+00
$Z_{w\dot{w}}$	added mass	$\frac{1}{2}\rho l^3$	-2.009E-02
$Z_{p\dot{p}}$	added mass	$\frac{1}{2}\rho l^4$	0.000E+00
$Z_{q\dot{q}}$	added mass	$\frac{1}{2}\rho l^4$	-3.932E-03
$Z_{r\dot{r}}$	added mass	$\frac{1}{2}\rho l^4$	0.000E+00
$Z_{uu}$	coupled added mass cross term	$\frac{1}{2}\rho l^3$	0.000E+00
$Z_{uv}$	coupled added mass cross term	$\frac{1}{2}\rho l^3$	0.000E+00
$Z_{uw}$	coupled added mass cross term	$\frac{1}{2}\rho l^3$	0.000E+00
$Z_{up}$	coupled added mass cross term	$\frac{1}{2}\rho l^3$	0.000E+00
$Z_{uq}$	coupled added mass cross term	$\frac{1}{2}\rho l^3$	8.304E-04
$Z_{ur}$	coupled added mass cross term	$\frac{1}{2}\rho l^3$	0.000E+00
$Z_{vv}$	coupled added mass cross term	$\frac{1}{2}\rho l^3$	0.000E+00
$Z_{vw}$	coupled added mass cross term	$\frac{1}{2}\rho l^3$	0.000E+00
$Z_{vp}$	coupled added mass cross term	$\frac{1}{2}\rho l^3$	-1.960E-02
$Z_{vq}$	coupled added mass cross term	$\frac{1}{2}\rho l^3$	0.000E+00
$Z_{vr}$	coupled added mass cross term	$\frac{1}{2}\rho l^3$	0.000E+00
$Z_{ww}$	coupled added mass cross term	$\frac{1}{2}\rho l^3$	0.000E+00
$Z_{wp}$	coupled added mass cross term	$\frac{1}{2}\rho l^3$	0.000E+00
$Z_{wq}$	coupled added mass cross term	$\frac{1}{2}\rho l^3$	0.000E+00
$Z_{wr}$	coupled added mass cross term	$\frac{1}{2}\rho l^3$	0.000E+00
$Z_{pp}$	coupled added mass cross term	$\frac{1}{2}\rho l^4$	-4.145E-04

Table 2.4.1 - Continued

$Z_{pq}$	coupled added mass cross term	$\frac{1}{2}\rho l^3$	0.000E+00
$Z_{pr}$	coupled added mass cross term	$\frac{1}{2}\rho l^4$	7.939E-05
$Z_{qq}$	coupled added mass cross term	$\frac{1}{2}\rho l^4$	0.000E+00
$Z_{qr}$	coupled added mass cross term	$\frac{1}{2}\rho l^4$	0.000E+00
$Z_{rr}$	coupled added mass cross term	$\frac{1}{2}\rho l^4$	0.000E+00
$Z_{u u \delta b}$	Z fin lift force due to bow planes	$u^2 * \delta$	1.759E-06
$Z_{u u \delta s}$	Z fin lift force due to stern planes	$u^2 * \delta$	3.121E-06
$Cdz$	vert. drag coefficient	$u^2$	1.098E-02
$K_{u\dot{u}}$	added mass	$\frac{1}{2}\rho l^4$	0.000E+00
$K_{v\dot{v}}$	added mass	$\frac{1}{2}\rho l^4$	-4.145E-04
$K_{w\dot{w}}$	added mass	$\frac{1}{2}\rho l^4$	0.000E+00
$K_{p\dot{p}}$	added mass	$\frac{1}{2}\rho l^5$	-6.715E-04
$K_{q\dot{q}}$	added mass	$\frac{1}{2}\rho l^5$	0.000E+00
$K_{r\dot{r}}$	added mass	$\frac{1}{2}\rho l^5$	-2.547E-06
$K_{uu}$	coupled added mass cross term	$\frac{1}{2}\rho l^3$	0.000E+00
$K_{uv}$	coupled added mass cross term	$\frac{1}{2}\rho l^3$	0.000E+00
$K_{uw}$	coupled added mass cross term	$\frac{1}{2}\rho l^3$	0.000E+00
$K_{up}$	coupled added mass cross term	$\frac{1}{2}\rho l^4$	0.000E+00
$K_{uq}$	coupled added mass cross term	$\frac{1}{2}\rho l^4$	0.000E+00
$K_{ur}$	coupled added mass cross term	$\frac{1}{2}\rho l^4$	0.000E+00
$K_{vv}$	coupled added mass cross term	$\frac{1}{2}\rho l^3$	0.000E+00
$K_{vw}$	coupled added mass cross term	$\frac{1}{2}\rho l^3$	-4.884E-04
$K_{vp}$	coupled added mass cross term	$\frac{1}{2}\rho l^4$	0.000E+00
$K_{vq}$	coupled added mass cross term	$\frac{1}{2}\rho l^4$	-3.852E-03
$K_{vr}$	coupled added mass cross term	$\frac{1}{2}\rho l^4$	0.000E+00
$K_{ww}$	coupled added mass cross term	$\frac{1}{2}\rho l^3$	0.000E+00
$K_{wp}$	coupled added mass cross term	$\frac{1}{2}\rho l^4$	4.145E-04
$K_{wq}$	coupled added mass cross term	$\frac{1}{2}\rho l^4$	0.000E+00
$K_{wr}$	coupled added mass cross term	$\frac{1}{2}\rho l^4$	3.852E-03
$K_{pp}$	coupled added mass cross term	$\frac{1}{2}\rho l^4$	0.000E+00
$K_{pq}$	coupled added mass cross term	$\frac{1}{2}\rho l^4$	-2.547E-06
$K_{pr}$	coupled added mass cross term	$\frac{1}{2}\rho l^4$	0.000E+00
$K_{qq}$	coupled added mass cross term	$\frac{1}{2}\rho l^4$	0.000E+00
$K_{qr}$	coupled added mass cross term	$\frac{1}{2}\rho l^4$	-4.643E-05
$K_{rr}$	coupled added mass cross term	$\frac{1}{2}\rho l^4$	0.000E+00
$K_{u u \delta r}$	fin lift-rolling moment	$u^2 * \delta$	0.000E+00
$K_{u u \delta s}$	fin lift-rolling moment	$u^2 * \delta$	0.000E+00
$K_{u u \delta b}$	fin lift-rolling moment	$u^2 * \delta$	0.000E+00

Table 2.4.1 - Continued

$M_{\dot{u}}$	added mass	$\frac{1}{2}\rho l^4$	0.000E+00
$M_{\dot{v}}$	added mass	$\frac{1}{2}\rho l^4$	0.000E+00
$M_{\dot{w}}$	added mass	$\frac{1}{2}\rho l^4$	-3.932E-03
$M_{\dot{p}}$	added mass	$\frac{1}{2}\rho l^5$	0.000E+00
$M_{\dot{q}}$	added mass	$\frac{1}{2}\rho l^5$	-3.949E-01
$M_{\dot{r}}$	added mass	$\frac{1}{2}\rho l^5$	0.000E+00
$M_{uu}$	coupled added mass cross term	$\frac{1}{2}\rho l^3$	0.000E+00
$M_{uv}$	coupled added mass cross term	$\frac{1}{2}\rho l^3$	0.000E+00
$M_{uw}$	coupled added mass cross term	$\frac{1}{2}\rho l^3$	1.926E-02
$M_{up}$	coupled added mass cross term	$\frac{1}{2}\rho l^4$	0.000E+00
$M_{uq}$	coupled added mass cross term	$\frac{1}{2}\rho l^4$	3.932E-03
$M_{ur}$	coupled added mass cross term	$\frac{1}{2}\rho l^4$	0.000E+00
$M_{vv}$	coupled added mass cross term	$\frac{1}{2}\rho l^3$	0.000E+00
$M_{vw}$	coupled added mass cross term	$\frac{1}{2}\rho l^3$	0.000E+00
$M_{vp}$	coupled added mass cross term	$\frac{1}{2}\rho l^4$	-7.939E-05
$M_{vq}$	coupled added mass cross term	$\frac{1}{2}\rho l^4$	0.000E+00
$M_{vr}$	coupled added mass cross term	$\frac{1}{2}\rho l^4$	-4.145E-04
$M_{ww}$	coupled added mass cross term	$\frac{1}{2}\rho l^3$	0.000E+00
$M_{wp}$	coupled added mass cross term	$\frac{1}{2}\rho l^4$	0.000E+00
$M_{wq}$	coupled added mass cross term	$\frac{1}{2}\rho l^4$	0.000E+00
$M_{wr}$	coupled added mass cross term	$\frac{1}{2}\rho l^4$	0.000E+00
$M_{pp}$	coupled added mass cross term	$\frac{1}{2}\rho l^4$	2.547E-06
$M_{pq}$	coupled added mass cross term	$\frac{1}{2}\rho l^4$	0.000E+00
$M_{pr}$	coupled added mass cross term	$\frac{1}{2}\rho l^4$	3.943E-01
$M_{qq}$	coupled added mass cross term	$\frac{1}{2}\rho l^4$	0.000E+00
$M_{qr}$	coupled added mass cross term	$\frac{1}{2}\rho l^4$	0.000E+00
$M_{rr}$	coupled added mass cross term	$\frac{1}{2}\rho l^4$	-2.547E-06
$M_{u u \delta s} - L$	fin lift-pitch moment	$u^2 * \delta$	-7.616E-05
$M_{u u \delta s} - D$	fin drag-pitch moment	$u^2 * \delta^2$	-6.701E-08
$M_{u u \delta b}$	fin lift-pitch moment	$u^2 * \delta$	2.525E-05
$N_{\dot{u}}$	added mass	$\frac{1}{2}\rho l^4$	0.000E+00
$N_{\dot{v}}$	added mass	$\frac{1}{2}\rho l^4$	7.939E-05
$N_{\dot{w}}$	added mass	$\frac{1}{2}\rho l^4$	0.000E+00
$N_{\dot{p}}$	added mass	$\frac{1}{2}\rho l^5$	-2.547E-06
$N_{\dot{q}}$	added mass	$\frac{1}{2}\rho l^5$	0.000E+00
$N_{\dot{r}}$	added mass	$\frac{1}{2}\rho l^5$	-3.950E-01
$N_{uu}$	coupled added mass cross term	$\frac{1}{2}\rho l^3$	0.000E+00
$N_{uv}$	coupled added mass cross term	$\frac{1}{2}\rho l^3$	-1.877E-02



Table 2.4.1 - Continued

$N_{uw}$	coupled added mass cross term	$\frac{1}{2}\rho l^3$	0.000E+00
$N_{up}$	coupled added mass cross term	$\frac{1}{2}\rho l^4$	-4.145E-04
$N_{uq}$	coupled added mass cross term	$\frac{1}{2}\rho l^4$	0.000E+00
$N_{ur}$	coupled added mass cross term	$\frac{1}{2}\rho l^4$	-7.939E-05
$N_{vv}$	coupled added mass cross term	$\frac{1}{2}\rho l^3$	0.000E+00
$N_{vw}$	coupled added mass cross term	$\frac{1}{2}\rho l^3$	0.000E+00
$N_{vp}$	coupled added mass cross term	$\frac{1}{2}\rho l^4$	0.000E+00
$N_{vq}$	coupled added mass cross term	$\frac{1}{2}\rho l^4$	4.145E-04
$N_{vr}$	coupled added mass cross term	$\frac{1}{2}\rho l^4$	0.000E+00
$N_{ww}$	coupled added mass cross term	$\frac{1}{2}\rho l^3$	0.000E+00
$N_{wp}$	coupled added mass cross term	$\frac{1}{2}\rho l^4$	-3.932E-03
$N_{wq}$	coupled added mass cross term	$\frac{1}{2}\rho l^4$	0.000E+00
$N_{wr}$	coupled added mass cross term	$\frac{1}{2}\rho l^4$	0.000E+00
$N_{pp}$	coupled added mass cross term	$\frac{1}{2}\rho l^4$	0.000E+00
$N_{pq}$	coupled added mass cross term	$\frac{1}{2}\rho l^4$	-3.943E-01
$N_{pr}$	coupled added mass cross term	$\frac{1}{2}\rho l^4$	0.000E+00
$N_{qq}$	coupled added mass cross term	$\frac{1}{2}\rho l^4$	0.000E+00
$N_{qr}$	coupled added mass cross term	$\frac{1}{2}\rho l^4$	2.547E-06
$N_{rr}$	coupled added mass cross term	$\frac{1}{2}\rho l^4$	0.000E+00
$N_{u u _{\partial b}}$	fin lift-yaw moment	$u^2 \delta$	0.000E+00
$N_{u u _{\partial rs}}$	fin lift-yaw moment	$u^2 \delta$	8.794E-05
$U$	design free stream/inflow/surge speed	in/s	8.101E+01
$n_{prop}$	propeller rotation rate at design speed	rpm	1.912E+03
$Z_{max}$	maximum operating depth	in	1.800E+04
$Z_{min}$	minimum operating depth	in	5.625E+00
$rot_{max}$	maximum control fin rotation	deg	2.250E+01

## Key:

- The terms with values in black were determined outright for themselves.
- The terms with values in blue were calculated using terms in black for inputs.
- The terms with values in purple are zero due to the existence of port-starboard symmetry [27].
- The terms with values in teal are always zero regardless of the body configuration [27].
- The terms with values in orange are zero by assumption based on observation of other similar terms and the relative scaling between the size of control fins and the size of the hull.
- The terms with values in grey do not apply to the current configuration of the *Deep 6*.
- The terms with values that have a light blue back fill are represented in degrees (this remains consistent throughout the simulation).

Note: The “units” for the added mass and control fin terms are the quantity that was used for non-dimensionalization.



## CHAPTER THREE

### VEHICLE EQUATIONS OF MOTION AND SIMULATIONS

The numerical simulation of the *Deep 6* incorporated the vehicle parameters that were discussed in Chapter 2 into a system of coupled, non-linear, 6 degrees of freedom equations of motion. These equations approximate the vehicle's behavior under the influence of the control parameters (control fin deflections and propeller rate of revolution). In order to describe the vehicle motions in inertial space, the inertial (Earth fixed) reference frame was orientated such that the positive x-axis pointed to the North, the positive y-axis pointed to the East, and the positive z-axis pointed down. Using the set of 12 first order, non-linear differential equations representing the vehicle motion, numerical simulations were performed based upon the Euler integration method. A numerical linearization was performed to find the linear state-space model about an equilibrium condition.

#### 3.1 Equations of Motion

The simulation of the *Deep 6* began with the writing of an appropriate set of vehicle equations of motion (EOM). The EOM for the underwater vehicles consist of three equations for translation, three equations for rotation, three equations for inertial orientation, and three equations for inertial position. These EOM may differ based upon the mathematical representation or model of the external forces and moments. Fossen presents the most commonly used form of these equations [19]. The generality of these equations is beneficial because it allows for the inclusion of a wide variety of geometric

configurations and external parameters (such as waves, currents, and sea floor/ground effects) [19]. The drawback of using these equations is that their derivation provides little insight into how the inputs are to be determined. Gertler and Hagen present a different form of the EOM. The form presented by Gertler and Hagen are referred to as the standard equations of motion for submarine simulation and were originally developed for use by the United States Navy [23]. The standard submarine equations differ from the ones developed by Fossen in that the equation inputs for the EOM are based upon physically measurable quantities, whereas Fossen's equations are more of a statement of the physics involved with vehicle motion [19], [23]. The key drawback of Gerlter and Hagen's approach is that they are less general. The loss of generality affects the equations' ability to incorporate various environmental forces. If the inclusion of environmental forces (such as wave forcing) were necessary, the required methodology would have to be developed and the equations amended. It shouldn't be too surprising that the standard submarine equations were developed and are ideally suited for vehicle configurations consistent with current naval submarine designs [18], [23]. The *Deep 6* was designed with a long, slender hull, aft mounted propellers, and uses control fins for maneuvering; just like naval submarines. Both sets of equations are coupled and non-linear, and attempt to describe the same set of events; however, the inputs for the standard submarine EOM were more intuitive and easier to obtain approximations for. For this reason, the standard submarine EOM were the basis for the simulation of the *Deep 6*. It is worth noting that the standard submarine equations have been revised over time to incorporate new, more accurate modeling approaches [11], [18]. The most current revision of the EOM was used for the basis of the simulation equations [11].

The *Deep 6*'s motions through its aquatic environment are completely unconstrained; thus, the vehicle is free to translate and rotate about each of the three coordinate axes (3 translations + 3 rotations = 6 total degrees of freedom). Each degree of freedom (DOF) requires its own unique equation. These six equations are based on the ones originally developed by Gertler and Hagen [11], [18], [23]. These EOM are an extension of Newton's Second Law,  $F = ma$  (or  $\tau = I\alpha$  for the 3 rotational cases). The six individual equations were grouped together to form the system of equations shown in Equation 3.1.1a. The "unknown" quantities that are solved for from Equation 3.1.1a are the acceleration terms,  $\{\dot{X}_1\}$ . To obtain the acceleration terms, both sides of Equation 3.1.1a were pre-multiplied by  $[A_1]^{-1}$ . The rearranged form of Equation 3.1.1a that was incorporated into the simulation program to solve for the acceleration terms is shown in Equation 3.1.1b. Equations 3.1.2 – 3.1.7 are the six individual EOM that collectively form Equation 3.1.1a.

---

### Equation 3.1.1a: General Form of 6 Degree of Freedom Equations of Motion

$$[A_1]\{\dot{X}_1\} = [B_1]$$

Where:

$$[A_1] = (\text{mass, inertia, and added mass terms}),$$

$$\{\dot{X}_1\} = [\dot{u}, \dot{v}, \dot{w}, \dot{p}, \dot{q}, \dot{r}]^T,$$

$$\text{and } [B_1] = f(\{X\}, \{U\})$$

$$\{X_1\} = [u, v, w, p, q, r]^T$$

$$\{U\} = [\delta_B, \delta_S, \delta_R, N_{prop}]^T$$

Note: The above equation represents a system of equations taking the form of Newton's Second Law, where the force terms are represented by  $[B_1]$ , the mass terms are represented by  $[A_1]$ , and the acceleration terms are represented by  $\{\dot{X}_1\}$ . A definition of the individual elements of the above vectors and matrices has been provided after Equation 3.1.7.

### Equation 3.1.1b: Rearranged Form of 6 Degree of Freedom Equations of Motion

$$\{\dot{X}_1\} = [A_1]^{-1}[B_1]$$

### Equation 3.1.2: Surge Equation of Motion

$$\begin{aligned} & \left(m - \frac{\rho}{2} L^3 X_{uu}\right) \dot{u} + m z_G \dot{q} - m y_G \dot{r} \\ &= m \left[ v r - w q + x_G (q^2 + r^2) - y_G p q - z_G p r \right] \\ &+ \frac{\rho}{2} L^4 \left[ X_{pp} p^2 + X_{qq} q^2 + X_{rr} r^2 + X_{pr} p r \right] \\ &+ \frac{\rho}{2} L^3 \left[ X_{wq} w q + X_{vp} v p + X_{vr} v r \right] \\ &+ u q (X_{uq\delta_b} \delta_b + X_{uq\delta_s} \delta_s) + u r (X_{ur\delta_r} \delta_r) \\ &+ \frac{\rho}{2} L^2 \left[ X_{vv} v^2 + X_{ww} w^2 \right] \\ &+ u v (X_{uv\delta_r} \delta_r) + u w (X_{uw\delta_b} \delta_b + X_{uw\delta_s} \delta_s) \\ &+ u |u| \left( X_{uu\delta_b} \delta_b^2 + X_{uu\delta_s} \delta_s^2 + X_{uu\delta_r} \delta_r^2 \right) \\ &- (W - B) \sin(\theta) \\ &+ \frac{\rho}{2} L^2 C_{d_x} \left[ C_{vn}^2 N_{prop} |N_{prop}| - u |u| \right] \end{aligned}$$

### Equation 3.1.3: Sway Equation of Motion

$$\begin{aligned}
& \left(m - \frac{\rho}{2} L^3 Y_{\dot{v}}\right) \dot{v} + \left(-m z_G - \frac{\rho}{2} L^4 Y_{\dot{p}}\right) \dot{p} - \left(m x_G - \frac{\rho}{2} L^4 Y_{\dot{r}}\right) \dot{r} \\
& = m \left[ -ur + wp - x_G pq + y_G (p^2 + r^2) - z_G qr \right] \\
& + \frac{\rho}{2} L^4 \left[ Y_{pq} pq + Y_{qr} qr \right] \\
& + \frac{\rho}{2} L^3 \left[ Y_{up} up + Y_{ur} ur + Y_{vq} vq + Y_{wp} wp + Y_{wr} wr \right] \\
& + \frac{\rho}{2} L^2 \left[ Y_{uv} uv + Y_{vw} vw \right] \\
& + u \left| u \right| \left( Y_{uu\delta_r} \delta_r^2 \right) \\
& - \frac{\rho}{2} \int_{x_{tail}}^{x_{nose}} \left[ C_{d_y} h(x) (v + xr)^2 + C_{d_z} b(x) (w - xq)^2 \right] \frac{(v + xr)}{U_{ef}(x)} dx \\
& + (W - B) \cos(\theta) \sin(\phi)
\end{aligned}$$

### Equation 3.1.4: Heave Equation of Motion

$$\begin{aligned}
& \left(m - \frac{\rho}{2} L^3 Z_{\dot{w}}\right) \dot{w} + m y_G \dot{p} + \left(-m x_G - \frac{\rho}{2} L^4 Z_{\dot{q}}\right) \dot{q} \\
& = m \left[ uq - vp - x_G pr - y_G qr + z_G (p^2 + q^2) \right] \\
& + \frac{\rho}{2} L^4 \left[ Z_{pp} p^2 + Z_{pr} pr + Z_{rr} r^2 \right] \\
& + \frac{\rho}{2} L^3 \left[ Z_{uq} uq + Z_{vp} vp + Z_{vr} vr \right] \\
& + \frac{\rho}{2} L^2 \left[ Z_{uw} uw + Z_{vv} v^2 \right] \\
& + u \left| u \right| \left( Z_{uu\delta_b} \delta_b^2 + Z_{uu\delta_s} \delta_s^2 \right) \\
& - \frac{\rho}{2} \int_{x_{tail}}^{x_{nose}} \left[ C_{d_y} h(x) (v + xr)^2 + C_{d_z} b(x) (w - xq)^2 \right] \frac{(w + xq)}{U_{ef}(x)} dx \\
& + (W - B) \cos(\theta) \sin(\phi)
\end{aligned}$$

### Equation 3.1.5: Roll Equation of Motion

$$\begin{aligned}
& \left( m z_G - \frac{\rho}{2} L^4 K_{\dot{v}} \right) \dot{v} + m y_G \dot{w} + \left( I_x - \frac{\rho}{2} L^5 K_{\dot{p}} \right) \dot{p} - I_{xy} \dot{q} + \left( -I_{xz} - \frac{\rho}{2} L^5 K_{\dot{r}} \right) \dot{r} \\
& = \left[ -\left( I_z - I_y \right) q r - I_{xy} p r + I_{yz} \left( q^2 - r^2 \right) + I_{xz} p q \right] \\
& - m \left[ y_G \left( -u q + v p \right) - z_G \left( u r - w p \right) \right] \\
& + \frac{\rho}{2} L^5 \left[ K_{pq} p q + K_{qr} q r + K_{pp} p |p| \right] \\
& + \frac{\rho}{2} L^4 \left[ K_{up} |u| p + K_{ur} u r + K_{vq} v q + K_{wp} w p + K_{wr} w r \right] \\
& + \frac{\rho}{2} L^3 \left[ K_{uv} u v + K_{vw} v w \right] \\
& - u |u| \left( K_{uu\delta_b} \delta_b + K_{uu\delta_s} \delta_s \right) \\
& + \left( y_G W - y_B B \right) \cos(\theta) \cos(\phi) \\
& - \left( z_G W - z_B B \right) \cos(\theta) \sin(\phi)
\end{aligned}$$

### Equation 3.1.6: Pitch Equation of Motion

$$\begin{aligned}
& m z_G \dot{u} + \left( -m x_G - \frac{\rho}{2} L^4 M_{\dot{w}} \right) \dot{w} - I_{xy} \dot{p} + \left( I_y - \frac{\rho}{2} L^5 M_{\dot{q}} \right) \dot{q} - I_{yz} \dot{r} \\
& = \left[ -\left( I_x - I_z \right) p r + I_{xy} q r - I_{yz} p q - I_{xz} \left( p^2 + r^2 \right) \right] \\
& + m \left[ x_G \left( -u q + v p \right) - z_G \left( -v r + w q \right) \right] \\
& + \frac{\rho}{2} L^5 \left[ M_{pp} p^2 + M_{pr} p r + M_{rr} r |r| + M_{qq} q |q| \right] \\
& + \frac{\rho}{2} L^4 \left[ M_{uq} u q + M_{vp} v p + M_{vr} v r \right] \\
& + \frac{\rho}{2} L^3 \left[ M_{uw} u w + M_{vv} v^2 \right] \\
& + u |u| \left( M_{uu\delta_b} \delta_b + M_{uu\delta_{sL}} \delta_s + M_{uu\delta_{sD}} \delta_s^2 \right) \\
& - \frac{\rho}{2} \int_{x_{tail}}^{x_{nose}} \left[ C_{d_y} h(x) (v + x r)^2 + C_{d_z} b(x) (w - x q)^2 \right] \frac{(w + x q)}{U_{eff}(x)} x dx \\
& - \left( x_G W - x_B B \right) \cos(\theta) \cos(\phi) \\
& - \left( z_G W - z_B B \right) \sin(\theta)
\end{aligned}$$

### Equation 3.1.7: Yaw Equation of Motion

$$\begin{aligned}
m y_G \dot{u} + \left( m x_G - \frac{\rho}{2} L^4 N_{\dot{y}} \right) \dot{y} + \left( -I_{xz} - \frac{\rho}{2} L^5 N_{\dot{p}} \right) \dot{p} - I_{yz} \dot{q} + \left( I_z - \frac{\rho}{2} L^5 N_{\dot{r}} \right) \dot{r} \\
= \left[ -\left( I_y - I_x \right) p q - I_{xy} \left( p^2 - q^2 \right) + I_{yz} p r - I_{xz} q r \right] \\
- m \left[ x_G (u r - w p) - y_G (-v r + w q) \right] \\
+ \frac{\rho}{2} L^5 \left[ N_{pq} p q + N_{qr} q r + N_{rr} r |r| \right] \\
+ \frac{\rho}{2} L^4 \left[ N_{up} u p + N_{ur} u r + N_{vq} v q + N_{wp} w p + N_{wr} w r \right] \\
+ \frac{\rho}{2} L^3 \left[ N_{uv} u v + N_{vw} v w \right] \\
- u |u| \left( N_{uu} \delta_r \right) \\
- \frac{\rho}{2} \int_{x_{tail}}^{x_{nose}} \left[ C_{d_y} h(x) (v + x r)^2 + C_{d_z} b(x) (w - x q)^2 \right] \frac{(v + x r)}{U_{cf}(x)} x dx \\
+ (x_G W - x_B B) \cos(\theta) \sin(\phi) \\
+ (y_G W - y_B B) \sin(\theta)
\end{aligned}$$

Where:

$U_{cf}(x) = \sqrt{(v + x r)^2 + (w - x q)^2}$  is the cross body flow,

$C_{vn} = \frac{U_o}{N_{prop}^*}$  is the propeller control parameter,

$u$  is the longitudinal velocity in the body fixed coordinate system,

$v$  is the transverse velocity in the body fixed coordinate system,

$w$  is the vertical velocity in the body fixed coordinate system,

$p$  is the roll rate in the body fixed coordinate system,

$q$  is the pitch rate in the body fixed coordinate system,

$r$  is the yaw rate in the body fixed coordinate system,

$x$  is the x-axis displacement in the Earth fixed coordinate system,

$y$  is the y-axis displacement in the Earth fixed coordinate system,

$z$  is the z-axis displacement in the Earth fixed coordinate system,

$x_G$  is the longitudinal location of the vehicle's center of gravity in the body fixed coordinate system (measured from the vehicle's nose),

$y_G$  is the transverse location of the vehicle's center of gravity in the body fixed coordinate system (measured from the vehicle's centerline/axis of revolution),

$z_G$  is the vertical location of the vehicle's center of gravity in the body fixed coordinate system (measured from the vehicle's centerline/axis of revolution),

$x_B$  is the longitudinal location of the vehicle's center of buoyancy in the body fixed coordinate system (measured from the vehicle's nose),

$y_B$  is the transverse location of the vehicle's center of buoyancy in the body fixed coordinate system (measured from the vehicle's centerline/axis of revolution),

$z_B$  is the vertical location of the vehicle's center of buoyancy in the body fixed coordinate system (measured from the vehicle's centerline/axis of revolution),

$\Phi$  is the Euler roll angle in the Earth fixed coordinate system,

$\Theta$  is the Euler pitch angle in the Earth fixed coordinate system,

$\Psi$  is the Euler yaw angle in the Earth fixed coordinate system,

### Equation 3.1.7 - Continued

$b(x)$  is the total height of the vehicle (hull diameter for bodies of revolution) along the vehicle's centerline at a specific longitudinal position,  $x$ ,

$h(x)$  is the total width of the vehicle (hull diameter for bodies of revolution) along the vehicle's centerline at a specific longitudinal position,  $x$ .

$L$  is the vehicle's length (LOA),

$\rho$  is the mass density of the fluid medium,

$m$  is the mass of the vehicle,

$W$  is the weight of the vehicle ( $m$  times the acceleration due to gravity),

$B$  is the buoyant force that results from the vehicle displacing fluid,

$I_*$  is the mass moment of inertia for the vehicle about the axis  $*$ ,

$I_{*#}$  is the product of inertia for axes  $*$  and  $\#$ ,

$Cd_*$  is the drag coefficient for the vehicle for flow along the  $*$  axis,

$N_{prop*}$  is the rate of revolution for the propeller (in rpm),

$N_{prop}$  is the rate of revolution for the propeller at the design speed (in rpm),

$U_o$  is the vehicle's design speed,

and "dotted" terms are the time derivative of the "undotted" quantity,

Note: Under most circumstances,

$$\dot{\phi} \neq p$$

$$\dot{\theta} \neq q$$

$$\dot{\psi} \neq r$$

The six differential equations shown in Equations 3.1.2 – 3.1.7 mathematically describe the interactions between the forces acting upon the vehicle and its motions. These equations take into consideration the vehicle's mass, its rotational inertia, and the added mass and hydrodynamic damping (all about their appropriate axes). The right hand sides of the six equations represent the mass and acceleration (or mass moment of inertia and rotational acceleration for the 3 rotational cases) terms in Newton's Second Law. The left hand side of these equations represent the forcing (or torque) term of Newton's Second Law. The left hand side of the equations is primarily composed of added mass terms. The inclusion of the added mass terms is the most significant difference between the EOM used for submarine and aircraft simulations [41]. Since water is approximately 800 times denser than air, the submarine EOM must include the added mass terms to



provide reasonable predictions [11], [24]. The added mass arises from the viscous drag entraining fluid, which exerts a resistive force upon the vehicle when attempting to accelerate during a maneuver [34]. Other force terms that are represented on the left hand sides of the equations are drag forces, propulsion forces, and control fin forces and moments. All of the equations except the pitch moment equation (Equation 3.1.6) have only one force or moment associated with each fin deflection. This condition exists as a result of the upper aft fin and the bow planes having been located along the vehicle's axis of revolution. The pitch equation has an additional control fin moment term to account for the longitudinal and the vertical offset of the two lower aft fins. Similar to the aircraft EOM, the submarine EOM expression for the physics contained within the equations is greatly simplified through the use of "stability and control derivatives" [41]. The derivative quantities are all of the  $X_{\#}$ ,  $Y_{\#}$ ,  $Z_{\#}$ ,  $P_{\#}$ ,  $Q_{\#}$ , and  $R_{\#}$  terms, where  $\#$  is representative of any number of possible variables. These derivative quantities represent the non-dimensional force/moment along/about the appropriate axis due to the subscripted variable. For example,  $X_{\dot{u}}$  is the non-dimensional force in the x-direction that results from an acceleration in the x-direction ( $\dot{u}$ ). The derivatives are all dimensionalized by the product of one-half of the mass density and the vehicle length raised to differing powers ( $\frac{1}{2} \rho L^n$ ). The formulas that were used to determine these derivative quantities assume that their values remain constant. It is conceivable that the derivatives, or even other parameters such as mass and volume, could change during operation. However, for simplicity it was assumed that during the simulation all input quantities would remain constant. Under this calculation regime a change of a "constant"

parameter would require two separate calculations (or an alteration to the program code). The only parameters that do change during the calculation of Equations 3.1.2 – 3.1.7 are the values of the elements of  $\{\dot{X}_1\}$  and  $\{X_2\}$ . This characteristic allows the matrix  $[A_1]$  of Equation 3.1.1 to be calculated only once for the entire analysis interval. The matrix  $[B_1]$ , though, must be reevaluated each iteration since it is a function of  $\{X_2\}$ .

Each iteration of the simulation program determines the six acceleration quantities from Equations 3.1.2 – 3.1.7, in addition to six inertial frame velocities. Equation 3.1.8 displays the equations incorporated into the simulation program to determine the second set of 6 unknown quantities, the inertial frame velocities. Equation 3.1.8 transforms the known velocities from the body fixed coordinate system to the Earth fixed coordinate system. The sub-matrix  $[R_1]$  is responsible for transforming the linear velocities, while the sub-matrix  $[R_2]$  transforms the rotational velocities. Since the orientation angles of the vehicle (the last three elements of  $\{X_2\}$ ) could change with each iteration, the transformation matrix,  $[T]$ , is updated every iteration.

---

**Equation 3.1.8: Body to Inertial Frame Velocity Transformation**

$$\{\dot{X}_2\} = [T]\{X_2\}$$

Where:

$$\{\dot{X}_2\} = [\dot{x}, \dot{y}, \dot{z}, \dot{\phi}, \dot{\theta}, \dot{\psi}]^T$$

$$\{X_2\} = [x, y, z, \phi, \theta, \psi]^T$$

$$[T] = \begin{bmatrix} [R_1] & [0] \\ [0] & [R_2] \end{bmatrix}$$

$$[R_1] = \begin{pmatrix} \cos(\theta) \cdot \cos(\psi) & \cos(\theta) \cdot \sin(\psi) & -\sin(\theta) \\ \sin(\phi) \cdot \sin(\theta) \cdot \cos(\psi) - \cos(\phi) \cdot \sin(\psi) & \sin(\phi) \cdot \sin(\theta) \cdot \sin(\psi) + \cos(\phi) \cdot \cos(\psi) & \sin(\phi) \cdot \cos(\theta) \\ \cos(\phi) \cdot \sin(\theta) \cdot \cos(\psi) + \sin(\phi) \cdot \sin(\psi) & \cos(\phi) \cdot \sin(\theta) \cdot \sin(\psi) - \sin(\phi) \cdot \cos(\psi) & \cos(\phi) \cdot \cos(\theta) \end{pmatrix}$$

$$[R_2] = \begin{pmatrix} 1 & 0 & -\sin(\theta) \\ 0 & \cos(\phi) & \sin(\phi) \cdot \cos(\theta) \\ 0 & -\sin(\phi) & \cos(\phi) \cdot \cos(\theta) \end{pmatrix}$$

---

To start the solution process, the simulation program must be provided with the initial conditions, which represent the combination of the  $\{X_1\}$  and  $\{X_2\}$  vectors at the starting time of the analysis. These initial conditions are used to determine the value of the  $\{\dot{X}_1\}$  and  $\{\dot{X}_2\}$  vectors. Once  $\{\dot{X}\}$  (which represents the combination of  $\{\dot{X}_1\}$  and  $\{\dot{X}_2\}$ ) has been determined, the initial set of known values,  $\{X\}$  are updated in time through integration. Equations 3.1.9 and 3.1.10 define the complete  $\{\dot{X}\}$  and  $\{X\}$ , respectively. An Euler integration routine has been incorporated into the simulation program to perform this operation. The Euler integration routine was selected in order to remain consistent with other AUV simulation programs [11], [19]. The Euler integration routine may lead to numerical instabilities over long time intervals, but does offer the unique

ability of providing “real time” solutions if used in conjunction with carefully designed numerical filters.

---

**Equation 3.1.9: Definition of  $\dot{X}$  Vector**

$$\{\dot{X}\} = [\dot{u}, \dot{v}, \dot{w}, \dot{p}, \dot{q}, \dot{r}, \dot{x}, \dot{y}, \dot{z}, \dot{\phi}, \dot{\theta}, \dot{\psi}]^T$$

**Equation 3.1.10: Definition of  $X$  Vector**

$$\{X\} = [u, v, w, p, q, r, x, y, z, \phi, \theta, \psi]^T$$

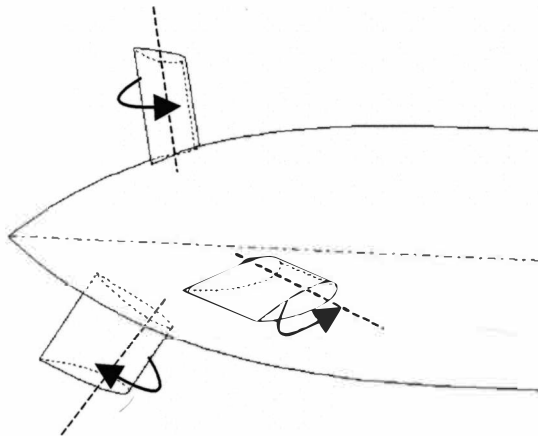
---

Equations 3.1.2 – 3.1.7 represent the EOM in simplified form. The simplifications that were performed were those allowed by the configuration of the *Deep 6*. A review of the original EOM revealed that equations could be simplified if the effects of the control fin rotations were properly grouped. The ability to produce a rolling moment was not a desirable capability for the control fins, thus the ability for the two forward fins to rotate in opposite directions would not be required. Since the foreword fins would always move as a coordinated pair, the additional forces and moments produced by their deflection could be grouped. For the remainder of the project the pair of forward fins would be collectively referred to as the bow planes. Similarly, to avoid producing a rolling moment when turning, it was deduced, via a free body diagram, that all three aft fins would need to be deflected. The free body diagram for the rotation of the aft fins revealed that the lower two fins were required to rotate the same amount as the upper fin to produce a yaw moment without producing a pitching moment. To achieve this condition, the two lower aft fins are required to rotate in opposite directions from one another. Figure 3.1.1 provides an example of the required aft fin rotations necessary to

produce a positive yaw angle. The effects of all three aft fins rotating in this manner were grouped and hence forth referred to as the rudder deflection. The same free body diagram also revealed that by rotating the two lower fins together, in a similar fashion to the bow planes, a pitching moment would be produced with no net yawing moment. The stern planes became the combined action of the two lower aft planes. Both the bow planes and the stern planes are individually capable of producing pitching moments, but used together they are capable of producing a net vertical force with no net pitching moment. The combined action of the bow and the stern planes allows for the desirable level posture altitude climbing described in Section 2.2. The grouping action of the individual fin components allowed the equations to consider the effects of a deflection for the three groups of fins instead of all of the fins individually.

---

**Figure 3.1.1: Aft Fin Configuration for Rudder Deflection**



---

As mentioned in Chapter 2, the selected EOM required no additional calculations to determine the control effect that the propellers' rate of revolution exerts upon the vehicle's performance. The reason for this is that the propeller control parameter can be

determined as a simple ratio of the design speed for the vessel and the required rpm necessary to achieve this speed [11]. Since both the design speed (4.0 kts.) and the propeller rate of revolution (1,912 rpm) required for the design speed were already known, the control parameter  $C_{vn}$  could be easily calculated within the simulation program. The EOM model the propellers' ability to generate thrust at various rates of revolution based upon the Propeller Law, which states that thrust is proportional to the square of the rate of revolution [25]. A noteworthy caveat of the expression for the propulsion thrust generated used by the equations of motion is that the effective thrust decreases with the square of the vehicle speed (due to an increase in resistance, which increases with the square of the speed). This result is in agreement with both naval architecture propeller-engine matching and idealized pump characteristics [11], [25]. The benefit of using this idealized model is that the propulsive thrust is simple to calculate during the simulation and a very limited amount of data is required to be known prior to the simulation.

### **3.2 Simulation**

Once a suitable set of equations of motion had been selected and all of the necessary inputs acquired, the simulation program, Underwater Vehicle Simulator, was created. The new simulation program was created because it was simpler to write a new program specific for this study than it was to modify a publicly available one. The simulation that Underwater Vehicle Simulator performs is a direct numerical solution of the coupled, non-linear, 6 DOF vehicle EOM. This program consists of one main function (UWV\_Sim.m) and 15 sub-routines that are called by the main function to perform the

various tasks associated with the simulation. Underwater Vehicle Simulator was made modular so that it can easily accommodate different operational procedures (such as a different set of EOM or integration routines). Some of the most important sub-routines of the program are the vehicle data gathering routines. These routines import the design characteristics of the vehicle under investigation directly from the Excel Workbook that was used for the preliminary design and saves them to a MATLAB data file (.mat format) for future use. The linking of these two programs not only eliminates the potential for errors during data entry, but also allows for the effects of design changes to be discovered almost as soon as they are made. Another benefit of the Excel import routines is that it relieves the user from having to enter all of the vehicle characteristic data, which is in excess of 200 different values (in addition to the geometry data). Another feature of Underwater Vehicle Simulator is that after performing the non-linear simulation it provides the user with the option of linearizing the EOM. Figure 3.2.1 displays a simplified flow diagram for the operation of Underwater Vehicle Simulator.

**Figure 3.2.1: Simulation Program Flowchart**

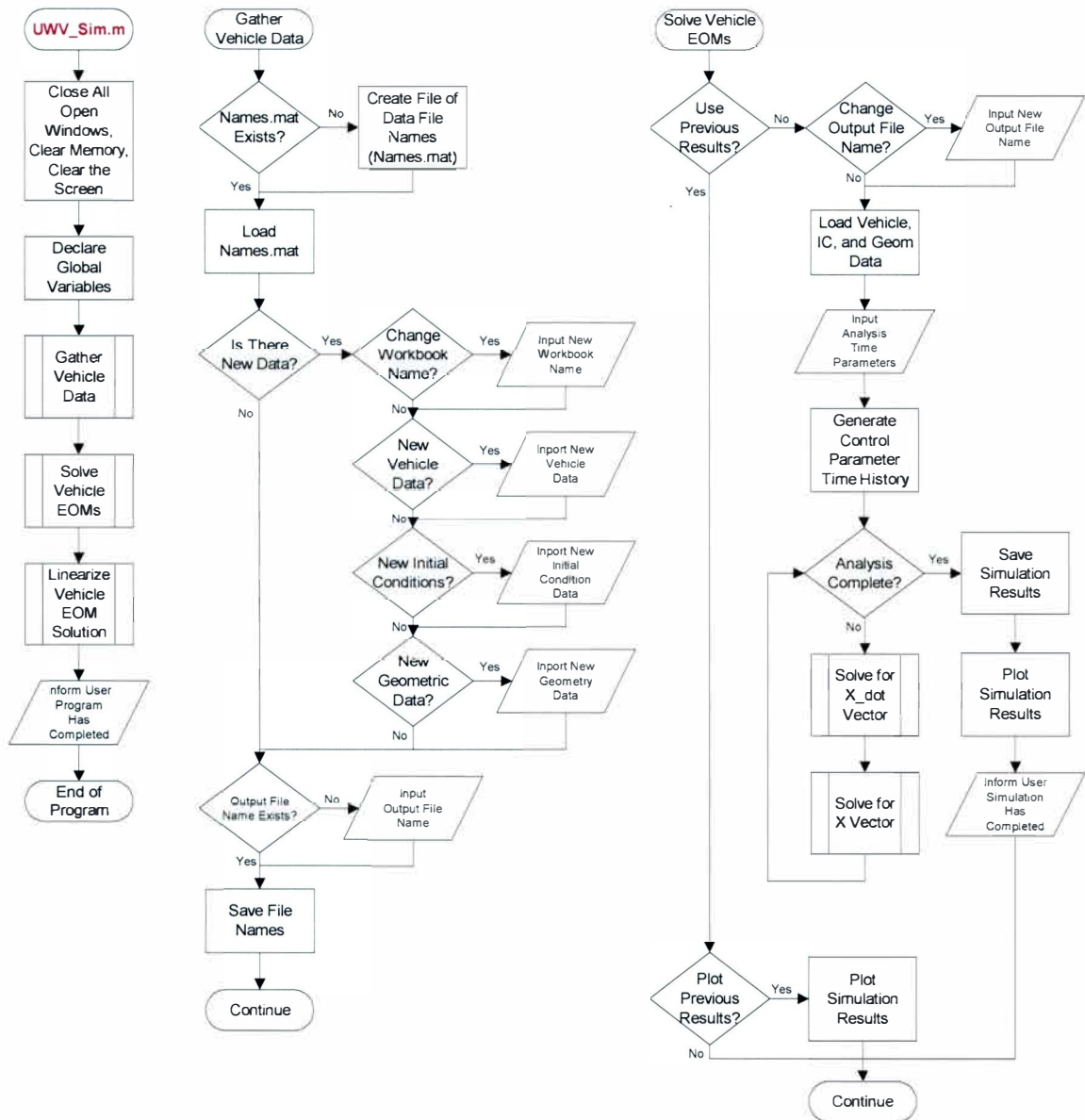
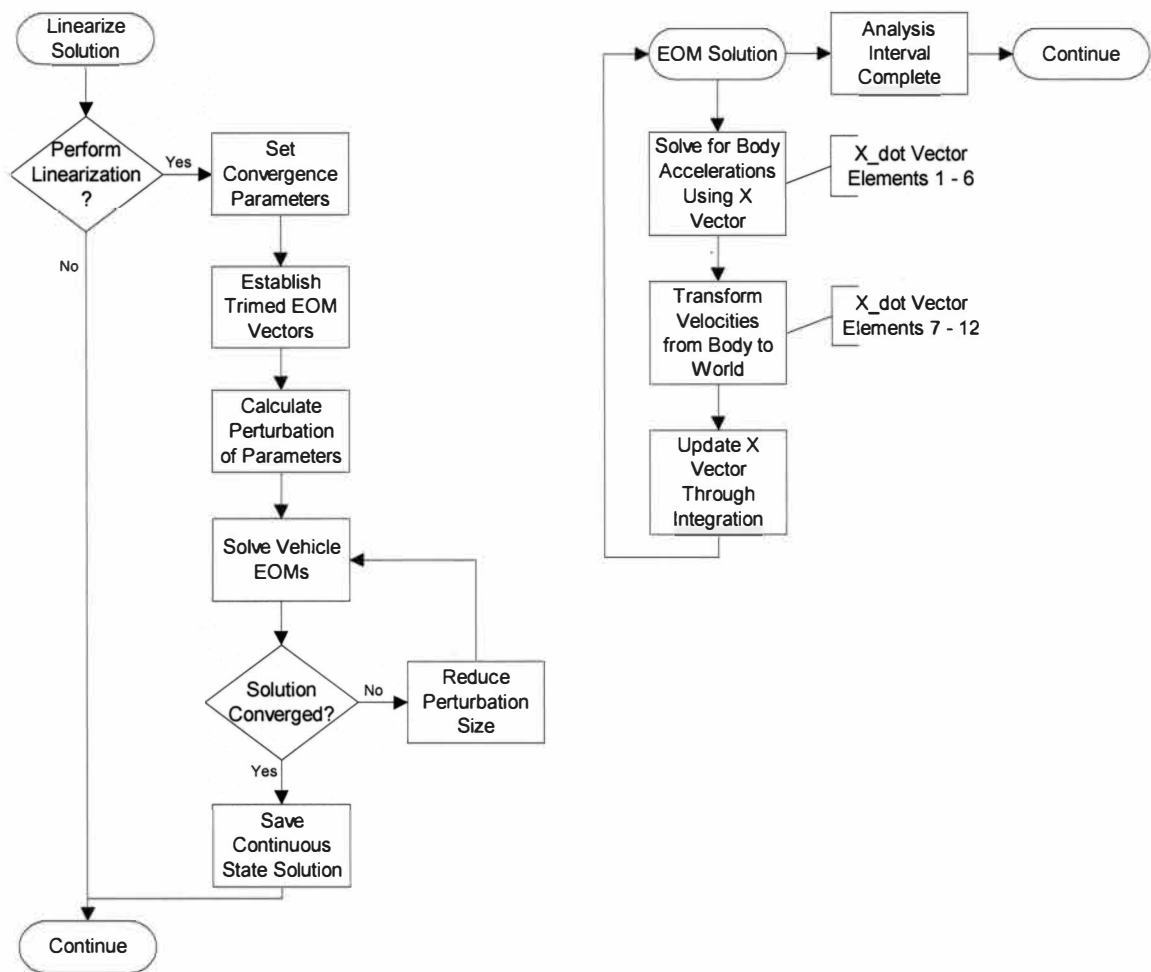




Figure 3.2.1 - Continued



The non-linear system of equations that were chosen to simulate the *Deep 6* describes the vehicle posture in space using three Euler angles, utilizing a 3-2-1 rotation sequence. There are 12 possible Euler angle rotation sequences. The 3-2-1 sequence was selected for the use in Underwater Vehicle Simulator to remain consistent with accepted aerospace and naval architecture practice [9], [11], [34]. Euler angles are a rational and systematic method of precisely describing a body's orientation in space, which could potentially be described through an almost infinite combination of different angles [9],

[39]. The use of Euler angles does require some restrictions on the orientations possible, though. The second of the rotations in the 3-2-1 sequence (rotation about the  $y'$  axis) produces a singularity when its angle,  $\theta$ , is equal to  $\pm \pi/2$ . Techniques have been developed to avoid the singularity problem of the Euler angles, such as Euler parameters (a.k.a. quaternions) [9], [11]. Use of the Euler parameters requires the calculation of one additional differential equation each iteration to perform the conversion between parameters and angles. The final solution is converted back into Euler angles because the angle values are much easier to interpret [9]. The use of Euler parameters was not incorporated into the calculation routine of Underwater Vehicle Simulator due to the fact that “most underwater vehicles must be prevented from inverting horizontally or pointing vertically, in order to prevent internal vehicle damage and uncontrollable maneuvering instabilities” [11]. Therefore, to simplify the simulation code Euler angles were used throughout. To address the singularity issue, a check routine was created within the program that will stop the simulation when the vehicle approaches horizontal inversion or “up-ending”. If the vehicle does attempt a maneuver that creates an undesirable orientation angle an error message will be output prior to the termination of the simulation.

During the calculation of the simulation solution, Underwater Vehicle Simulator saves the  $\{\dot{X}\}$  and  $\{X\}$  from each iteration. Once the required number of iterations had been performed the program generated plots of the stored acceleration, velocity, and position data. Also plotted is the “time history” for the four control parameters (three control fin rotations and the propeller rate of revolution) and a 3D plot of the vehicle’s displacement

with respect to the inertial (Earth fixed) reference frame. Figures 3.2.2 – 3.2.7 display example results generated by Underwater Vehicle Simulator. The simulations displayed in Figures 3.2.2 – 3.2.7 all use an integration time step of 0.01 sec. The initial depth for the vehicle was set at 3,600 in. (300 ft.) for all of the analyses. The value of 3,600 in. was selected to provide the vehicle with sufficient room to maneuver vertically without exceeding the low and high value limits (the water's surface and the maximum depth of the Great Lakes, respectively). For the simulations that involved control fin deflections, the respective control fin rotation rate was set at  $1^{\circ}/s$ , which more accurately simulated reality than did a step change. The actual rate of fin rotation can easily be incorporated into the simulation program once the capabilities of the control fin servomotors are known.

### Figures 3.2.2: Simulation Results – Case 1, Steady State Condition

Figure 3.2.2a

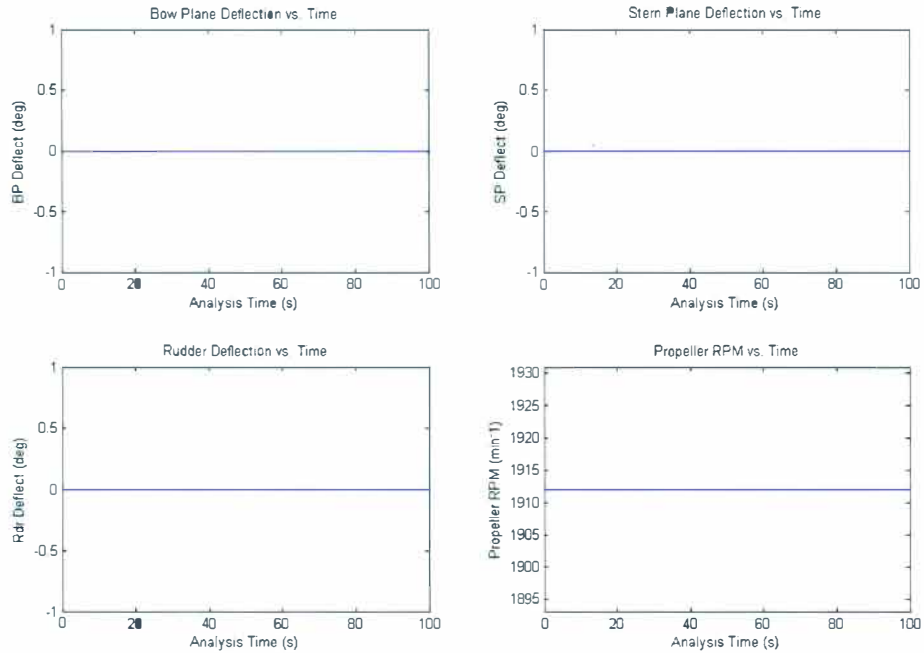


Figure 3.2.2b

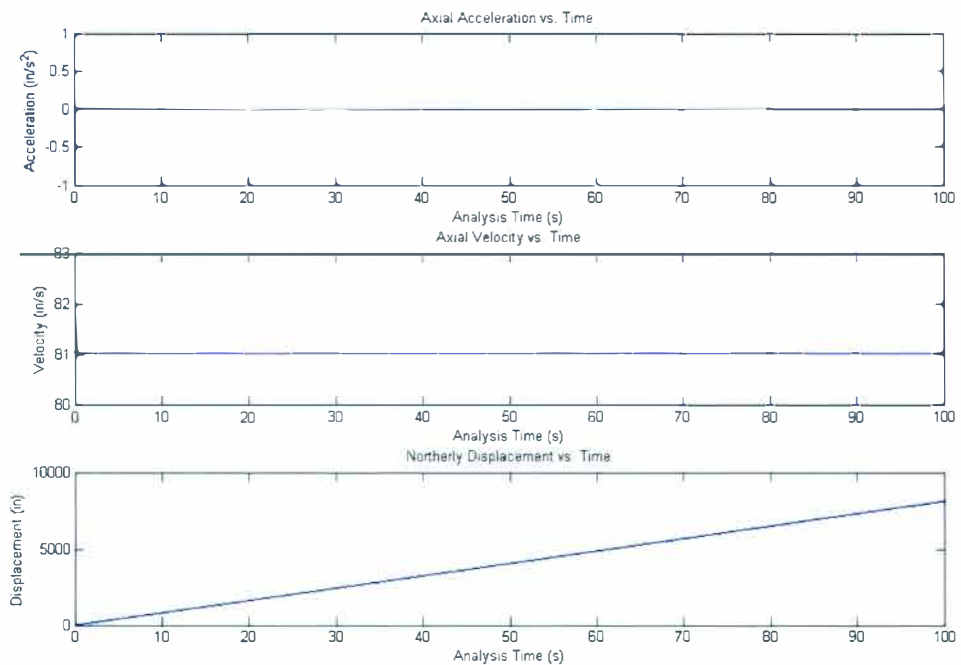


Figure 3.2.2c

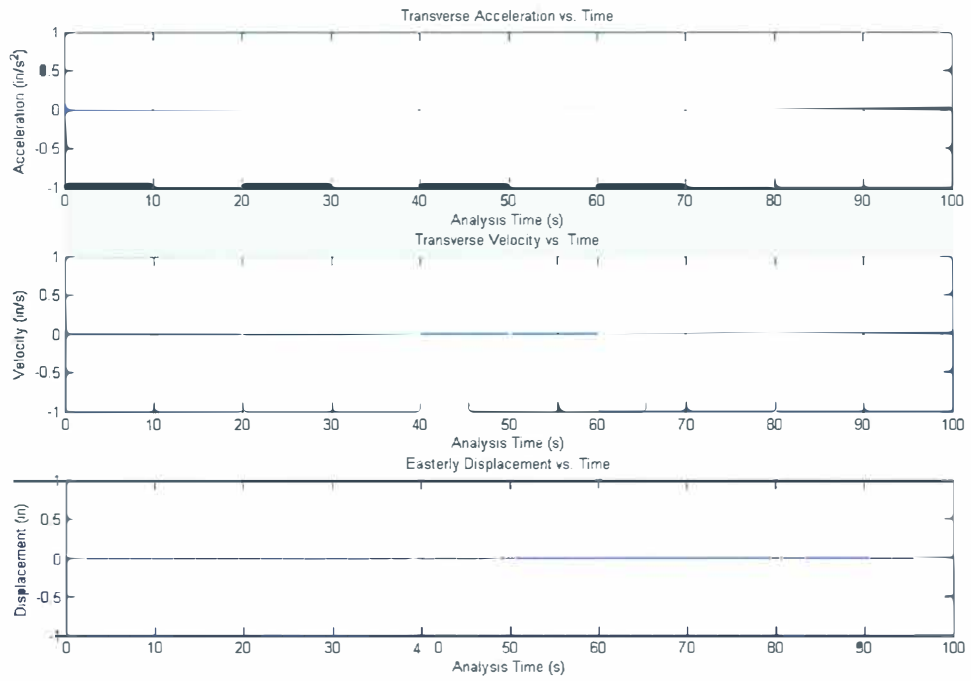


Figure 3.2.2d

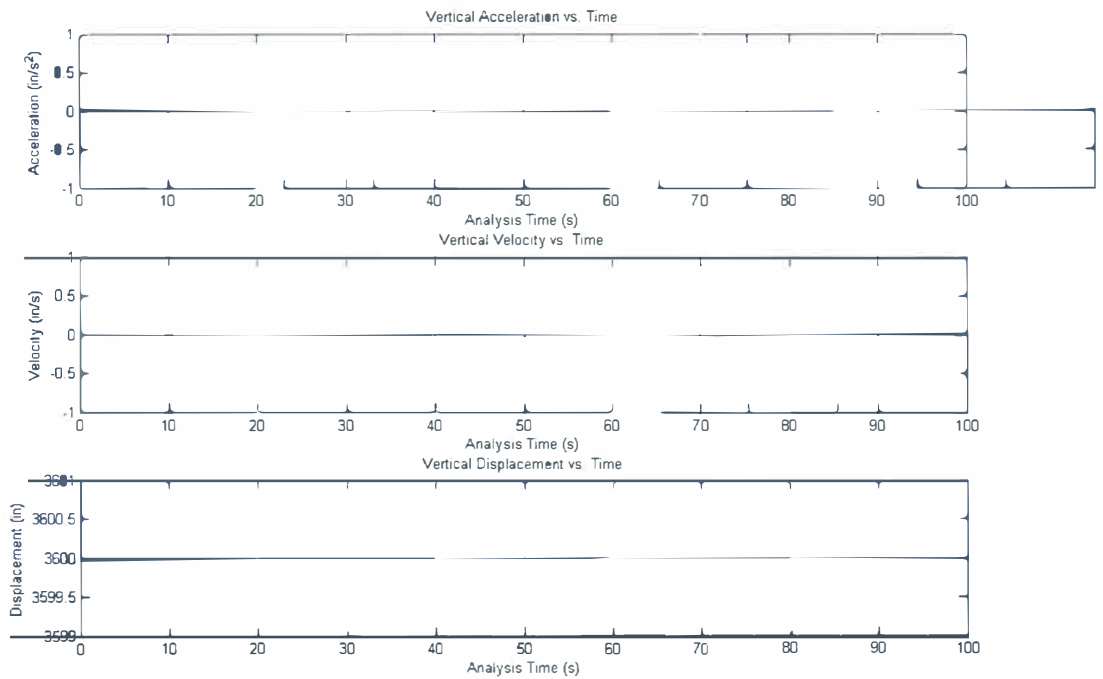


Figure 3.2.2e

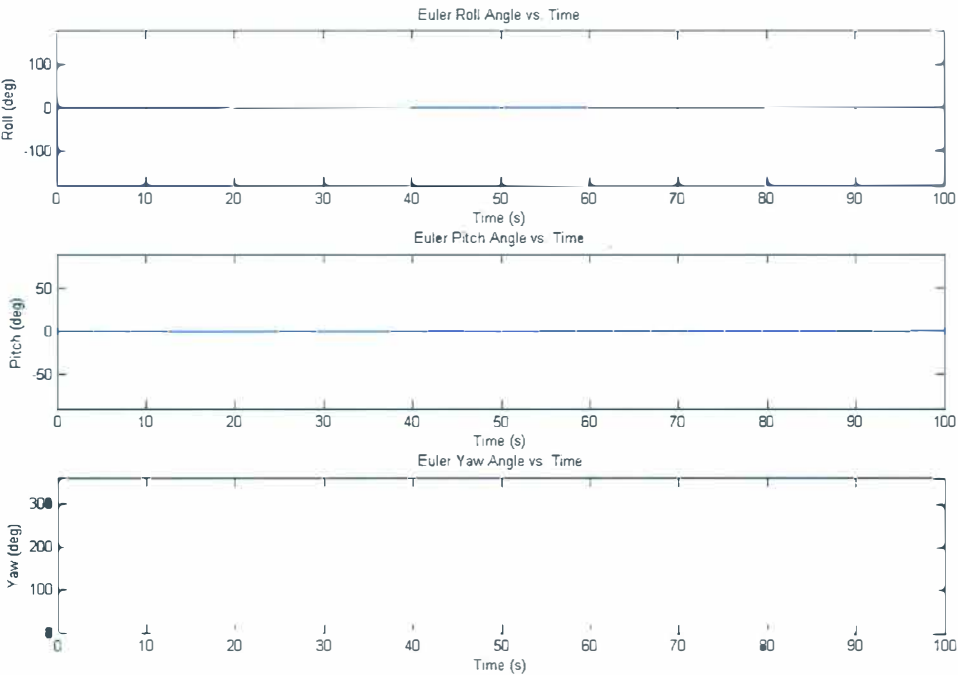
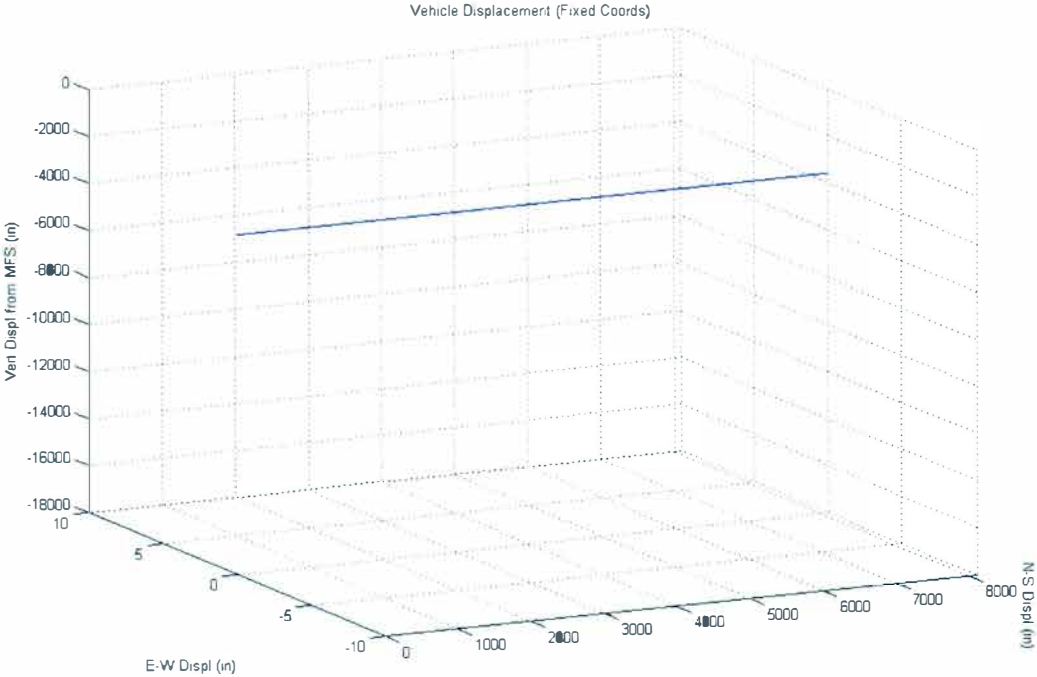


Figure 3.2.2f



**Figures 3.2.3: Simulation Results – Case 2, No Initial Velocity**

Figure 3.2.3a

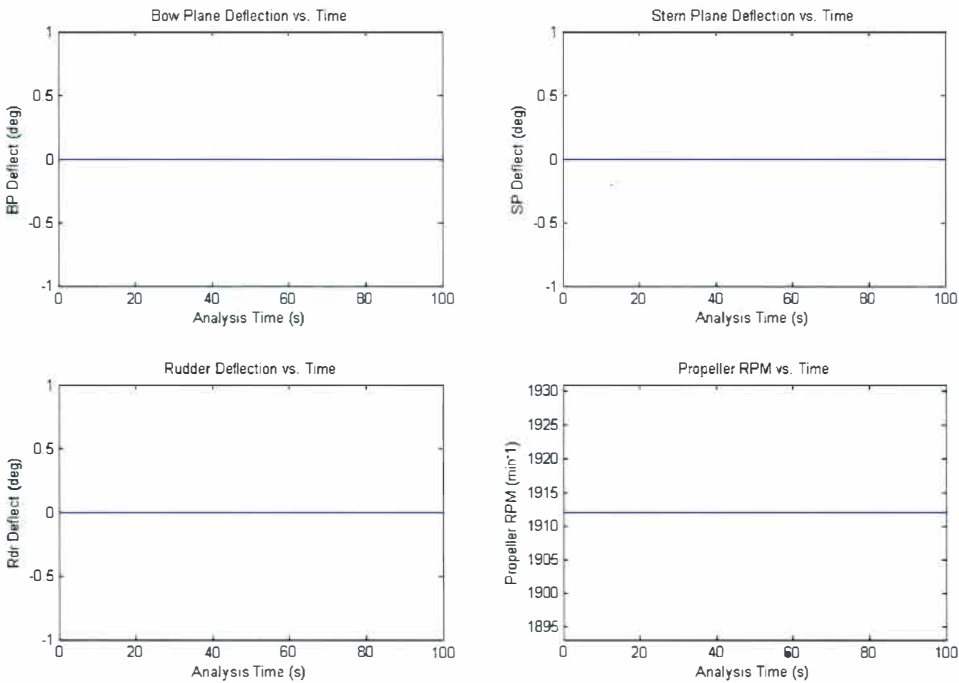


Figure 3.2.3b

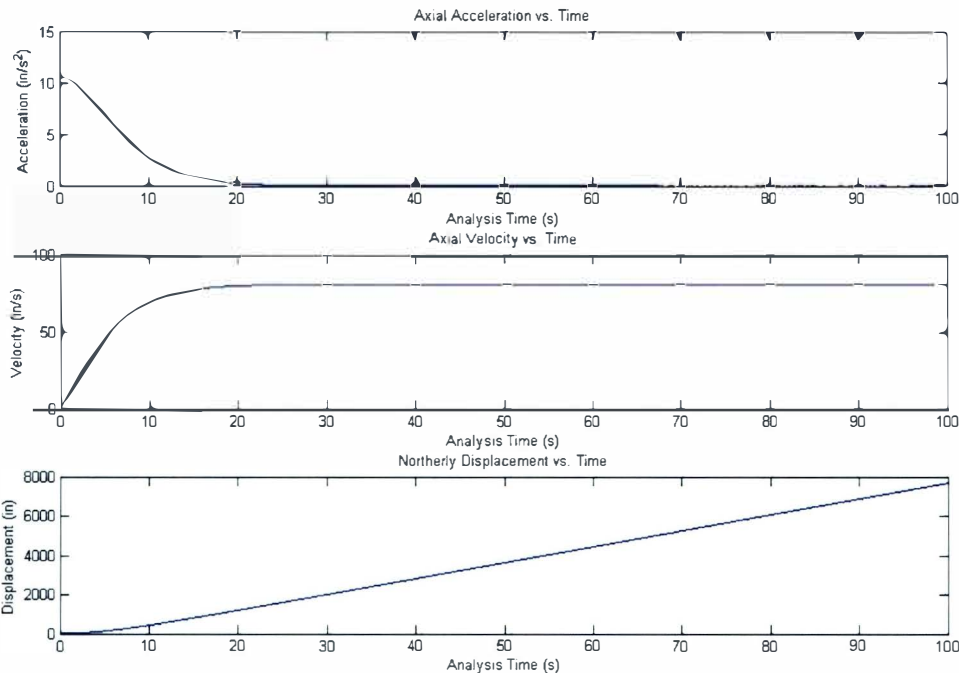


Figure 3.2.3c

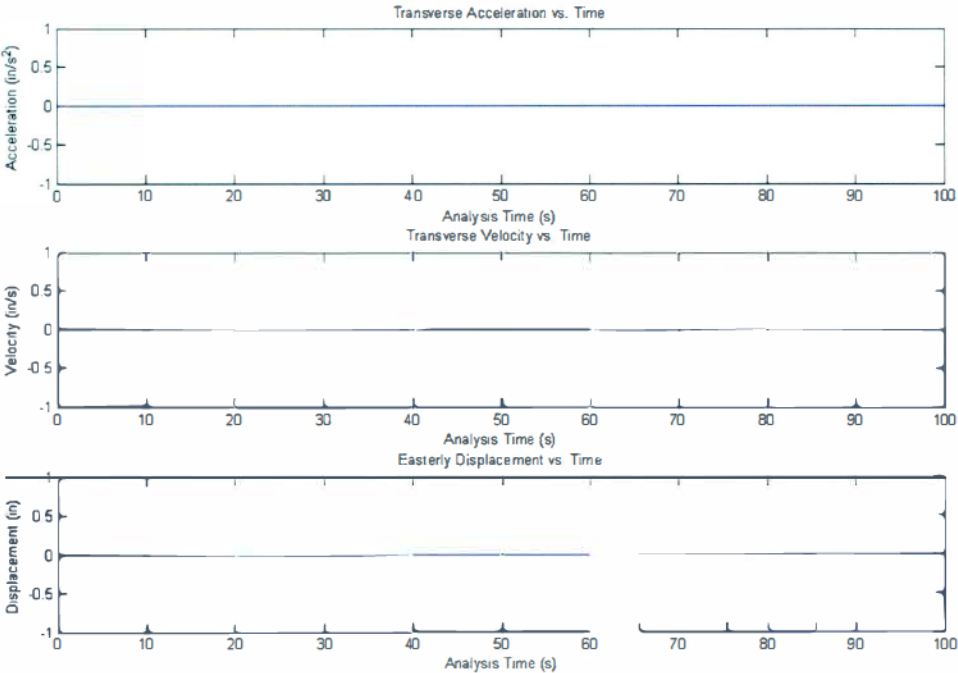


Figure 3.2.3d

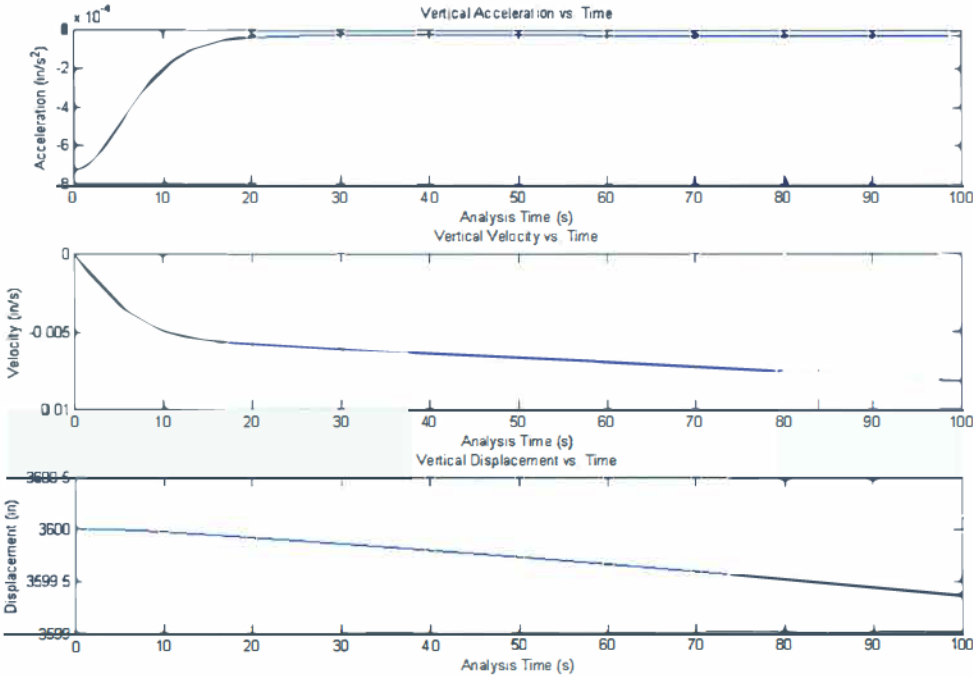




Figure 3.2.3e

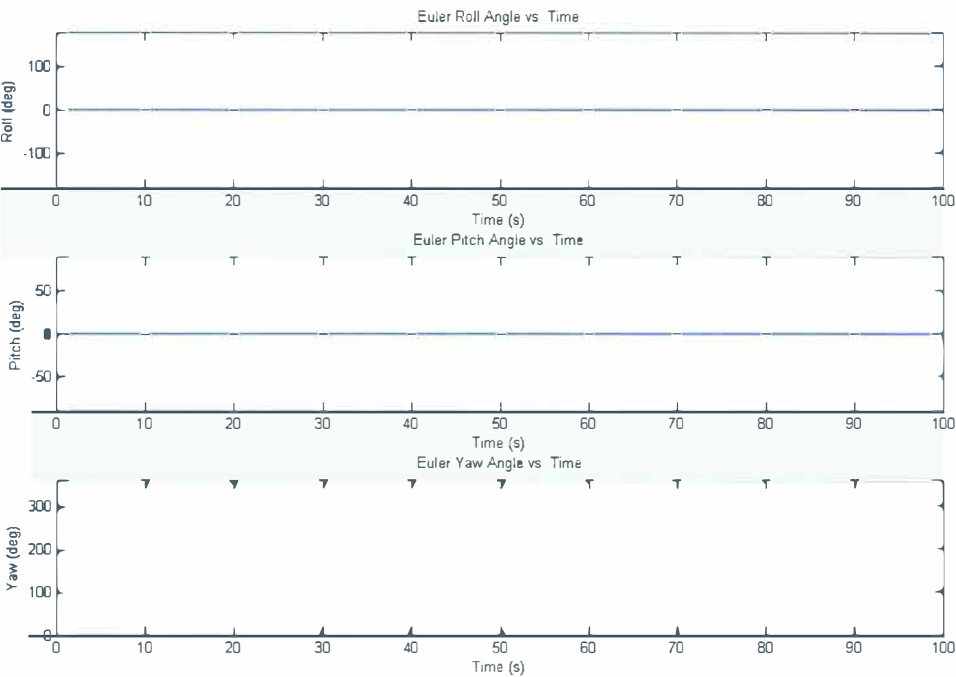
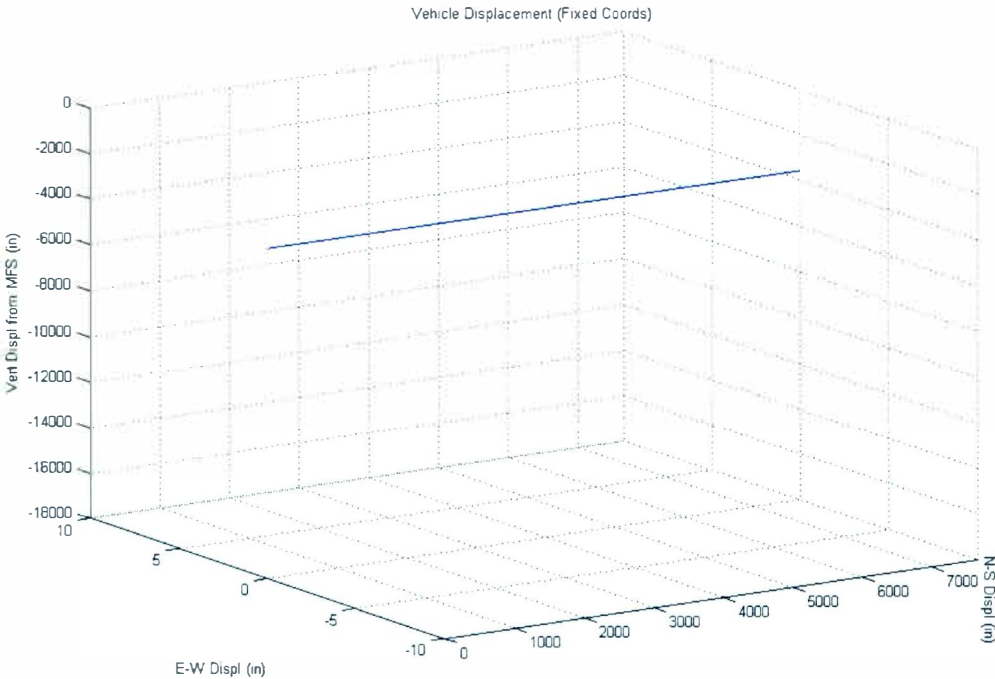


Figure 3.2.3f



**Figures 3.2.4: Simulation Results – Case 3, Positive Bow Plane Deflection**

Figure 3.2.4a

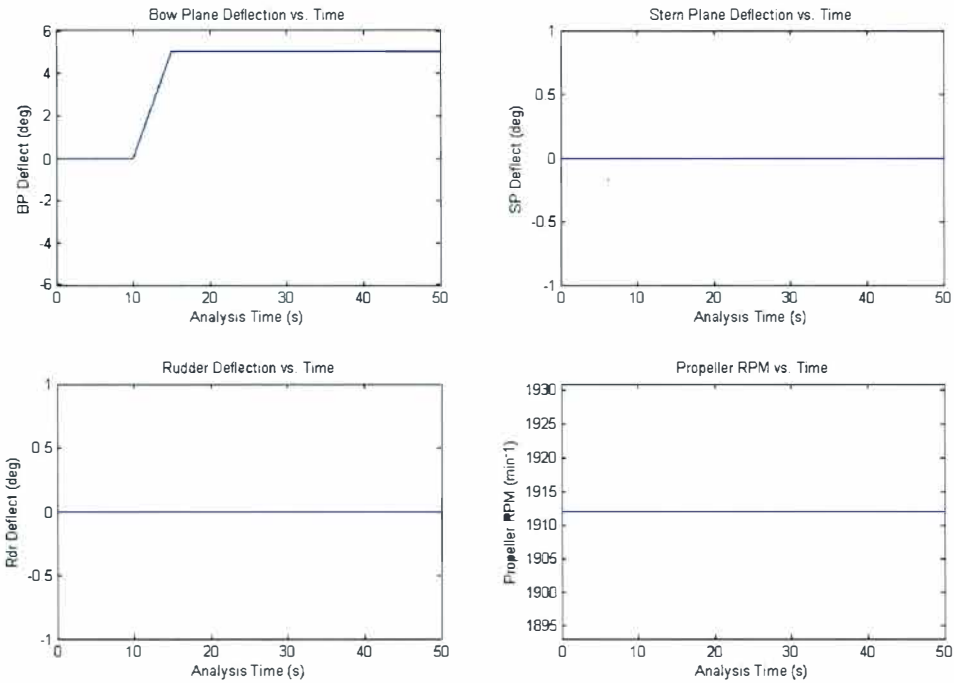


Figure 3.2.4b

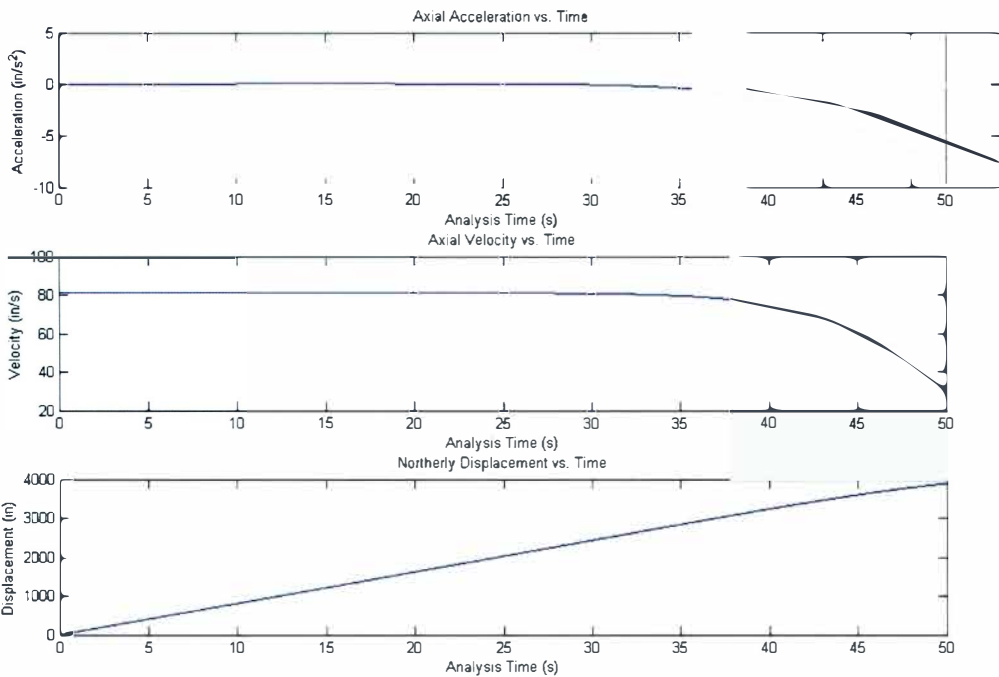


Figure 3.2.4c

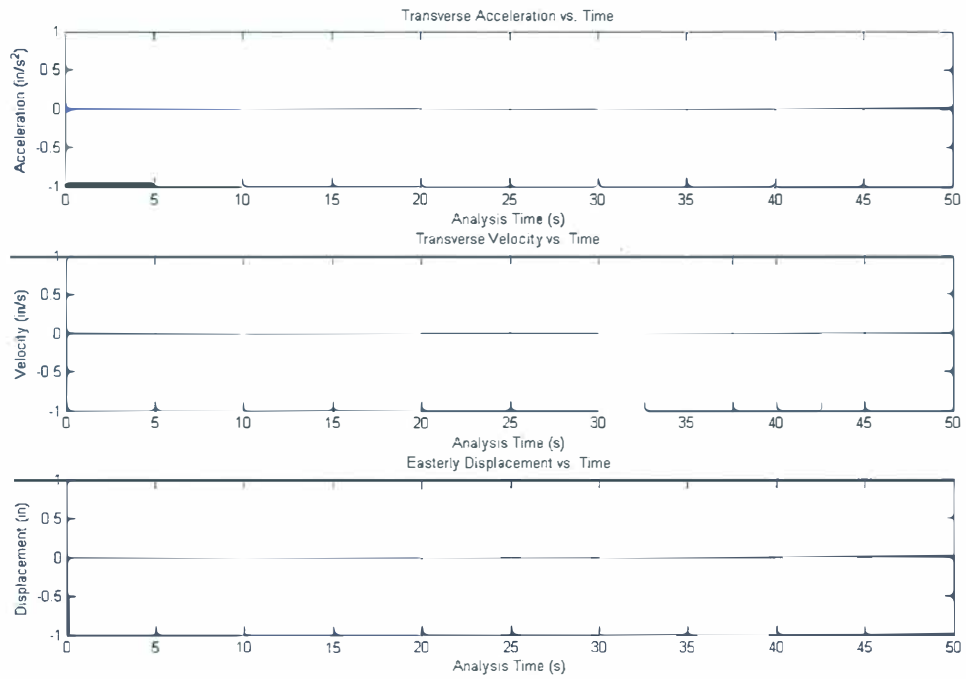


Figure 3.2.4d

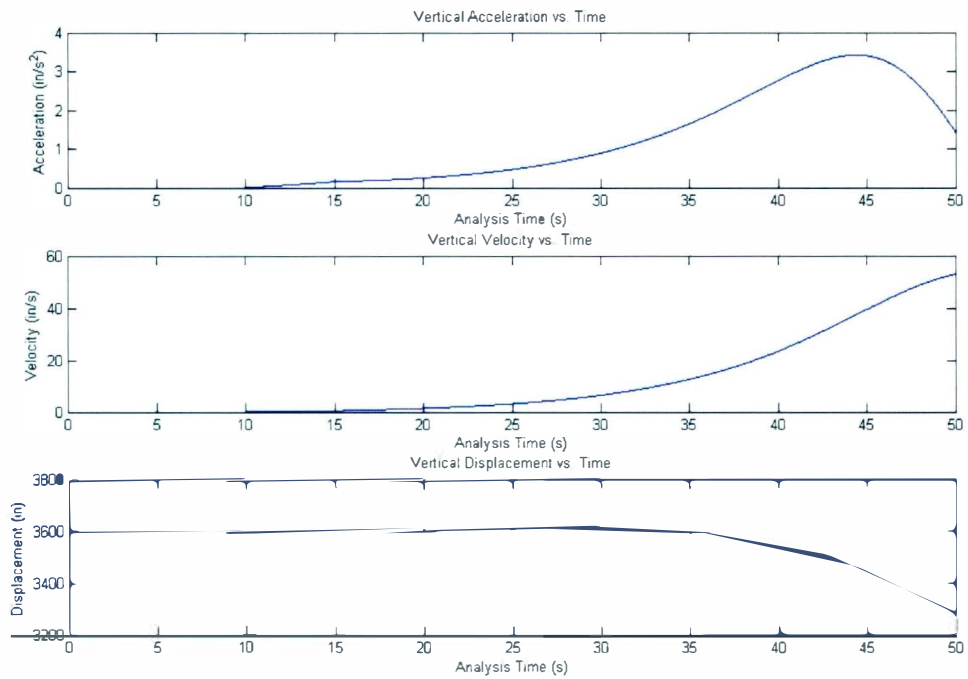


Figure 3.2.4e

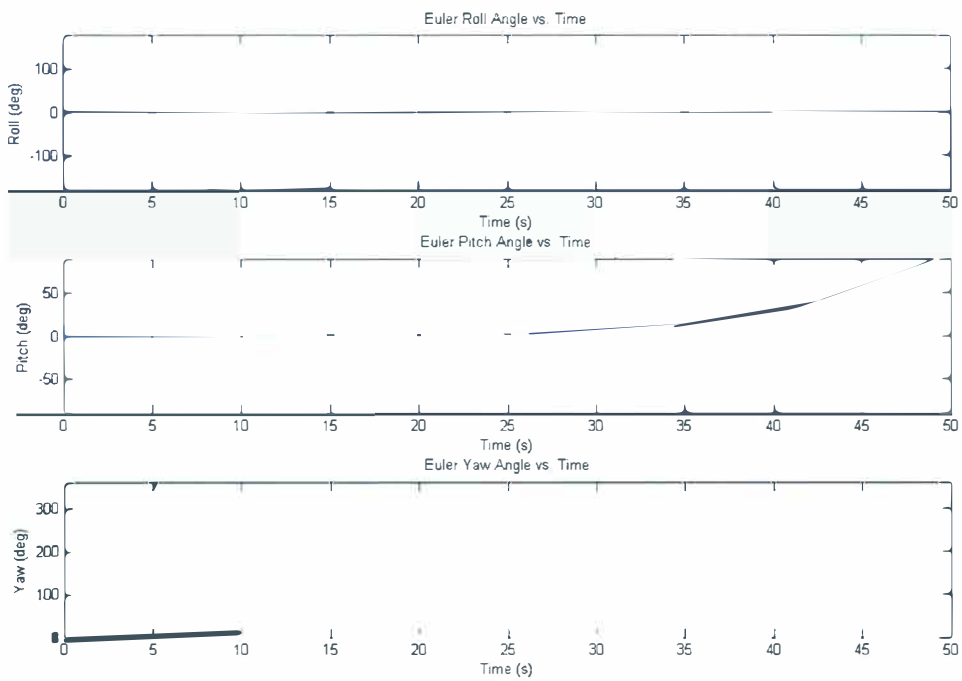
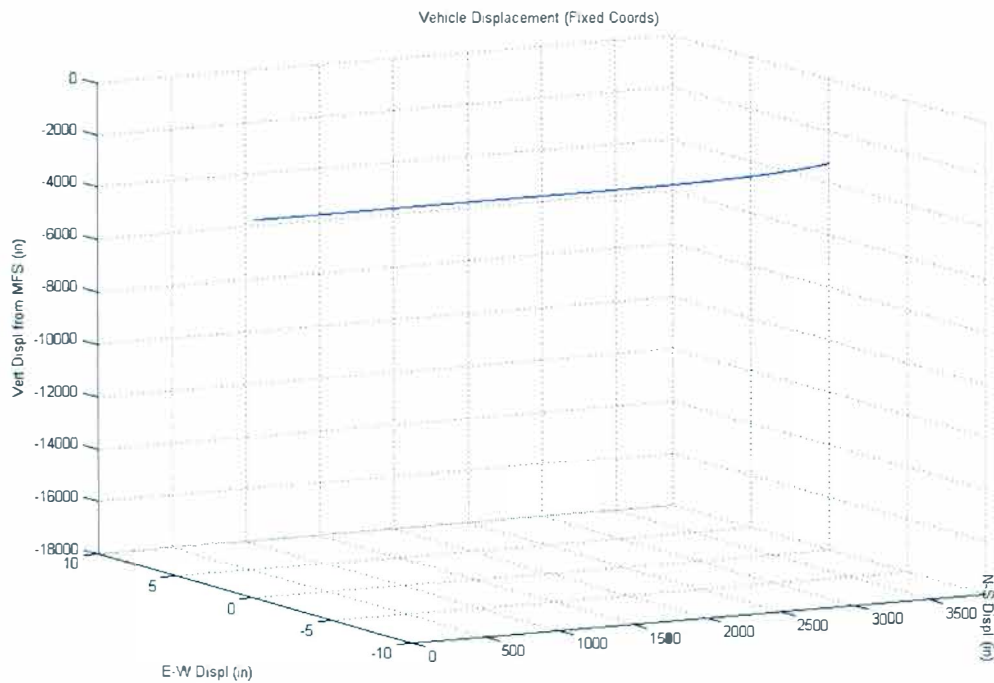


Figure 3.2.4f



## Figures 3.2.5: Simulation Results – Case 4, Constant Positive Pitch Angle

Figure 3.2.5a

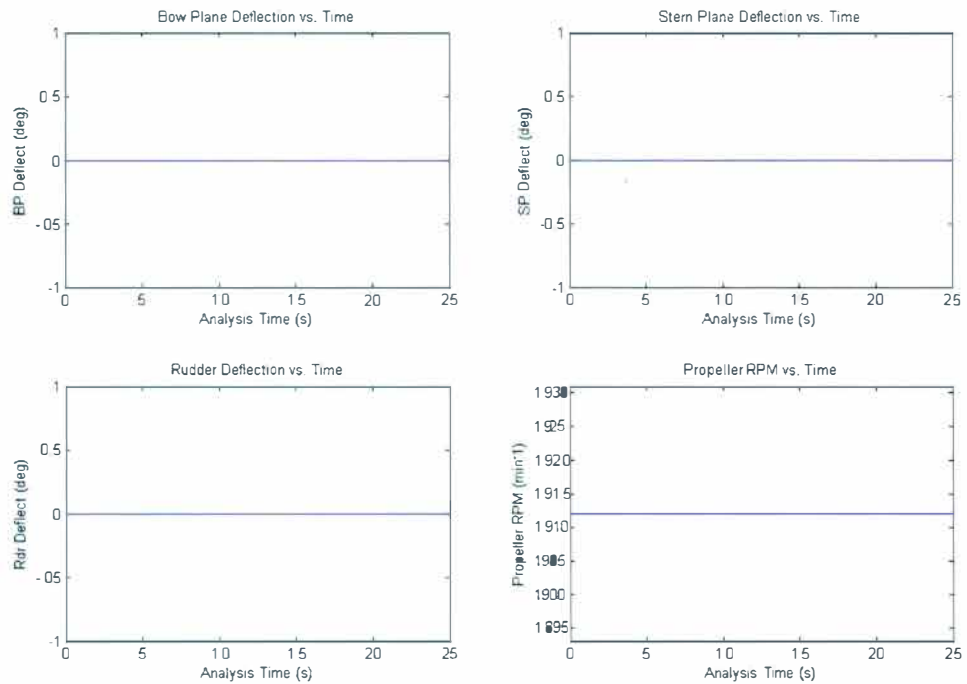


Figure 3.2.5b

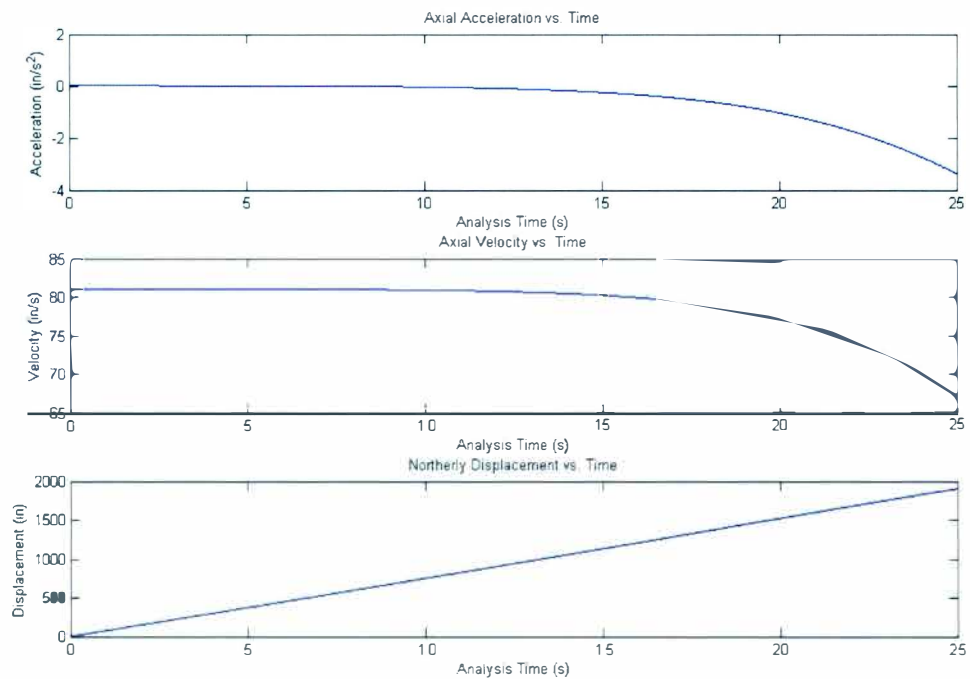


Figure 3.2.5c

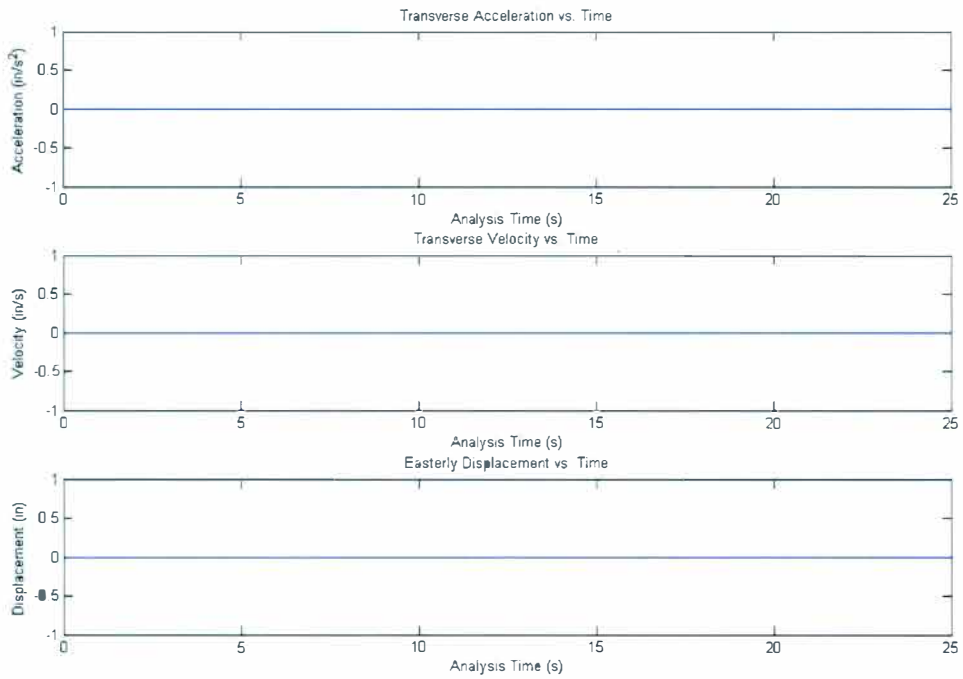


Figure 3.2.5d

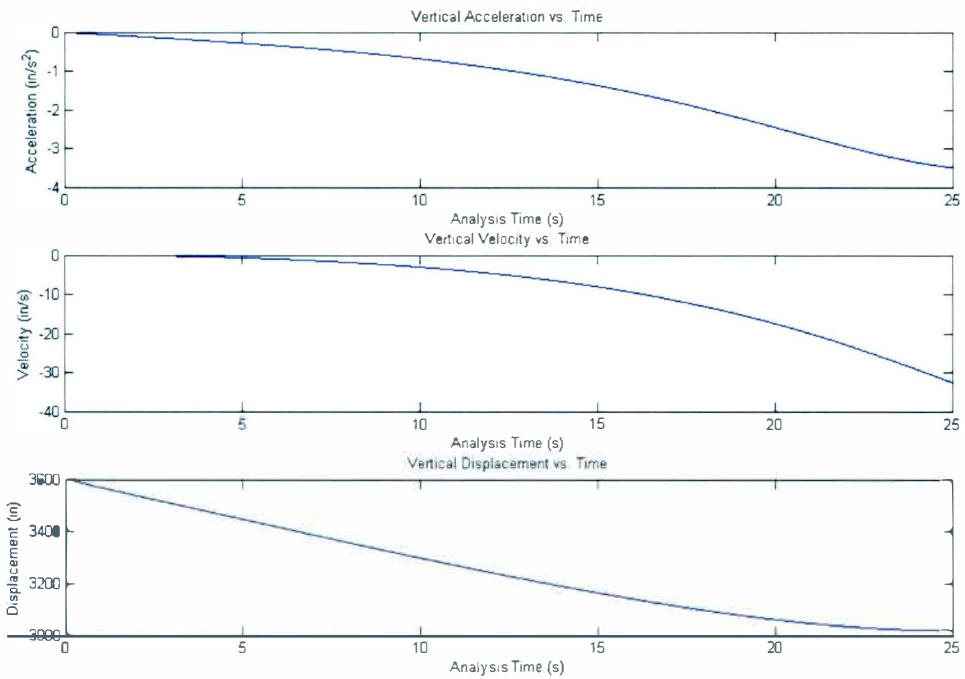


Figure 3.2.5e

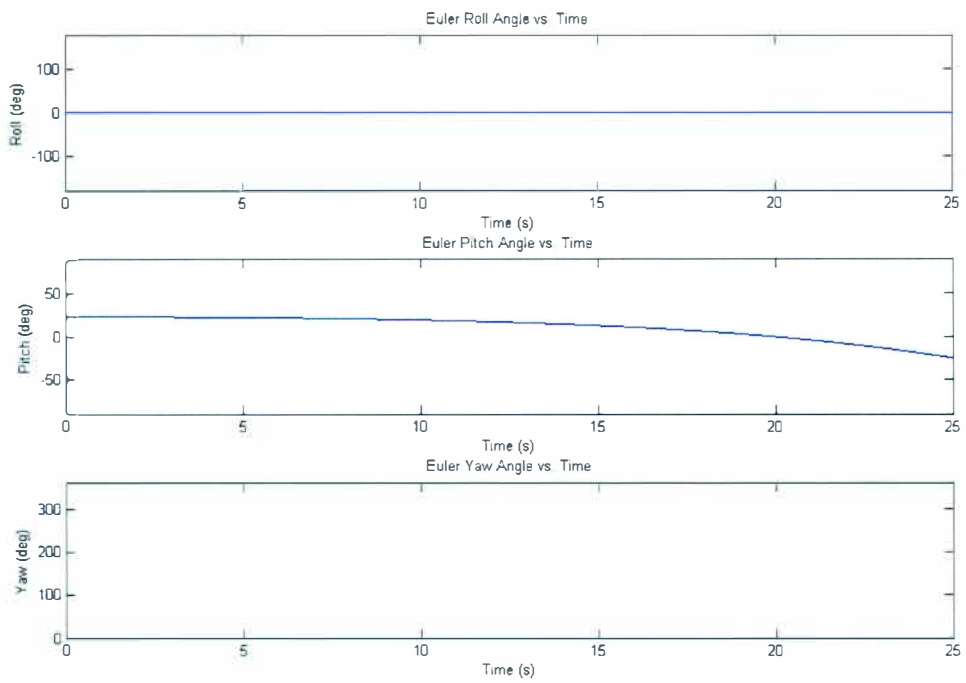
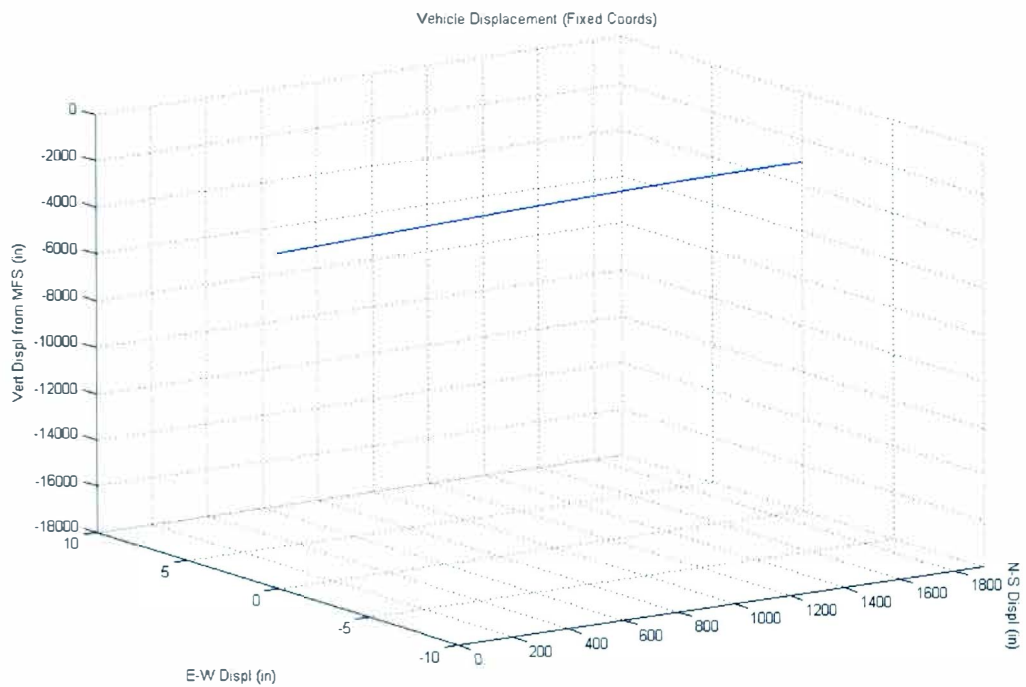


Figure 3.2.5f



## Figures 3.2.6: Simulation Results – Case 5, Negative Rudder Deflection

Figure 3.2.6a

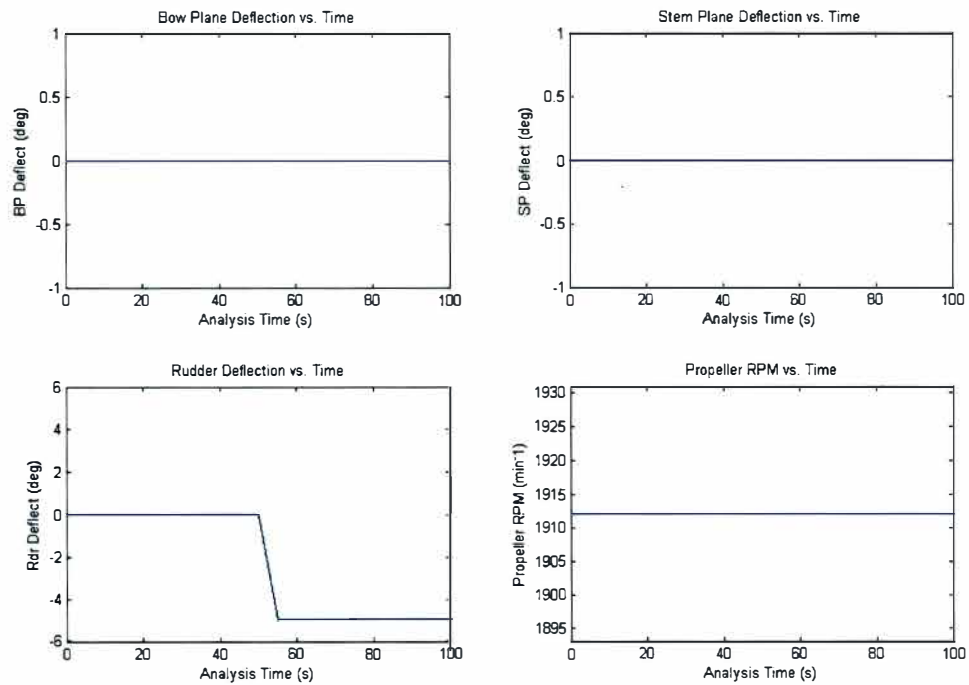


Figure 3.2.6b

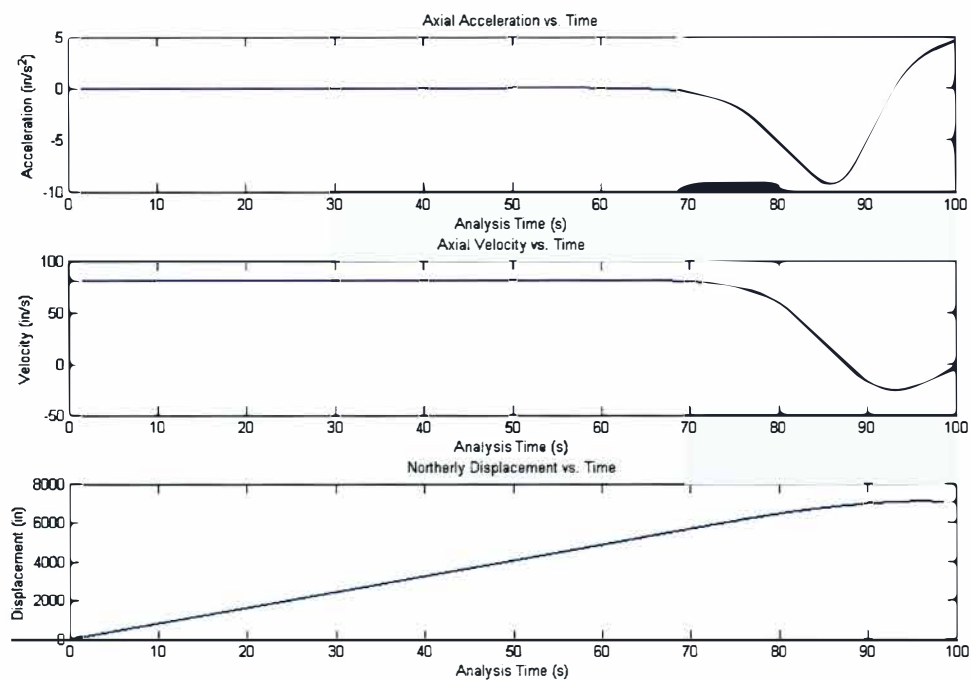




Figure 3.2.6c

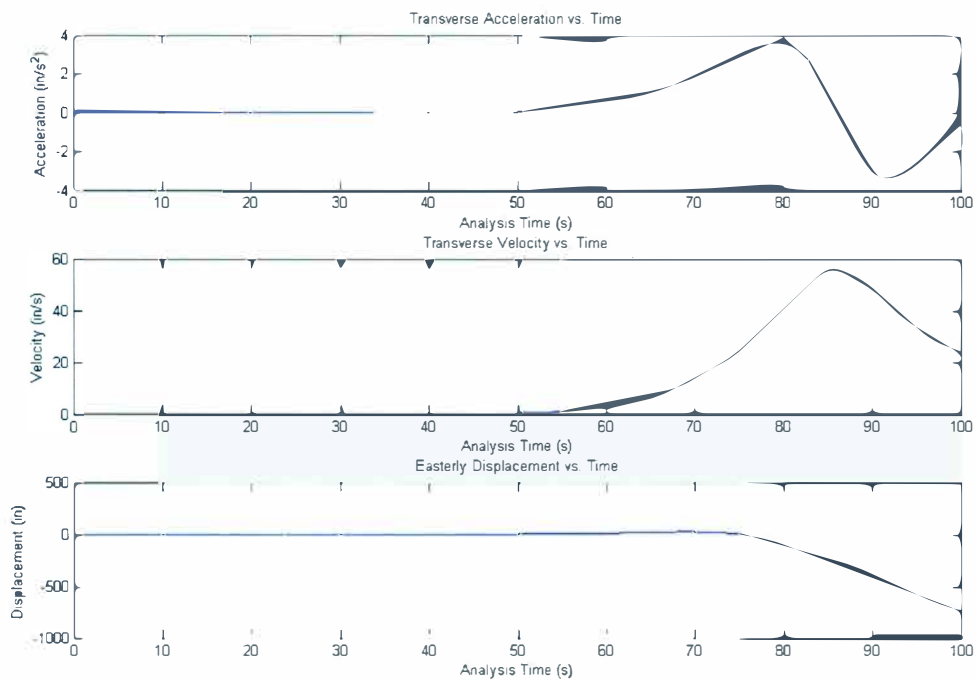


Figure 3.2.6d

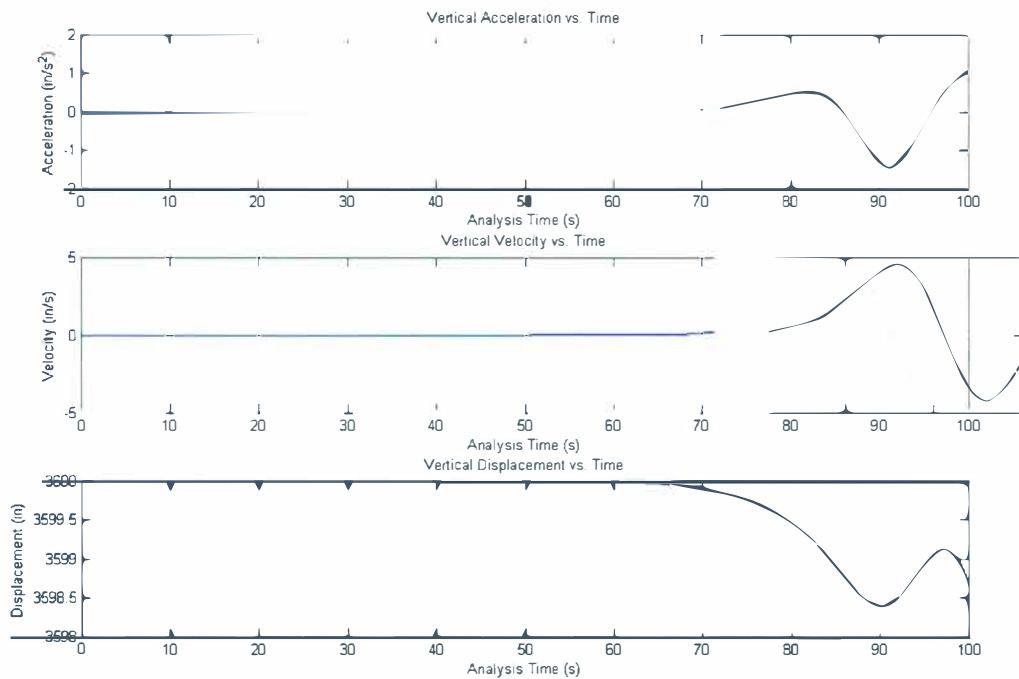


Figure 3.2.6e

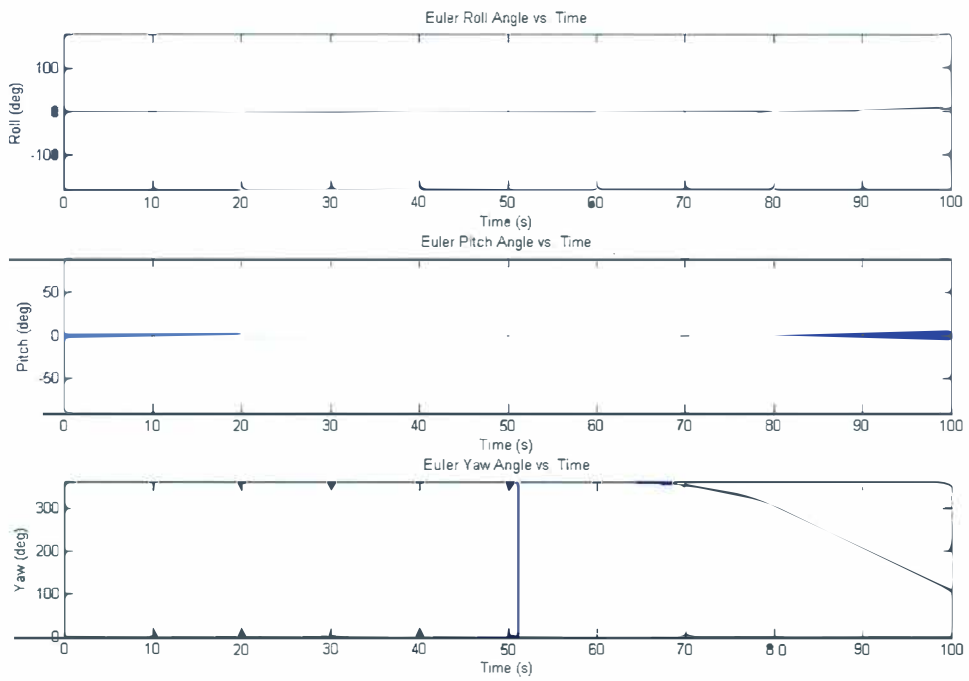
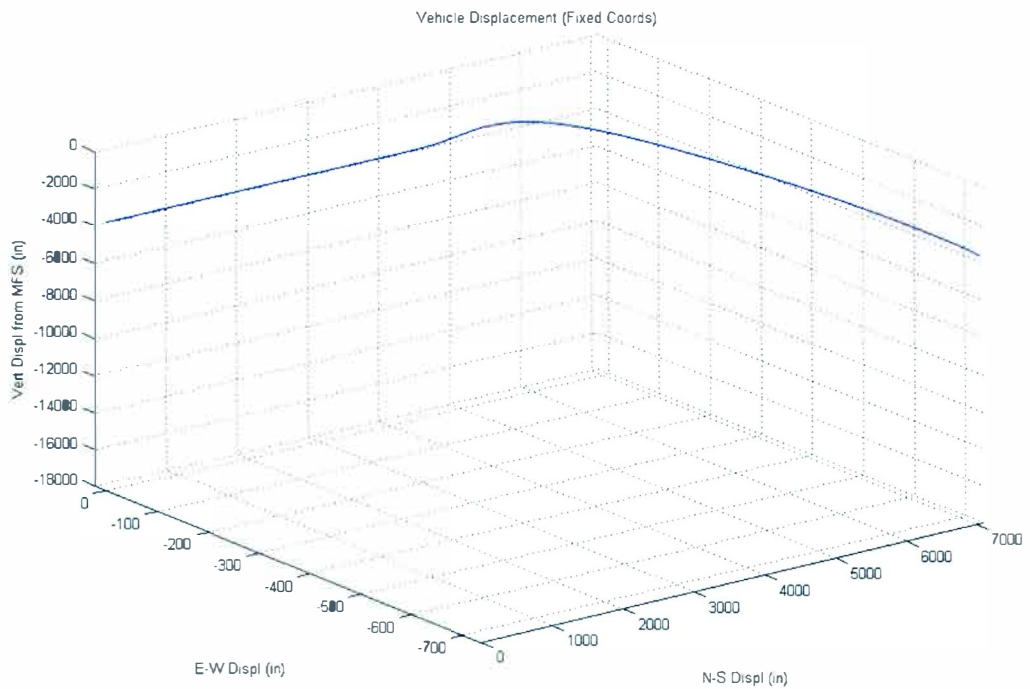


Figure 3.2.6f



**Figures 3.2.7: Simulation Results – Case 6, Level Oblique Rise**

Figure 3.2.7a

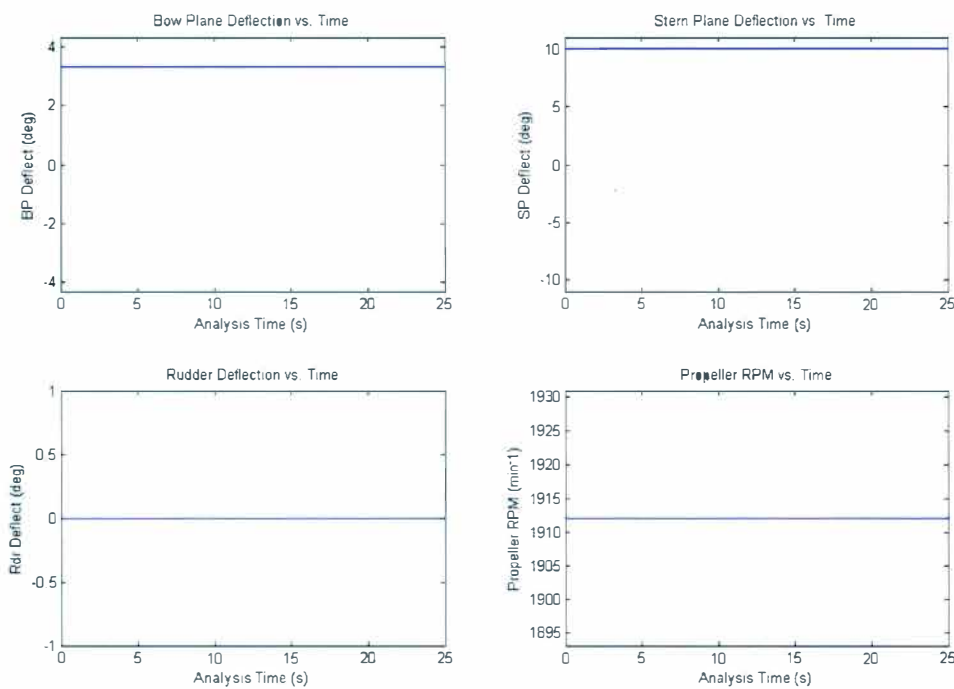


Figure 3.2.7b

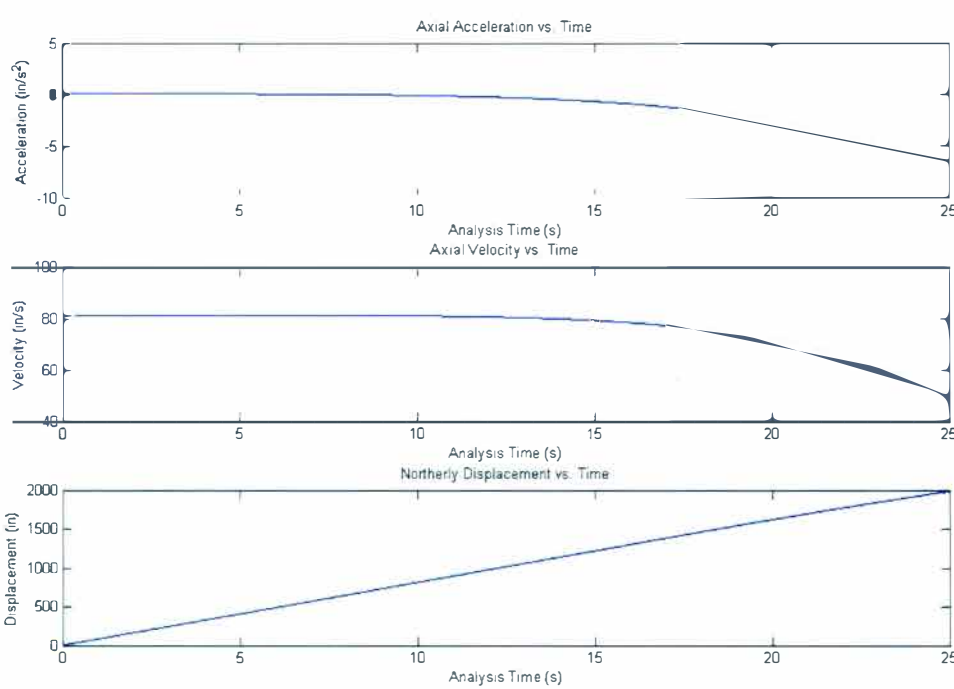


Figure 3.2.7c

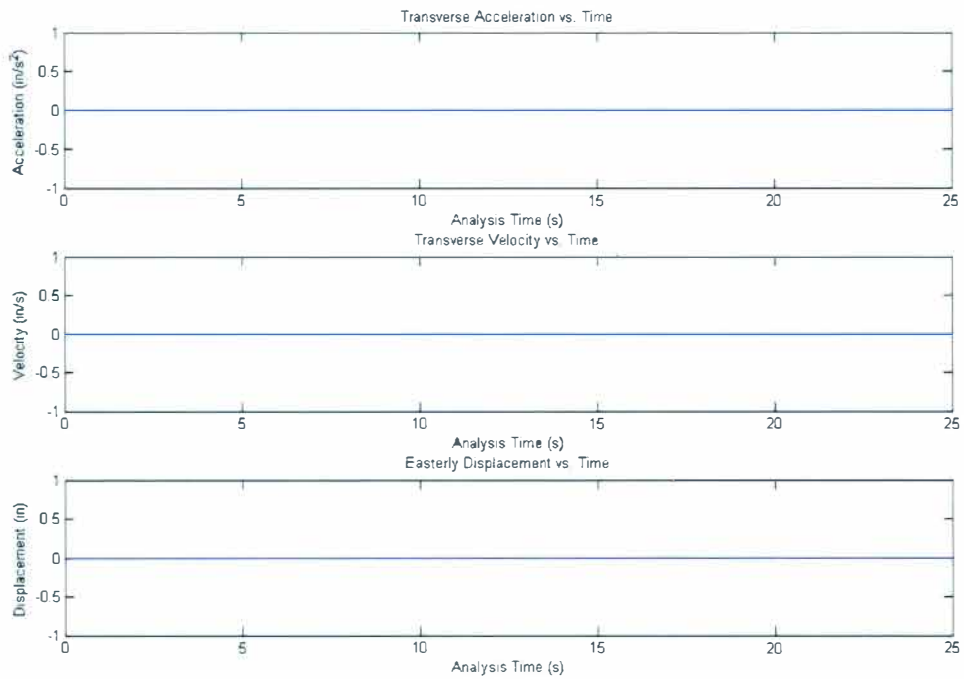


Figure 3.2.7d

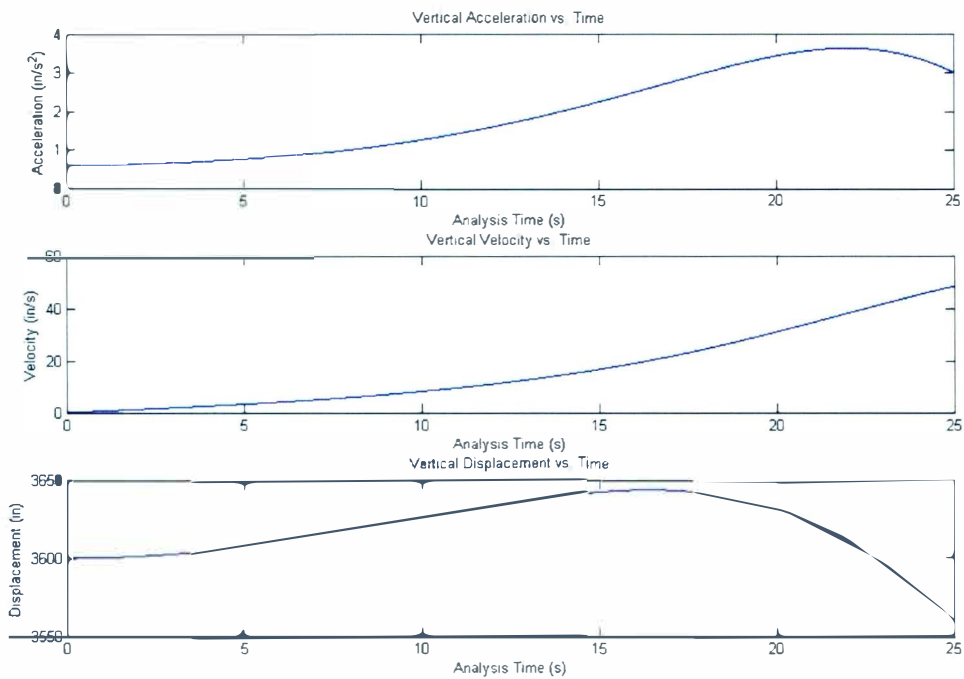


Figure 3.2.7e

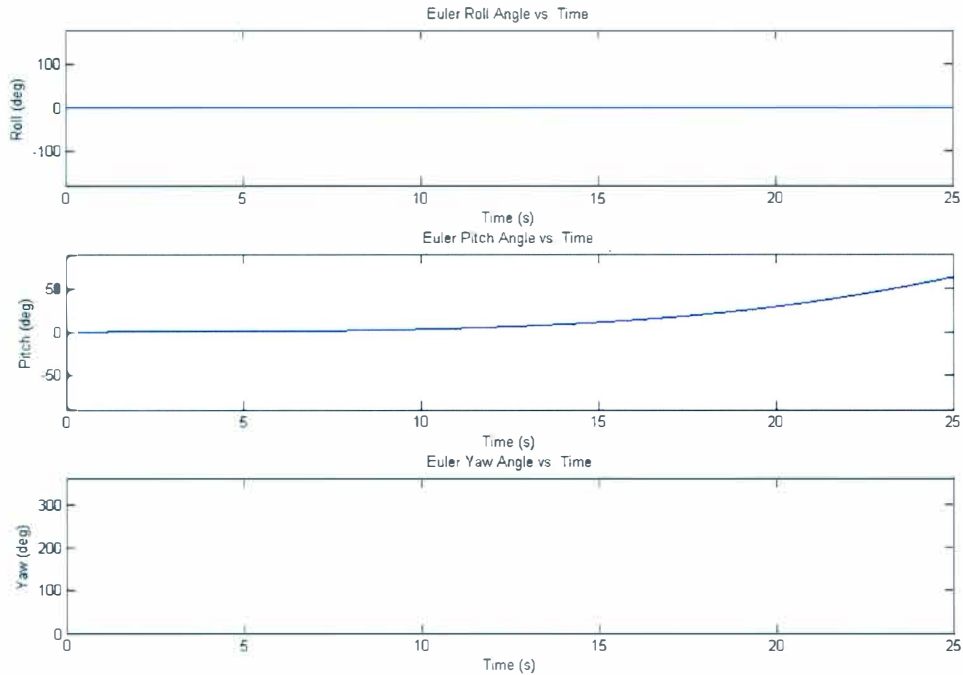
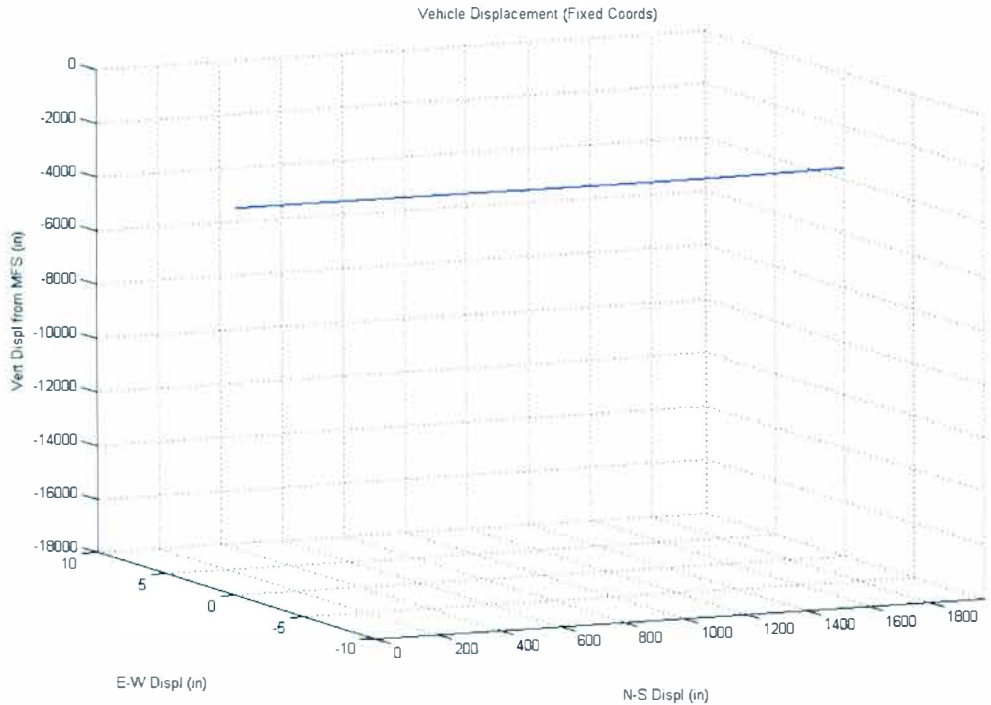


Figure 3.2.7f



Case 1, shown in Figures 3.2.2, simulated the *Deep 6* operating at its design condition. The *Deep 6*'s design condition consisted of a level posture with all of the control fins aligned with the hull ( $0^\circ$  deflection) and moving at the service speed of 4 kts. Figure 3.2.2a shows the time history of the control parameters, which reflect their appropriate position for the design condition. The simulation for Case 1 lasted 100 sec. All of the initial conditions for this case were set to zero, except the propeller rate of revolution, forward velocity, and the depth. The response predicted by Underwater Vehicle Simulator was as expected – straight ahead travel with no body rotations (visible in Figures 3.2.2e and 3.2.2f). The lack of transverse and vertical accelerations, velocities, and displacements, as well as body rotations is visible in Figures 3.2.2b – 3.2.2e. The steady-state design condition served as the equilibrium condition about which the non-linear EOM were later linearized.

The Case 2 simulation predicted the behavior of the *Deep 6* as if it were initially at rest and at the start of the analysis time power was provided to the propulsion motor. The initial conditions for this analysis were all zero except for the propeller rate of revolution and the initial depth. The initial rate of revolution was set to be the service rate of 1,912 rpm, while the depth was set at 3,600 in. The analysis time for this simulation was 100 sec. Figures 3.2.2c – 3.2.2f show that the vehicle moved along a straight line. Figure 3.2.2b shows that the initial vehicle forward speed is zero and increases to the service speed of 4 kts. The response of the vehicle to the diminishing excess propulsion thrust was as expected.

The Case 3 simulation predicted the behavior of the *Deep 6* when its bow planes provided a positive deflection of  $5^\circ$  after 10 sec. The initial conditions for this case were identical to those for Case 1. The definition of positive fin deflection, moments, and rotations shown in Figure 2.4.1 reveals that a positive bow plane deflection will produce a positive (nose up) pitching moment. Figures 3.2.4e and 3.2.4f show that Underwater Vehicle Simulator did predict the expected response for the *Deep 6*. These figures also imply the sluggishness of the *Deep 6*'s responses. At least a portion of the slow response time is due to the high density of the fluid in which the *Deep 6* operates. The pitch angle, shown in Figure 3.2.4e, continues to increase for the *Deep 6* because the constantly deflected bow planes continuously produce a pitching moment. The constant pitching moment leads to an ever increasing pitch angle. For this reason, the simulation for Case 3 had to be performed over the short time interval of 50 sec. to prevent the vehicle's near vertical posture from initiating Underwater Vehicle Simulator's error routine.

The Case 4 simulation predicted the vehicle behavior when an initial pitch angle had been given. The initial pitch angle used for this simulation was  $+22.5^\circ$ . All of the initial conditions, save the pitch angle, were identical to those for Case 1. Figure 3.2.5f shows that Underwater Vehicle Simulator predicted that the *Deep 6* would traverse along an oblique line, as was expected. Figure 3.2.4e predicts that the pitch angle for the *Deep 6* will decrease shortly after the analysis begins. This behavior is due to the righting moment that is created by the offset between the CG and the CB when the vehicle pitches. This response, as well as the changes in the forward velocity, was expected and

is also similar to the response experienced by pitching (stable) airplanes operating with open-loop controls [41].

The Case 5 simulation predicted the vehicle's response to a  $-5^\circ$  rudder deflection. The initial conditions for Case 5 were identical to those used for Case 1. The analysis time for this case was set at 100 sec. and the rudder was set to begin deflecting after 50 sec. The response shown in Figure 3.2.6f reveals many expected characteristics. The first characteristic that was expected was the initial eastward translation of the *Deep 6* immediately before the turn towards the port began. In controls this behavior is attributed to a non-minimum phase zero [21]. Physically, this behavior is attributed to the fact that the vehicle responds faster to the force generated by the control fin than it does the moment. This response has been well documented for both marine vehicles and aircraft [34], [41]. The second expected response characteristic is the vehicle's large turning radius [5]. The plots shown in Figure 3.2.6d appear to show substantial vertical instabilities for the *Deep 6*. The responses appear to be drastic due the fact that the scale for these plots is much smaller than the scale used for the rest of the plots displayed. Longer time intervals for Case 5 were attempted so that the steady state turning radius could be displayed. It was discovered that during longer analyses the predicted responses for the *Deep 6* began to diverge from what was expected. This behavior may be, in part, due to numerical instabilities associated with use of the Euler integration routine over long time intervals.



The final simulation presented, Case 6, predicted the response of the *Deep 6* to a coordinated deflection of both the bow and the stern planes. The purpose of this simulation was to verify that the “oblique level rising” capability desired for the vehicle was possible. A free body diagram was used to determine the ratio of bow plane to stern plane deflection ratio. It was determined that the stern planes need to deflect approximately 3 times more than the bow planes to produce no net pitching moment. This condition can be seen in Figure 3.2.7a. The initial conditions for Case 6 were identical to those used for Case 1 except that the bow and stern planes were given an initial deflection. Figure 3.2.7f shows that Underwater Vehicle Simulator predicts that the *Deep 6* is capable of performing the intended maneuver. However, the Euler pitch angle time history, shown in Figure 3.2.7e, reveals that the *Deep 6* may not be able to perform this maneuver without the assistance of a feedback controller for extended periods of time. This behavior was as expected. The unbalanced fore and aft horizontal fin area results in a positive pitching moment when a vertical flow component exists. Therefore, in order for the *Deep 6* to perform this maneuver over long time periods, either the deflection angle ratio needs to be modified or a feedback controller must be used to continuously alter the deflection angle of the fins.

While performing test runs during the creation of Underwater Vehicle Simulator it was discovered that the results generated tended to diverge from the expected behavior towards the end of the analysis interval. An investigation into the source of these unexpected responses revealed that the solutions contained slight discrepancies as a result of computer induced numerical rounding errors. The discrepancies that were produced

were typically on the order of  $10^{-12}$  to  $10^{-28}$ . While an error of such a magnitude might not be noticeable for a single solution, the errors were propagated from one iteration to the next. After many iterations, say 100,000, the accumulated errors would become significant enough to significantly influence the vehicle's behavior in unexpected ways. To prevent numerical errors from deteriorating the quality of the simulation a "small value filter" was created and applied to the solution after each iteration. The filter was set to restore any value smaller than  $10^{-8}$  back to a value of 0. Subsequent simulations no longer contained the aforementioned peculiarities for higher number iterations.

### 3.3 Linearization

After the non-linear simulations were performed, the non-linear vehicle model was linearized to create a linear state-space vehicle model about an equilibrium condition. The equilibrium condition that was used for the linearization process was the level, steady-state, or "design", condition. Case 1 of the simulation results that were presented in the previous section depicts the design condition for the *Deep 6*. The simulation results generated for Case 1 served as inputs to the linearization routine. The linearization that was performed is a critical step necessary for the design of a vehicle control system [41], [39].

The linearization process was performed using small perturbation theory [41], [42]. Small perturbation theory assumes that, while the overall vehicle behavior may be non-linear, the vehicle behavior can be approximated as linear over a small region immediately surrounding the equilibrium condition. This method required a set of non-

linear differential equations arranged in a form similar to the one presented in Equation 3.1.1b. Once a set of differential equations were obtained, a two variable Taylor series expansion was performed on the equations. The general equation that resulted for the Taylor series expansion has been shown in Equation 3.3.1.

---

**Equation 3.3.1: Taylor Series Expansion, General Form**

$$\{\dot{X}_e(t)\} + \{\Delta\dot{X}(t)\} = \{f(\{X_e\}, \{U_e\})\} + \{\Delta X\} \left. \frac{d\{f\}}{d\{X\}} \right|_{\{X\}=\{X_e\}} + \{\Delta U\} \left. \frac{d\{f\}}{d\{U\}} \right|_{\{U\}=\{U_e\}} + H.O.T.$$

Where the subscript “e” is used to signify the equilibrium condition and “H.O.T.” represent the higher order terms that have not been considered in this first order approximation.

---

The  $\{\dot{X}_e(t)\}$  term on the left hand side of Equation 3.3.1 and the  $\{f(\{X_e\}, \{U_e\})\}$  term on the right hand side of the same equation represent Equation 3.1.1b. Since these two terms must be equal as a result of the statement of Equation 3.1.1b, they can be removed from Equation 3.3.1 without affecting the equality presented. The analyses performed during this investigation were only first order; therefore, the higher order terms from Equation 3.3.1 can be removed without adversely affecting the desired results. Equation 3.3.2 displays Equation 3.3.1 after these simplifications had been applied [42].

---

**Equation 3.3.2: Linearized Equations of Motion**

$$\{\Delta\dot{X}(t)\} = [A_2]\{\Delta X\} + [B_2]\{\Delta U\}$$

Where  $[A_2]$  and  $[B_2]$  represent  $\left. \frac{d\{f\}}{d\{X\}} \right|_{\{X\}=\{X_e\}}$  and  $\left. \frac{d\{f\}}{d\{U\}} \right|_{\{U\}=\{U_e\}}$ , respectively. The coefficient matrices,  $[A_2]$  and  $[B_2]$ , are referred to as the Jacobian matrices [42].

---

The linearization routine incorporated into Underwater Vehicle Simulator was an adaptation of the routine presented by Stevens and Lewis [42]. The Jacobian matrices determined by the linearization routine for the *Deep 6* operating under Case 1 conditions are shown in Figures 3.3.1 and 3.3.2.

**Figure 3.3.1: Linearized  $[A_2]$  Coefficient Matrix**

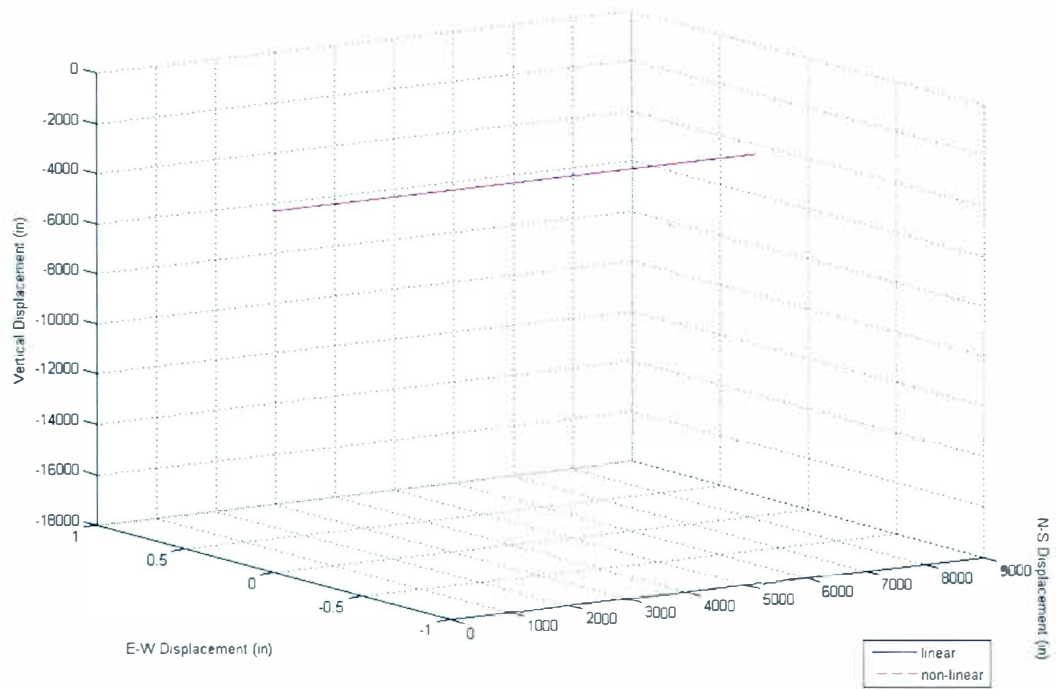
[A <sub>2</sub> ] columns 1-6					
-2.6E-01	0	0	0	2.3E-01	0
0	0	0	9.1E-03	0	-8.0E+02
1.8E-05	0	0	9.8E-11	7.9E+02	0
0	0	0	0	0	1.4E+00
2.1E-06	0	0	0	-1.9E-01	0
0	0	0	-6.3E-04	0	-1.4E-01
1.0E+00	0	0	0	0	0
0	1.0E+00	0	0	0	0
0	0	1.0E+00	0	0	0
0	0	0	1.0E+00	0	0
0	0	0	0	1.0E+00	0
0	0	0	0	0	1.0E+00
[A <sub>2</sub> ] columns 7-12					
0	0	0	0	3.7E-03	0
0	0	0	-3.9E-03	0	0
0	0	0	0	-2.7E-02	0
0	0	0	-1.8E-01	0	0
0	0	0	0	-3.1E-03	0
0	0	0	0	0	0
0	0	0	0	0	0
0	0	0	0	0	8.1E+01
0	0	0	0	-8.1E+01	0
0	0	0	0	0	0
0	0	0	0	0	0
0	0	0	0	0	0

**Figure 3.3.2: Linearized [B<sub>2</sub>] Coefficient Matrix**

0	0	-6.6E-12	1.1E-02
0	0	5.8E-02	0
2.8E-02	5.0E-02	0	-7.6E-07
0	0	-5.3E-05	0
0	0	0	-8.9E-08
0	0	0	0
0	0	0	0
0	0	0	0
0	0	0	0
0	0	0	0
0	0	0	0
0	0	0	0

To verify that the linearization routine was performed correctly and that the assumptions accepted by the small perturbation theory were valid, a comparison between the results generated by the non-linear and the linear vehicle models was conducted. In order for the linearized model to be acceptable, there should be no significant difference between the two sets of results for “conservative” maneuvers. Figure 3.3.3 displays the 3D displacement comparison plot that was generated during the investigation. The comparison shown in Figure 3.3.3 was performed for the design condition. As can be seen in Figure 3.3.3, there is no significant difference between the two results. While Figure 3.3.3 alone cannot confirm the validity of the Jacobian matrices that were determined, it does show that the linearization routine is capable of producing reasonable results.

**Figure 3.3.3: Non-Linear vs. Linear EOM Comparison Plot**



## CHAPTER FOUR

### CONCLUSIONS AND FUTURE WORK

#### 4.1 Conclusions

The scope of this research involved the preliminary design of a new AUV, the *Deep 6*, and laid the foundation necessary for the creation of an autopilot control system. The *Deep 6* was created to provide unrestricted access to the parameters necessary for the construction of a mathematical model of the vehicle. The mathematical model was a first order approximation that was developed using analytical techniques. The subsequent simulation combined the mathematical model with a system of coupled, non-linear, 6 degree of freedom equations of motion to predict the *Deep 6*'s responses to various control inputs (such as control fin deflections). Over short time periods, the maneuvers predicted by the non-linear simulation program were as expected and are comparable to those published for other vehicles. As a final step, the non-linear simulation equations of motion were linearized about an equilibrium condition. The linearization was done to complete the preliminary work necessary for the development of an autopilot control system.

#### 4.2 Future Work

The scope of this project laid all of the ground work necessary for the design of a control system. The next step in the development of the *Deep 6* would be to create an autopilot control system. The controller design would utilize the linearized state-space model that was developed to determine the vehicle transfer functions, which are necessary for the

controller design. The design of the control system would include a stability analysis of the vehicle's motions. This investigation would reveal any instabilities and unfavorable cross-couplings between the vehicles motions. Should any unfavorable vehicle performance characteristics or cross-couplings be discovered during the investigation, the vehicle design would need to be revisited.

Completion of the control system would move the design of the *Deep 6* one more step towards the eventual construction of a working prototype. Prior to the construction of the prototype, completion of the component level design and an investigation into the effects of the simplifying assumptions made during the preliminary design would need to be preformed. Testing of the working prototype would allow for confirmation of the work contained within this study. The results gathered from prototype testing would allow for further refinement of the simulation program. This refinement would, in turn, lead to a more accurate design of future vehicles.

Finally, additional research should be done to investigate current methodology for the design of contra-rotating propellers. This information would allow a more accurate propulsion system model to be generated, which would in turn lead to more accurate simulations and controllers.



## REFERENCES

- [1] Abbott, Ira H., and Albert E. Von Doenhoff. *Theory of Wing Sections*. New York: Dover Publications, 1959.
- [2] Aerologic. *Digital Wind Tunnel CMARC*. Los Angeles: Aerologic, 2003.
- [3] Allmendinger, E. E., ed. *Submersible Vehicle System Design*. Jersey City: Society of Naval Architects and Marine Engineers (SNAME), 1990.
- [4] Ananthakrishnan, P., and S. Decron. "Dynamics of Small- and Mini-Autonomous Underwater Vehicles Part I. Analysis and Simulation for Midwater Applications." July 2002. <http://www.oe.fau.edu/~anath/AUV-Hydro-FAU-2000-I.pdf>.
- [5] Anderson, Jamie M., and Peter A. Kerrebrock. "The Vorticity Control Unmanned Undersea Vehicle [VCUUV]: An Autonomous Robot Tuna." 11<sup>th</sup> International Symposium on Unmanned Untethered Submersible Technology. Durham. 23 Aug 1999.
- [6] "ARCS." 6 Mar. 2002. International Submarine Engineering, Ltd. <http://www.ise.bs.ca/arcs.html>.
- [7] "Aries – Acoustic Radio Interactive Exploratory Server." Office of Naval Research. <http://www.cs.nps.navy.mil/research/auv/auvframes.html>.
- [8] "Autonomous Benthic Explorer (ABE)." NOAA Ocean Explorer. <http://www.oceanexplorer.noaa.gov/technology/subs/abe/abe.html>.
- [9] Baruh, Haim. *Analytical Dynamics*. Boston: WCB McGraw-Hill, 1999.
- [10] Breslin, J. P., and P. Andersen. *Hydrodynamics of Ship Propellers*. New York: Cambridge University Press, 1996.

- [11] Brutzman, Donald P. "Underwater Vehicle Dynamics Model" *A Virtual World for an Autonomous Underwater Vehicle*. Monterey: Naval Postgraduate School, 1994. 89-170.
- [12] Bullivant, W. Kenneth. "Tests of the NACA 0025 and 0035 Airfoils in the Full-Scale Wind Tunnel." 1941. NACA. <http://naca.larc.nasa.gov/reports/1941/naca-report-708/naca-report-708.pdf>.
- [13] Burcher, R. K., and L. J. Rydill. *Concepts in Submarine Design*. New York: Cambridge University Press, 1998.
- [14] "Contra-Rotating Propeller System." 2000. Mitsubishi Heavy Industries, Ltd. <http://www.mhi.co.jp/ship/english/htm/crp01.htm>.
- [15] Dean, Robert G. and Robert A. Dalrymple. *Water Wave Mechanics for Engineers and Scientists*. New Jersey: World Scientific, 1984.
- [16] Earle, Sylvia A. *Atlas of the Ocean, the Deep Frontier*. Washington D.C.: National Geographic.
- [17] "Earlier Builds." AUV Laboratory at MIT Sea Grant. <http://auvlab.mit.edu/vehicles/vehiclespecEARLY.html>.
- [18] Feldman, J. "Revised Standard Submarine Equations of Motion." Report DTNSRDC/SPD-0393-09. Bethesda: David W. Taylor Naval Ship Research and Development Center, June 1979.
- [19] Fossen, Thor I. *Guidance and Control of Ocean Vehicles*. New York: John Wiley & Sons, 1994.
- [20] Fox, Robert W., and Alan T. McDonald. *Introduction to Fluid Mechanics*. 5<sup>th</sup> ed. New York: John Wiley & Sons, Inc., 1998.

- [21] Franklin, Gene F., J. David Powell, and Abbas Emami-Naeini. *Feedback Control of Dynamic Systems*. 5<sup>th</sup> ed. Upper Saddle River: Pearson Prentice Hall, 2006.
- [22] Gertler, M. "Resistance Experiments on a Systematic Series of Streamlined Bodies of Revolution – For Application to the Design of High-Speed Submarines." Report C-297. Washington D.C.: David W. Taylor Model Basin, April 1950.
- [23] Gertler, M., and G. Hagen. "Standard Equations of Motion for Submarine Simulation." Report DTNSRDC 2510. Bethesda: David W. Taylor Naval Ship Research and Development Center, June 1967.
- [24] Giancoli, Douglas C. *Physics for Scientists and Engineers*. 3<sup>rd</sup> ed. New Jersey: Prentice Hall, 2000.
- [25] Harrington, Roy L., ed. *Marine Engineering*. Jersey City: The Society of Naval Architects and Marine Engineers, 1992.
- [26] Huphreys, D. E., and K. W. Watkinson. "Prediction of Acceleration Hydrodynamic Coefficients for Underwater Vehicles from Geometric Parameters." Report NCSL 327-78 Panama City: Naval Coastal Systems Laboratory, July 1978.
- [27] "Hydrodynamic Aspects Contra-Rotating Propeller." 2004. Wartsila.  
[http://www.wartsila.com/Wartsilla/docs/en/ship\\_power/media\\_publications/marine\\_news/2004\\_1/hydrodynamic.pdf#search='wartsilacontrarotating%20propeller'](http://www.wartsila.com/Wartsilla/docs/en/ship_power/media_publications/marine_news/2004_1/hydrodynamic.pdf#search='wartsilacontrarotating%20propeller').
- [28] "ISE Web Based AUV Design Info: Explorer." 2000. International Submarine Engineering, Ltd. <http://www.ise.bs.ca/AUV%20DESIGNINFO.pdf>.
- [29] Jackson, Harry. "Fundamentals of Submarine Concept Design." *SNAME Transactions* 100 (1992): 419-448.

- [30] “Just What is An AUV Anyway.” International Submarine Engineering, Ltd.  
<http://www.ise.bc.ca/WADEwhatisanAUV.html#start>.
- [31] Kotz, John C, and Paul Treichler, Jr. *Chemistry and Chemical Reactivity*. 4<sup>th</sup> ed.  
Fort Worth: Saunders College Publishing, 1999.
- [32] Kristiansen, Arne, Cand Mag, and Arne Hauglund. “New Paradigm for Propulsion.”  
*The Naval Architect* July/August 2003: 40-44.
- [33] Lewis, E. L., ed. *Principles of Naval Architecture*. Vol. 2. 2<sup>nd</sup> ed. Jersey City:  
Society of Naval Architects and Marine Engineers, 1989.
- [34] Lewis, E. L., ed. *Principles of Naval Architecture*. Vol. 3. 2<sup>nd</sup> ed. Jersey City:  
Society of Naval Architects and Marine Engineers (SNAME), 1989.
- [35] Li, Jun. Optimal Wageningen B-Screw Series Propellers. University of Michigan  
Department of Naval Architecture and Marine Engineering. [http://www-  
personal.engin.umich.edu/~parsons/470web/Junli/Propellorweb.html](http://www-personal.engin.umich.edu/~parsons/470web/Junli/Propellorweb.html).
- [36] Myring, D.F. “A Theoretical Study of Body Drag in Subcritical Axisymmetric  
Flow.” *Aeronautical Quarterly*, 27.3 (August 1976): 186-94.
- [37] Nahon, M. “Determination of Undersea Vehicle Hydrodynamic Derivatives Using  
the USAF DATCOM.” Proceedings of IEEE Oceans '93: Engineering in  
Harmony with the Ocean. Victoria, B.C., 1993: 1283-1288.
- [38] Newman, J. N. *Marine Hydrodynamics*. Massachusetts: MIT Press, 1977.
- [39] Prestero, Timothy. “Development of a Six-Degree of Freedom Simulation Model  
for the REMUS Autonomous Underwater Vehicle.” 2001. MIT/WHOI Joint  
Program in Oceanographic Engineering.  
<http://www.mit.edu/~tprester/Oceans2001.pdf>.

- [40] Ridley, Peter, Julien Fontan, and Peter Corke. "Submarine Dynamic Modeling."  
2003. <http://www.araa.asn.au/acra/acra2003/papers/10.pdf>.
- [41] Schmidt, Louis V. *Introduction to Aircraft Flight Dynamics*. Reston: American Institute of Aeronautics and Astronautics, Inc., 1998.
- [42] Stevens, Brian L, and Frank L. Lewis. *Aircraft Control and Simulation*. 2<sup>nd</sup> ed. New Jersey: Prentice Hall, 2003.
- [43] "The HUGIN 3000 AUV." Maxon Motor USA.  
[http://www.maxonmotorusa.com/applicationarticles/article.cfm?id=20030610&title=The%20HUGIN%203000%20AUV%20\(Autonomous%20Underwater%20Vehicle\)](http://www.maxonmotorusa.com/applicationarticles/article.cfm?id=20030610&title=The%20HUGIN%203000%20AUV%20(Autonomous%20Underwater%20Vehicle)).
- [44] "Theseus: An Autonomous Underwater Cable Laying Vehicle." International Submarine Engineering, Ltd. <http://www.ise.bc.ca/theseus.html#specifications>.
- [45] Thomas, George B. and Ross L. Finney. *Calculus and Analytic Geometry*. 9<sup>th</sup> ed. Reading: Addison-Wesley, 1996.
- [46] "Torpedo Troubles." 2002.USS Bowfin Submarine Museum and Park.  
[http://www.bowfin.org/website/bowfin\\_systems/torpedo\\_troubles/torpedo\\_troubles.htm](http://www.bowfin.org/website/bowfin_systems/torpedo_troubles/torpedo_troubles.htm).
- [47] "Unmanned Vehicles." Dec. 2003. Naval Oceanographic Office.  
[http://www.navo.navy.mil/pao/fact\\_sheets/sams\\_seahorse.pdf](http://www.navo.navy.mil/pao/fact_sheets/sams_seahorse.pdf).
- [48] Van Dokkum, Klass. *Ship Knowledge, A Modern Encyclopedia*. The Netherlands: Giethoorn Ten Brink, 2003.
- [49] Von Alt, Christopher. "Autonomous Underwater Vehicles." Autonomous Underwater Lagrangian Platforms and Sensors Workshop. 24 Mar 2003.

- [50] Zubaly, Robert B. *Applied Naval Architecture*. Jersey City: The Society of Naval Architects and Marine Engineers, 1996.

## GLOSSARY

- AOA, angle of attack: the angle between an objects longitudinal axis and the inflow velocity vector.
- AUV, autonomous underwater vehicle (can also stand for advanced underwater vehicle) – this term is synonymous with UUV, unmanned underwater vehicle or untethered underwater vehicle.
- Beam: transverse dimension (width) of marine vessels. The beam may vary with longitudinal and vertical position along a hull. Therefore, the beam typically refers to the widest point for a hull at a specific longitudinal position.
- Bow: the front/forward end of a vessel.
- c, chord: the longitudinal length of a non-cambered foil section, or the shortest distance between the leading and trailing edges of a cambered section.
- CAD: computer aided design/drafting.
- CB, center of buoyancy: the centroid of volume for the object under consideration.
- $C_B$ , block coefficient: the ratio between a body's displaced volume and the volume encompassed by a block with dimensions equaling the vehicle's maximum length (LOA), maximum width (beam), and maximum height (depth). The block coefficient provides a measure of the "fullness" of a hull form.
- CFD, computational fluid dynamics: the method of utilizing a computer to numerically approximate the solution to fluid dynamics equations for those situations that are too complex for analytical solutions.

- CG, center of gravity: the centroid of mass for the object or objects under consideration.
- $C_p$ , prismatic coefficient: the ratio between a body's displaced volume and the volume encompassed by a solid with a constant cross section equal to the maximum cross section of the body and length equal to the body's LOA. The prismatic coefficient provides a measure of the amount of taper at the ends of a hull.
- $\Delta$ , displacement: the weight (or mass) of the vehicle. For marine vehicles, the displacement is equal to the weight (or mass) of a volume of water equal to the vehicle's submerged volume. Mass displacement (commonly used when using the SI system of units) typically attaches a subscript "m" to the delta symbol.
- Depth: the distance between the bottom (keel) of a marine vessel and the waterline (on a submerge body, this dimension equals the total height of the vehicle).
- DOF, degrees of freedom: the number of unconstrained motions a body is allowed. The maximum number is six; three translations and three rotations (each along or about one of the three coordinate axes).
- Entrance: the forward section of a submarine, synonymous with bow and nose. The entrance is characterized as the forward section of the hull spanning from the very front (zero height) to the point of maximum height/diameter.
- EOM, equation(s) of motion: the mathematical description of how external forces and moments affect a body's position and orientation.
- FP, forward perpendicular: the point at which the bow intersects the waterline (for a submarine in the submerged state, this is the tip of the nose).
- Heave: translation along the vertical axis.



- H.O.T., higher order terms: elements of an equation, such as in a Taylor series expansion, that result in producing effects beyond the scope of the intended analysis.
- ITTC, International Towing Tank Conference: governing body for procedures relating to towing tanks (model basins).
- Kts, knots: nautical miles per hour (equivalent to one minute of latitude per hour)
- lbf.: pound force (includes the effects of gravity on a mass to produce a weight).
- LOA, length overall: the absolute maximum longitudinal length of a vehicle.
- NACA, National Advisory Committee for Aeronautics: the predecessor to NASA.
- n.d.: non-dimensional, unitless.
- Pitch: rotation about the transverse axis.
- PMB, parallel mid body: the section of a hull where width (beam) is constant. This term is usually used when the constant width section comprises a notable percentage of the total vehicle length.
- Port: the left hand side when looking toward the bow.
- Principle Particulars: a list of the key dimensions and parameters that define the overall vehicle package (such as maximum length, maximum width (beam), displacement, and service speed). The principle particulars should include the information necessary to identify the specific vehicle amongst a group of others.
- Roll: rotation about the longitudinal axis.
- Run: the aft section of a submarine's hull, synonymous with stern and tail. The run is characterized as the afterword section of the hull spanned from the point of maximum height/diameter to the very end (zero height).

- Spn, span: the “tip to tip” distance for a set of wings or fins (a.k.a. wing span).
- SSpn, semi-span: the distance from the vehicle centerline to the outer tip of a wing or fin (one-half of the span).
- Starboard: the right hand side when looking towards the bow.
- Stern: the back/aft end of a vessel.
- Surge: translation along the longitudinal axis.
- Sway: translation along the transverse axis.
- Table of Offsets: a tabulated list of hull coordinates, usually organized in groupings of longitudinal stations.
- $\nabla$ : volume (of displacement). Volume is also commonly abbreviated by an inverted triangle symbol.
- Yaw: rotation about the vertical axis.

**APPENDIX A: Table of Offsets for the *Deep 6* Hull** (all dimensions in inches)

<b>X</b>	<b>R</b>	<b>X</b>	<b>R</b>	<b>X</b>	<b>R</b>	<b>X</b>	<b>R</b>
0.00	0.000	6.75	3.612	46.35	3.667	53.25	2.715
0.15	0.589	6.90	3.630	46.50	3.659	53.40	2.677
0.30	0.851	7.05	3.646	46.65	3.651	53.55	2.638
0.45	1.055	7.20	3.661	46.80	3.643	53.70	2.598
0.60	1.226	7.35	3.675	46.95	3.634	53.85	2.558
0.75	1.377	7.50	3.688	47.10	3.624	54.00	2.516
0.90	1.513	7.65	3.700	47.25	3.614	54.15	2.474
1.05	1.636	7.80	3.710	47.40	3.604	54.30	2.430
1.20	1.751	7.95	3.719	47.55	3.593	54.45	2.386
1.35	1.857	8.10	3.727	47.70	3.582	54.60	2.341
1.50	1.956	8.25	3.734	47.85	3.570	54.75	2.295
1.65	2.050	8.40	3.740	48.00	3.557	54.90	2.247
1.80	2.138	8.55	3.744	48.15	3.544	55.05	2.199
1.95	2.222	8.70	3.747	48.30	3.531	55.20	2.150
2.10	2.301	8.85	3.749	48.45	3.517	55.35	2.100
2.25	2.377	9.00	3.750	48.60	3.502	55.50	2.049
2.40	2.449	...	...	48.75	3.487	55.65	1.996
2.55	2.518	42.00	3.750	48.90	3.471	55.80	1.943
2.70	2.584	42.15	3.750	49.05	3.455	55.95	1.889
2.85	2.647	42.30	3.750	49.20	3.438	56.10	1.834
3.00	2.707	42.45	3.750	49.35	3.420	56.25	1.777
3.15	2.765	42.60	3.749	49.50	3.402	56.40	1.720
3.30	2.820	42.75	3.749	49.65	3.383	56.55	1.662
3.45	2.874	42.90	3.748	49.80	3.364	56.70	1.602
3.60	2.925	43.05	3.747	49.95	3.344	56.85	1.541
3.75	2.974	43.20	3.747	50.10	3.323	57.00	1.480
3.90	3.021	43.35	3.745	50.25	3.301	57.15	1.417
4.05	3.066	43.50	3.744	50.40	3.279	57.30	1.353
4.20	3.109	43.65	3.743	50.55	3.256	57.45	1.288
4.35	3.151	43.80	3.741	50.70	3.233	57.60	1.221
4.50	3.191	43.95	3.739	50.85	3.208	57.75	1.154
4.65	3.229	44.10	3.737	51.00	3.183	57.90	1.086
4.80	3.265	44.25	3.734	51.15	3.158	58.05	1.016
4.95	3.301	44.40	3.732	51.30	3.131	58.20	0.945
5.10	3.334	44.55	3.729	51.45	3.104	58.35	0.873
5.25	3.366	44.70	3.725	51.60	3.076	58.50	0.800
5.40	3.397	44.85	3.722	51.75	3.047	58.65	0.725
5.55	3.426	45.00	3.718	51.90	3.017	58.80	0.650
5.70	3.454	45.15	3.714	52.05	2.987	58.95	0.573
5.85	3.480	45.30	3.709	52.20	2.956	59.10	0.495
6.00	3.506	45.45	3.704	52.35	2.924	59.25	0.415
6.15	3.530	45.60	3.699	52.50	2.891	59.40	0.335
6.30	3.552	45.75	3.693	52.65	2.858	59.55	0.253
6.45	3.573	45.90	3.687	52.80	2.823	59.70	0.170
6.60	3.593	46.05	3.681	52.95	2.788	59.85	0.086
6.75	3.612	46.20	3.674	53.10	2.752	60.00	0.000

Note: The “X” dimensions start at the nose and increase moving aft.

## APPENDIX B: Tabular Comparison Between *Deep 6* and Other AUVs

Vehicle (units)	LOA in	D in	L/D n.d.	$\nabla$ in <sup>3</sup>	U <sub>MAX</sub> kts	Source
<i>Deep 6</i>	60.000	7.500	8.000	2,226.5	4.0	
REMUS	59.055	7.874	7.500	2,143.3	2.9	[39], [49]
Ocean Explorer	84.252	20.866	4.038	18,917.4	5.0	[4]
Morpheus (min)	60.000	9.000	6.667	1,523.2	4.0	[4]
Morpheus (max)	120.000	9.000	13.333	6,867.0	4.0	[4]
QUT** AUV	59.055	5.984	9.868	?	?	[40]
NPS AUV II (Phoenix)	87.624	N/A *	N/A *	11,745.0	1.2	[11], [19]
NPS AUV III (ARIES)	120.000	10.000 x 15.000*	N/A *	24,192.0	?	[7]
SAMS	163.200	24.000	6.800	?	4.0	[41]
SEAHORSE I	334.000	38.000	8.789	270,000.0	4.0	[41]
SPURV I	?	?	?	28,577.0	4.3	[49]
Odyssey	84.645	23.228	3.644	9,525.7	2.9	[17], [49]
ABE	78.740	?	?	40,484.1	2.0	[8], [49]
Theseus	420.000	50.000	8.400	512,003.9	3.9	[44], [40]
Autosub	?	?	?	101,210.3	3.0	[49]
Hugin 3000	204.000	39.600	5.152	83,349.3	4.0	[43], [49]
ARCS	252.000	27.000	9.333	81,000.0	?	[6]

\*Note: The Naval Postgraduate School AUVs have rectangular cross sections, and therefore do not have diameters.

\*\*Note: QUT, Queensland University of Technology.

## **APPENDIX C: Explanation of a Screw Propeller's Inherent Inefficiency**

The fundamental flaw with the modern marine screw propeller referred to in section 2.3 of this report arises from the propeller's principle of operation. The propeller functions by accelerating the fluid that is drawn through it. This acceleration causes a pressure differential to exist between the two sides of the propeller. Bernoulli's equation reveals that it is the faster moving fluid downstream of the propeller blade that has the lower pressure. The pressure differential between the fluid surrounding the lower pressure fluid downstream of the propeller (which is at static/ambient pressure) and the lower pressure fluid creates a force in the direction of travel. The net force exerted on the propeller is the difference between the resistive force exerted by the fluid on its back (upstream side) and the force on its face (downstream side). A propeller mounted behind a vehicle is aided by the presence of the vessel. The wake (the momentum deficit due to the friction of the hull preventing the fluid from returning to the free stream velocity at the stern of the body) from the vessel causes the fluid upstream of the propeller to have an elevated inflow velocity. This higher velocity increases the pressure gradient across the propeller, thus generating a greater propulsive force. The drawback of the aft mounted propeller is that it increases the fore-to-aft pressure gradient along the vessel. The lower pressure at the vehicle's stern increases the fluid's net resistive force exerted on the vehicle. Thus, while the presence of the hull aids the propeller's operation, the propeller hinders the hull by increasing the form/pressure drag. The situation becomes a catch-22; the faster the propeller turns, the higher the pressure gradient across the propeller, but the higher pressure gradient increases the drag for the hull, which requires more thrust to overcome

it. The increase in drag from the propeller is in addition to the already present  $R \propto v^2$  relationship for the hull [20], [32], [33].

## APPENDIX D: Propeller Optimization Program Input and Output

### Input Data:

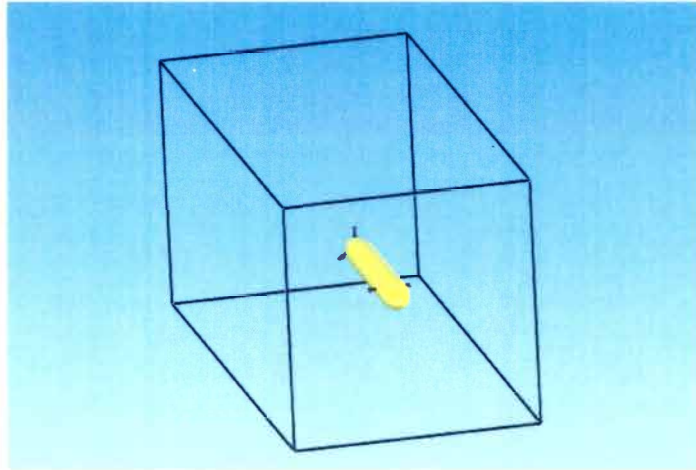
Design Mode = No Variable  
PropellerType = Fixed-Pitched Propeller  
WaterType = Fresh Water at 15C  
Cavitation Constraint = 5%  
Number of Blades = 4  
Required Thrust (kN) = 0.00571165  
Ship Speed = 4.0  
Wake Fraction = 0.4  
Depth of Shaft below WaterLine (m) = 0.142875  
Search Starting Value for Expanded Area Ratio = 0.5  
Search Starting Value for Pitch Diameter Ratio = 0.5  
Search Starting Value for Propeller Diameter = 0.07  
Minimum Diameter Constraint (m) = 0.0508  
Maximum Diameter Constraint (m) = 0.0762

### Optimal Design Results:

Propeller Diameter (m) = 0.07615378418439167  
Propeller Pitch (m) = 0.05927861970781676  
Pitch Diameter Ratio  $P/D_p$  = 0.7784067507963233  
Expanded Area Ratio = 0.4712560590526303  
Propeller Revolutions per Minute (rpm) = 1912.1829075191315  
Advance Coefficient (J) = 0.5090801573982102  
Thrust Coefficient (KT) = 0.15858049209921996  
Torque Coefficient (KQ) = 0.02183681154281022  
Propeller Open Water Efficiency (Eta 0) = 0.5883921046544349  
Propeller Thrust (kN) = 0.005407787743484282  
Reynolds Number (Rn) = 102164.095819258  
Cavitation Number (Sigma) = 6.597048502467369  
Optimization Search Evaluation Count = 32

## APPENDIX E: Sample CFD Analysis Output

**Figure a: Axial Flow FloWorks Analysis Control Volume**



Note: The analysis control volume was rectangular in cross section. The dimensions of the control volume were 140 in. long x 67.75 in. wide x 67.75 in. tall. The *Deep 6* model was centered both horizontally and vertically within the control volume. The nose of the *Deep 6* was positioned approximately 12 in. back from the inflow face of the control volume. The control volume's rectangular cross sectional shape was not desired but was a limitation imposed by Cosmos FloWorks.

**Figure b: FloWorks Surface Velocity Contour Plot**

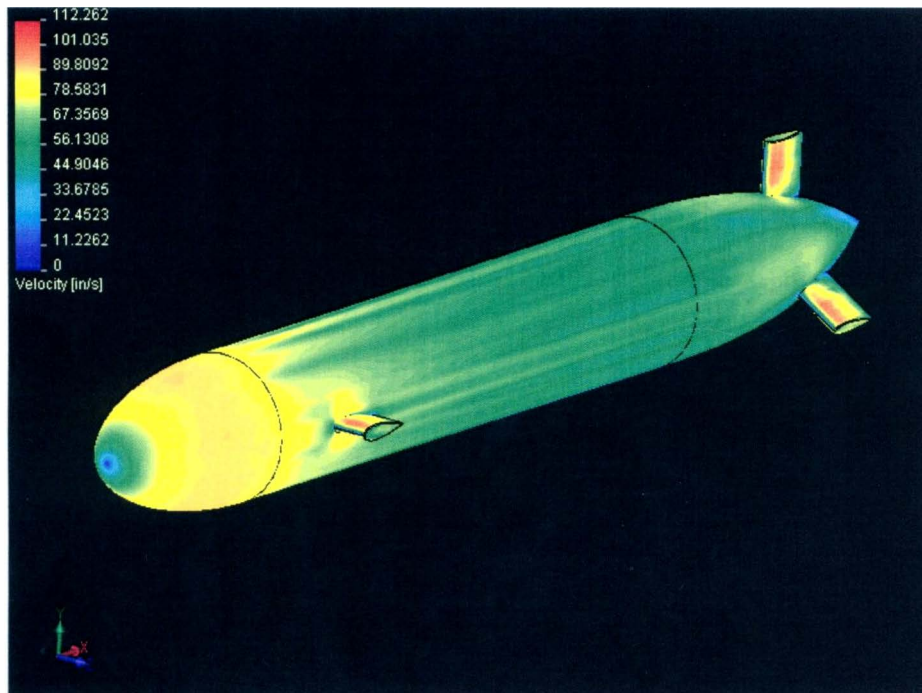




**Figure c: Axial Flow FLUENT Analysis Control Volume**

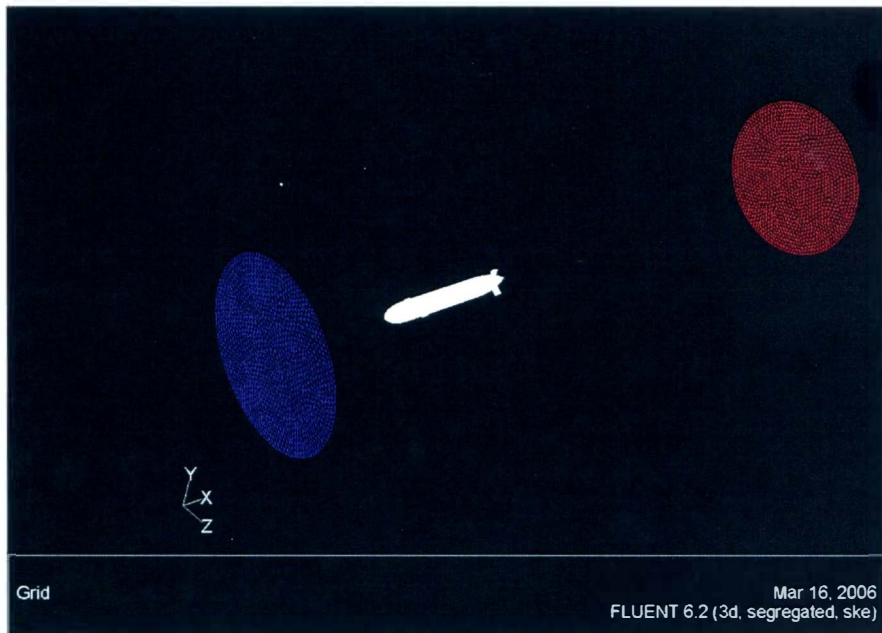


[Image generated by Anne Saad for the purpose of this study]

Note: The analysis control volume was circular in cross section. The control volume had a constant cross section along the entire length of 240 in. The diameter of the cross section was 75 in. The *Deep 6* model was placed along the centerline of the control volume cylinder. The nose of the *Deep 6* was positioned approximately 60 in. back from the inflow face of the control volume. The circular cross section for the control volume was desirable as a result of the shape of the *Deep 6*'s hull.

**Figure d: FLUENT Surface Velocity Vector Plot**

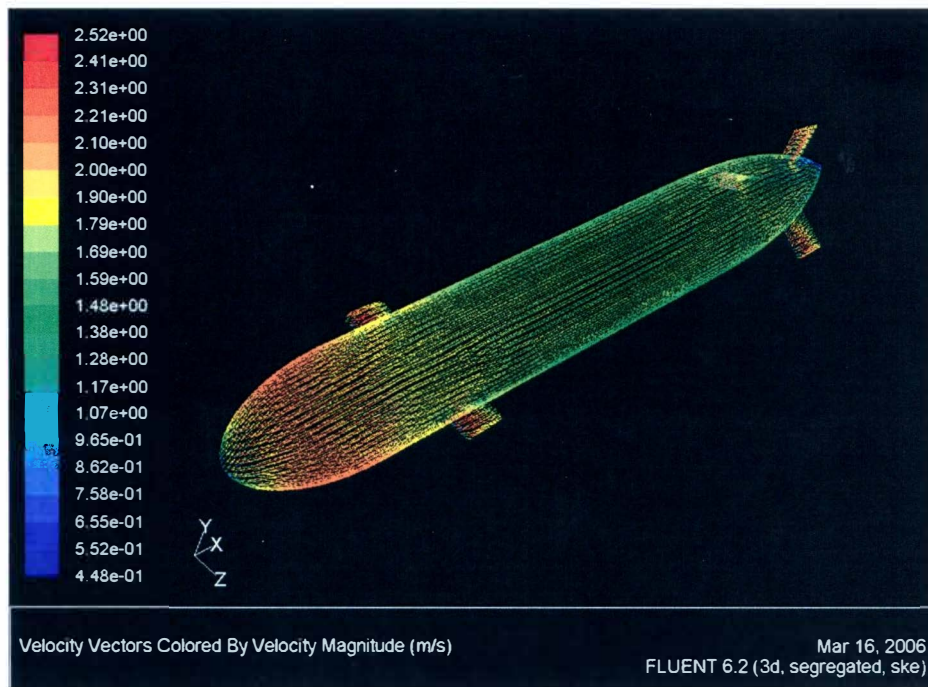


[Image generated by Anne Saad for the purpose of this study]

**Figure e: FloWorks Axial Velocity Central Vertical Plane Contour Plot**

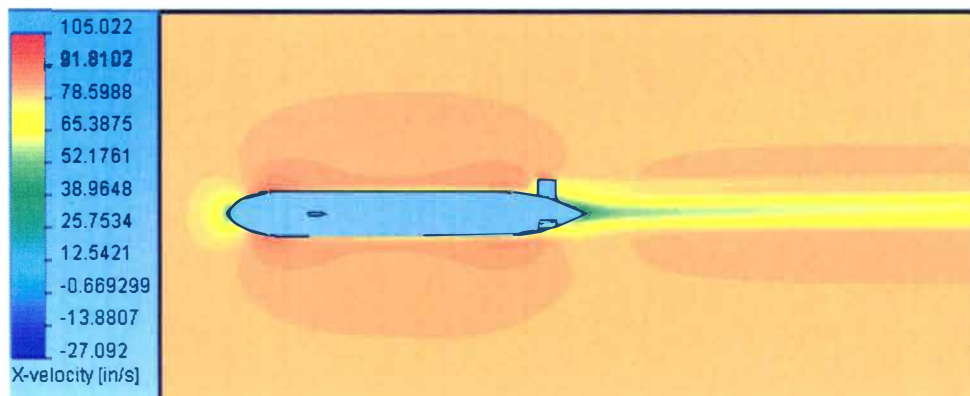


**Figure f: FloWorks Axial Velocity Central Horizontal Plane Streamline Plot**

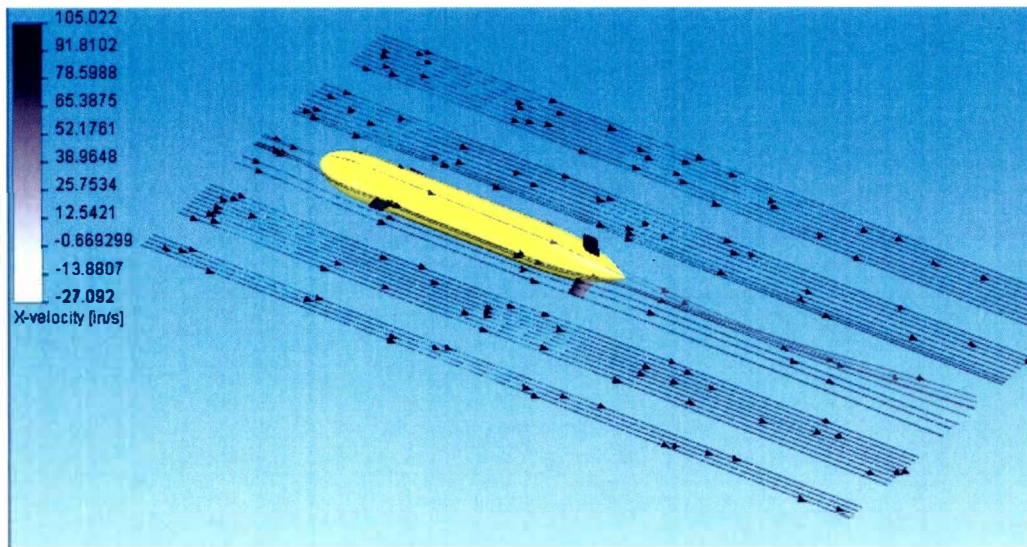
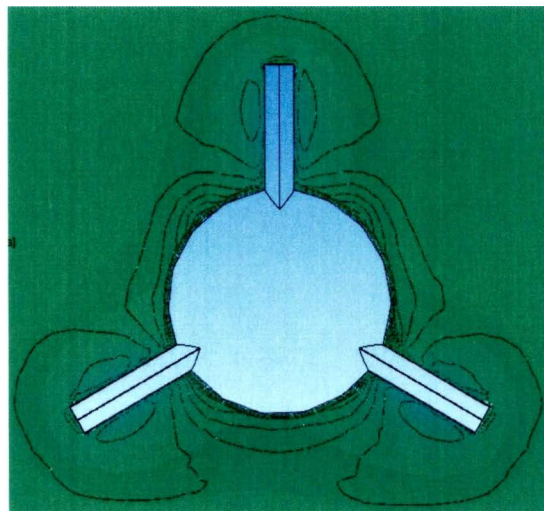


**Figure g: FloWorks Transverse Plane Across Aft Fins Pressure Contour Plot**



The analysis performed by FloWorks utilized the inch-pound-second system of units while the analysis performed by FLUENT utilized the SI system of units. The difference in units renders direct comparison between Figures b and d difficult. However, a visual inspection of these figures reveals that the flow patterns and relative velocity magnitudes predicted by each of the CFD programs is similar. This similarity and the similarity

between the predicted drags supports the conclusion that the actual hull drag is close in value to the results analytically determined. Again, it was not the intention of this investigation to develop a “perfect” hydrodynamic model of the *Deep 6*. The CFD analyses were only intended to confirm the first order analytical drag calculations.

Both CFD software packages that were used during this study are capable of incorporating fans/propellers into the flow analysis. This capability would have allowed the hull-propeller interaction effects to be included in the flow analysis results. This capability was not used since the flow analyses were used only to verify the analytically determined results. Typical naval architecture practice determines the hull and propeller characteristics independent of one another and the uses design factors to account for the interaction effects [33]. Since the analytical drag prediction for the *Deep 6* used naval architecture formulas and design guides, it did not include the propeller interaction effects. Adoption of this modeling scheme for the CFD analyses provided the clearest comparison possible with the analytical result. Also for both CFD analyses, the model of the *Deep 6* had the gap between the hull and the control fins removed to simplify the geometry. This procedure followed the recommended “best practices” guidelines for both of the programs.

## **APPENDIX F: Additional CFD Verification**

If design charts had not been available for the prediction of the wake fraction and thrust deduction, they would have typically been measured during physical testing. The CFD modeling that was performed for this project, however, can be substituted for physical testing during the preliminary design process [13]. Since the CFD modeling was performed without the presence of a propeller (the testing was done using a loose interpretation of “bare hull”), the results gathered did not allow for a prediction of the thrust deduction. However, the flow analysis did allow for a prediction of the wake fraction to be determined. Equation 1 displays the commonly accepted formula for calculating the wake fraction [3], [13], [33]. To determine the speed of advance for the first propeller, a contour plot on a plane normal to the hull’s longitudinal axis was created at the predicted location of the first propeller (30.5 in. from the vehicle CG). Figure a displays the contour plot that was generated. The value used to calculate the wake fraction was determined as a visual average taken from Figure a, and was estimated to be approximately 47 in/s. The wake fraction that was calculated using the CFD results was 0.42. This value is in close agreement with the value of 0.40 that was determined using the design charts. Therefore, either method of determining the wake fraction would produce a reasonable value for the purpose of preliminary design.



---

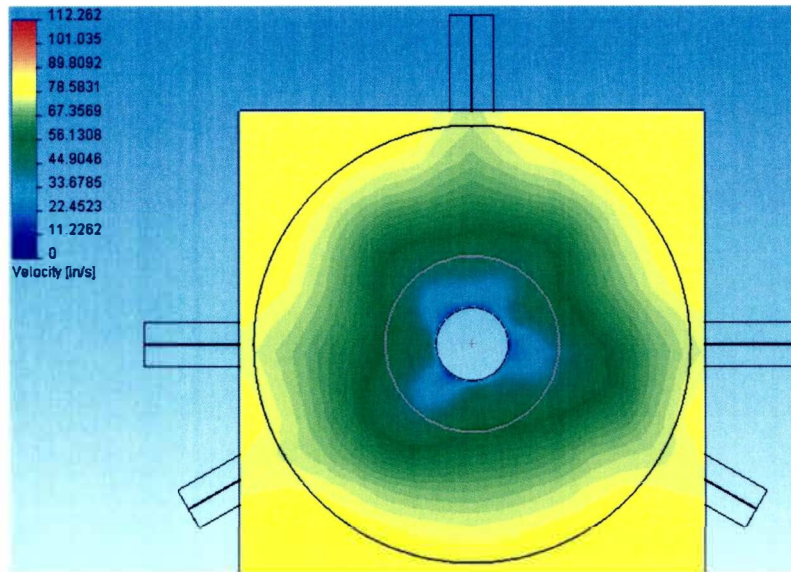
### Equation 1: Wake Fraction

$$w = \frac{v - v_A}{v}$$

Where  $w$  is the wake fraction,  $v$  is the vehicle speed, and  $v_A$  is the local speed of the fluid entering the propeller (speed of advance).

Note: This formula can be used for calculations of the local wake fraction or to estimate the average wake fraction for the entire propeller disk area.

**Figure a: Advance Speed Contour Plot**



The above figure is a contour plot of the fluid velocity around the hull in the region of the first of the *Deep 6*'s propellers. The largest of the three circles represents the maximum diameter of the hull. The smallest of the circles, with the blue center, represents the hull size where the cut plane was placed. The circle in the center of the two aforementioned circles represents the propeller diameter. The speed of advance was taken as an estimated area weighted average value for the colors between the two smaller circles (the fluid actually entering the propeller).

---

## APPENDIX G: Verification of Analytical Solutions Through Physical Testing

To receive independent validation for some of the vehicle parameters analytically determined, work is currently in progress to obtain some experimental data specific to the *Deep 6*. Two Western Michigan University undergraduate students have elected to perform wind tunnel and water channel testing of the *Deep 6* for their senior design project. To facilitate their testing, a 1:3.75 scale model of the *Deep 6*, with movable control fins, was CNC machined. Figure a shows a picture of the model that was created. Unfortunately, at the time of writing no substantial data was available for presentation.

---

**Figure a: 1:3.75 Scale Model of the *Deep 6* Created for Physical Testing**



The physical model of the *Deep 6* was machined out of the DuPont acetyl plastic Delrin. The model has 0.093 in. diameter stainless steel dowel pins supporting the five control fins. There is a 0.75 in. diameter hole in the stern for mounting the model onto the wind tunnel's sting balance. Underneath each of the three aft control fins is a stainless steel #6-32 set screw for locking the model into position once it is mounted.

---